Stuart- Landau Oscillators with Pairwise and Higher order interactions and Application in PGES

Submitted in partial fulfillment of the requirements
of the degree of

Doctor of Philosophy

by

Subhasanket Dutta
(Roll No. 1901151010)

Supervisor:
Prof. Sarika Jalan

Department of Physics
INDIAN INSTITUTE OF TECHNOLOGY INDORE
2025

Dedicated to Baba

INDIAN INSTITUTE OF TECHNOLOGY
INDORE

I hereby certify that the work which is being presented in the thesis entitled **Stuart- Landau Oscillators with Pairwise and Higher order interactions and Application in PGES** in the partial fulfillment of the requirements for the award of the degree of **DOCTOR OF PHILOSOPHY** and submitted in the **Department of Physics**, **Indian Institute of Technology Indore**, is an authentic record of my own work carried out during the time period from **July 2019** to **Nov 2024** under the supervision of **Prof. Sarika Jalan**, **IIT Indore**.

The matter presented in this thesis has not been submitted by me for the award of any other degree of this or any other institute.

12 Aug 2025

signature of the student with date

(**Subhasanket Dutta**)

This is to certify that the above statement made by the candidate is correct to the best of my/our knowledge.

12 Aug 2025

Signature of Thesis Supervisor #1 with date

(Prof. Sarika Jalan)

Signature of Thesis Supervisor #2 with date

(NAME OF THE SUPERVISOR)

Subhasanket Dutta has successfully given his Ph.D. Oral Examination held on **12 Aug 2025**.

12 Aug 2025

Signature of Thesis Supervisor #1 with date

(Prof. Sarika Jalan)

Signature of Thesis Supervisor #2 with date

(NAME OF THE SUPERVISOR)

Acknowledgement

With gratitude to the support of numerous individuals, I have successfully completed this dissertation, and I express my sincere thanks from the depths of my heart. I extend my heartfelt appreciation to my supervisor, Prof. Sarika Jalan, for her guidance and unwavering support throughout this journey. Her encouragement through challenging tasks during my tenure at the Indian Institute of Technology (IIT) Indore has been instrumental in boosting my confidence as both a student and a professional. The experience of learning, interacting, and collaborating at the Complex Systems Lab during my Ph.D. has contributed significantly to my growth, not only as a researcher but also as an individual. I extend my sincere appreciation to the members of the PSPC committee, Dr. Dipankar Das, and Dr. Md. Tanveer for offering invaluable insights and providing constructive suggestions to enhance my research work. I am also thankful to the Director of IIT Indore, DPGC convener, Head of the Department of Physics, Dean of Academic Affairs (DOAA), and all faculty and staff members of the Department of Physics at IIT Indore, including Mr. Rahul, Mr. Vedprakash Thakur, Mr. Nitin Upadhyay, and Mr. Prashant Gupta, for their timely assistance and support. Special thanks are due to the staff members of the Academic Office, Accounts Section, R&D Section, IT Section, Central Library, and Medical Team at IIT Indore for their continuous support, ensuring the smooth progress of my research work. I express my gratitude to Mr. Tapesh Parihar and Mr. Rahul Srivas for their dedicated efforts in completing the intricate and time-consuming official formalities related to the Ph.D. thesis. The journey of obtaining a Ph.D. was a long and challenging path, marked by numerous sleepless nights. I owe a debt of gratitude to the global community that offered invaluable support. Numerous personal and email exchanges significantly enriched and refined this dissertation. Foremost, I extend my appreciation to Dr. Sandipan Pati (CNR-Institute of Complex Systems, Italy), and Woo-Soek Lee (IBS South Korea) for engaging in fruitful discussions and offering valuable suggestions. I also express my gratitude to all the journal reviewers who meticulously assessed the manuscript and provided constructive feedback, contributing to the accuracy and improvement of the thesis content. I feel incredibly grateful, and with heartfelt appreciation, I extend my thanks to all the research scholars at the Complex Systems Lab. Special gratitude

goes to Dr. Ajaydeep Kachhvah, Dr. Pramod Shinde, Dr. Saptarshi Ghosh, Dr. Anil Kumar, Dr. Rahul, Dr. Ankit Mishra, Dr. Vasundhara Rathore, Tanu Raghav, Dr. Umesh kumar Verma, Jerry David, Ayushi Suman, Priyanka Rajwani, Abhishek Sharma, Dishant Sisodia, Jayesh Jain for their unwavering love, care, and support.

Supported by the generosity of many individuals, I have successfully overcome numerous challenges and reached the culmination of my Ph.D. thesis. I am eternally grateful to these individuals for turning my dream into reality. I am fortunate to have had wonderful friends, such as Vasundhara and Tanu, who were by my side throughout much of this journey, making it both memorable and joyful. I also thank Priyanka, Abhishek, Dishant and Jayesh for their invaluable support in the final stages of my Ph.D. I would like to acknowledge a few friends I made at IIT outside my lab. Dhruv, with whom I had many deep conversations, and Ayan, who provided tremendous support and made me feel at home. I also extend my gratitude to Souparno and Arpan for the time we spent together. Your presence holds a unique significance to me, and I will forever cherish it. Apart from my colleugues and friends at IIT I would like to mention my childhood friends Arka and Baidya who have been very supportive. Special thanks go to these friends for their consistent help, which added warmth and joy to my scholarly pursuit, making this accomplishment even more beautiful. While it is impossible to mention everyone by name, I am sincerely thankful for the widespread and generous support I have received throughout my academic journey.

I am deeply indebted to the most significant individuals in my life – my family. My heartfelt gratitude goes to my loving and warmhearted parents, my sister, my adorable niece, and my in-laws whose simple yet profound words continue to inspire me. I owe my heartfelt thanks to my wife, Aditi, whose love, understanding, and belief in me sustained me during the most challenging phases of this work. I am deeply thankful for the care and her unwavering support and marrying me. Special thanks to my Maa, for being the epitome of light and persistence throughout my life.

This journey would not have been possible without all the constant encouragement and love.

Thank you!!

Abstract

This thesis focuses on pairwise and higher-order modeling of coupled Stuart-Landau oscillators, with an emphasis on the suppression of oscillations and its application to a neuropathological condition known as Postictal Generalized EEG Suppression (PGES). To investigate the suppression of oscillations in various nonlinear model systems, coupled Stuart-Landau oscillators prove to be particularly suitable for understanding the origin and implications of such behavior. Quenching of oscillations in these systems is primarily achieved through three mechanisms, introducing parameter mismatch, communication delays, and conjugate coupling. A quenched or "death" state of an oscillator can be broadly classified into two categories, amplitude death (AD) and oscillation death (OD), based on the spatial configuration and symmetry of the associated fixed points. The AD state corresponds to all oscillators converging to the same fixed point, which is typically an unstable fixed point in the uncoupled system. In this case, coupling stabilizes the AD state via a Hopf bifurcation while preserving parity symmetry. In contrast, in the OD state, oscillators settle at different fixed points that emerge due to coupling-induced and parity symmetry-breaking bifurcations. First, we propose a coupling setup that yields suppression in coupled Stuart-Landau oscillators in the form of AD and OD. We derive the necessary and sufficient condition for attaining the AD state for this setup. Moreover, we develop a generalized theoretical framework to obtain the analytical condition for AD state for similar coupling forms. Furthermore, we attempt to identify applications of dynamical models that demonstrate the suppression of oscillations in a neuropathological condition known as PGES. PGES is defined by marked suppression in brain activity just after a tonic-clonic seizure. Assuming that the functional connectivity matrix is a good approximation of the adjacency matrix, we numerically analyzed the coupled dynamics model for the functional connectivity matrix from the seizure data. We found that the phenomenon of amplitude suppression in the model resembles the PGES. It has increasingly been realized that real-world complex systems made of dynamical units may not only have pairwise interactions but also possess higher-order structures; examples

include cliques in the human brain Sizemore et al. (2018), scientific collaborations Vasilyeva et al. (2021). Therefore, we turn our attention to interactions beyond pairwise. We devise a scheme to incorporate higher-order interactions that cannot be decomposed into pairwise interactions, and investigate the dynamical evolution of Stuart-Landau oscillators under the influence of such a coupling. We discover an oscillator death state through first-order (explosive) phase transition in which a single, coupling dependent stable death state away from the origin exists in isolation without being accompanied by any other stable state, usually existing for pair-wise couplings. We call such a state a solitary death state. We report the emergence of a coupling-dependent SD state, a single stable quenched state arising from the higher-order interactions. Contrary to wide-spread subcritical Hopf bifurcation, here we report homoclinic bifurcation as an origin of the explosive death state. Moreover, this explosive transition to the death state is preceded by a surge in amplitude, and followed by a revival of the oscillations. The analytical value of the critical coupling strength for the solitary death state agrees with the simulation results.

Finally, we focus on the mechanism behind PGES and the revival of normal brain function after PGES. Postictal dynamics vary across brain regions and individuals but typically begin with a suppressed phase marked by significant signal attenuation. This is followed by a transitional phase where bursts of high-amplitude activity intermittently interrupt the suppressed state, eventually leading to recovery characterized by a return to preictal-like activity. we analyzed the power distribution across EEG channels and found that the suppressed state exhibits a unimodal exponential distribution, while the transitional phase displays pronounced bimodality. To capture this behavior, we employed the subcritical Hopf normal form, identifying parameter regimes that reproduce these empirical features. While the complexity of parameter interactions prevents us from definitively attributing the observed transitions to a classical subcritical Hopf bifurcation, our results support a transition from a fixed-point regime to a bistable state as a plausible underlying mechanism of EEG recovery during PGES.

To summarize, the results presented in the thesis provide valuable insights into the dissimilar repulsive coupling form in Stuart-Landau oscillators. We demonstrate that this mechanism can account for AD, OD, and oscillation state, as well as the transitions between them. Additionally, we show that these findings have applications in neurological systems, specifically in the context of postictal generalized EEG suppression (PGES). Furthermore, we extend our work to triadic interactions in SL oscillators and conclude that they can give rise to bistability and a coupling-

dependent solitary fixed point. Finally, we successfully generate states similar to PGES using the subcritical Hopf normal model and report the phase transitions occurring during PGES and its revival to normal brain function.

Objectives:

1. To understand the role of pairwise dissimilar coupling in identical and non identical SL oscillators.
2. Find an application of such coupling in PGES using functional connectivity as the adjacency matrix.
3. To explore the role of higher-order interaction in coupled SL oscillator.
4. Determine the phase transitions taking place in PGES.
5. To find a suitable dynamical model explaining the phase transitions in PGES.

Conclusion and Future Scope: The results presented in this document provide valuable insights into the dissimilar repulsive coupling form in Stuart-Landau (SL) oscillators. We demonstrate that this mechanism can account for amplitude death (AD), oscillation death (OD), and oscillation suppression (OS), as well as the transitions between them. Additionally, we show that these findings have applications in neurological systems, specifically in the context of postictal generalized EEG suppression (PGES). Furthermore, we extend our work to triadic interactions in SL oscillators and conclude that they can give rise to bistability and a coupling-dependent solitary fixed point. Finally, we successfully generate states similar to PGES using the subcritical Hopf normal model and report the phase transitions occurring during PGES and its revival to normal brain function.

Future work will explore other approaches to modeling real neurobiological data using dynamical differential equations. Exploring the use of functional connectivity dynamics in EEG data may enable more accurate modeling. Additionally, higher-order interactions have been rarely studied in real data and hold great potential. Developing a framework to identify higher-order interactions in EEG data could address fundamental questions in neuroscience and help bridge the gap between neuroscience and nonlinear dynamics.

Contents

List of Tables

List of Figures

List of Abbreviations

SL	Stuart Landau
HB	Hopf Bifurcation
AD	Amplitude Death
OD	Oscillation Death
EEG	Electroencephalogram
PGES	Postictal Generalised EEG Suppression
SUDEP	Sudden death in epileps
SD	Solitary Death
EO	Enhancement of oscillation
RO	Revival of oscillation

List of Publications

Thesis

1. **Dutta, S.**, Alamoudi, O., Vakilna, Y. S., Pati, S., & Jalan, S. (2023). Oscillation quenching in Stuart-Landau oscillators via dissimilar repulsive coupling. *Physical Review Research*, 5(1), 013074. DOI: 10.1103/PhysRevResearch.5.013074

2. **Dutta, S.**, Verma, U. K., Jalan, S. (2023). Solitary death in coupled limit cycle oscillators with higher-order interactions. Physical Review E, 108(6), L062201. DOI: 10.1103/PhysRevE.108.L062201

3. **Dutta, S.**, Vakilna, Y. S., Pati, S., Jalan, S. (2024) Dynamical phase transition in Postictal generalized EEG suppression. (To be submitted.)

Other publications

1. Panday, A., Lee, W. S., **Dutta, S.**, Jalan, S. (2021). Machine learning assisted network classification from symbolic time-series. Chaos: An Interdisciplinary Journal of Nonlinear Science, 31(3). DOI: https://doi.org/10.1063/5.0046406

2. Moyal, B., Rajwani, P., **Dutta, S.**, Jalan, S. (2024). Rotating clusters in phase-lagged Kuramoto oscillators with higher-order interactions. *Physical Review E*, 109(3), 034211. DOI: 10.1103/PhysRevE.109.034211

3. Tipping in Stuart-Landau oscillators induced by higher-order repulsive interactions Umesh Kumar Verma, **Subhasanket Dutta**, Richita Ghosh, Manish Dev Shrimali, and Sarika Jalan *Phys. Rev. E 110*, 044211 – Published 22 October 2024 DOI:https://doi.org/10.1103/Phys

Chapter 1

Introduction

1.1 Dynamical systems

Studying a dynamical system involves analyzing its temporal evolution. A system may exhibit various behaviors, such as settling to a fixed point, displaying repetitive or periodic dynamics, showing sensitivity to perturbations, and producing other complex spatial and temporal patterns. Such systems arise in diverse fields, including classical mechanics Goldstein et al. (2002), chemical kinetics Steinfeld et al. (1999), and population biology Zhao (2017). In classical mechanics, many systems evolve in time, such as a swinging pendulum or planetary motion. In chemical kinetics, the Belousov-Zhabotinsky reaction serves as an excellent example of a dynamical system, where the concentrations of chemicals oscillate over time. Similarly, in population biology, the interaction between species and environmental factors can be modeled to study population dynamics using concepts from dynamical systems. Typically, these systems are mathematically represented using differential equations (continuous-time models) or maps (discrete-time models). For instance, the differential equations of the Brusselator model effectively describe the oscillatory behavior observed in the Belousov-Zhabotinsky reaction Steinfeld

et al. (1999). On the other hand, the logistic map provides insights into the population dynamics of ecological systems Strogatz (2015).

History: The concept of dynamical systems can be traced back to the invention of differential equation by Newton. Together with laws of motion and gravity he found the exact solution of the two body problem and which conformed with Kepler's law of planetary motion and is considered a landmark in this field Goldstein et al. (2002). Although the two body problem was solved, the solution of three body problem alluded scientist for a long time due to its non linear and complex nature. Poincare introduced a different point of view and asked the question about the stability of system rather than the exact solution and provided a geometric interpretation which would help to answer that question Strogatz (2015); Tabor (1989); Devaney (1989). In the subsequent time non linear oscillators found many applications in radio, laser and radar sStrogatz (2015).

The invention of high-speed computers in the 1950s had a major impact in the realm of non-linear dynamics. Lorentz found the computational solution of a set of non linear differential equations describing the weather system had an aperiodic and irregular behavior. Any change in the initial condition led to vastly different weather predictions. This led to the discovery of chaos which was defined as the deterministic but extreme sensitive to the initial condition. Further, it was proposed that non-linearity was the cause of this complex behavior Gleick (1987).

Importance of Non-Linearity: A dynamical system is considered linear when it can be decomposed into smaller parts, solved separately, and recombined to obtain the final solution Strogatz (2015); Robinson (1995). Mathematically, the time evolution of linear systems can be expressed as $\frac{d\mathbf{x}}{dt} = A\mathbf{x}$, where $\mathbf{x}$ is a variable representing the dynamical state of the system and A is a constant matrix. Furthermore, if $\mathbf{x}_1$ and $\mathbf{x}_2$ are solutions to this differential equation, then any linear combination $c_1\mathbf{x}_1 + c_2\mathbf{x}_2$ is also a solution. For linear systems, solutions to these differential equations can often be found in closed form. However, for most nonlinear systems, obtaining analytical solutions is significantly more challenging. In such cases, geometric interpretations are particularly insightful. Additionally, computational approaches, such as the Euler method and more advanced techniques like the fourth-order Runge-Kutta method, are widely employed to approximate solutions Strogatz (2015). Linear systems exhibit predictable and stable behaviors, such as exponential growth/decay or oscillations. However, they lack the

complex and chaotic behaviors that are characteristic of nonlinear systems Devaney (1989).

1.1.1 Geometric approach and Linear stability analysis

Although most nonlinear differential equations do not have closed-form solutions, some do. For example, the solution of the first-order system $\dot{x} = \sin(x)$ is given by the time t,

$$t = \ln \left| \frac{\csc(x_0) + \cot(x_0)}{\csc(x) + \cot(x)} \right|,$$

which is difficult to interpret and does not directly address stability in the phase plane. In the geometric representation, the direction of the particle's flow is visualized as a vector field. The positions in phase space where the flow stops are called fixed points Strogatz (2015); Devaney (1989).

Consider the general form of a one-dimensional first-order dynamical system, $\dot{y} = f(y)$, where the $\dot{y}$ vs y diagram represents the phase plane. The flow stops when $\dot{y} = 0$, which occurs when $f(y^*) = 0$, meaning y^* is a fixed point. To analyze the stability of the system, a small perturbation is introduced, and its growth or decay over time is observed Tabor (1989). Let the perturbation be $\eta(t) = y(t) - y^*$. Expanding $f(y)$ as a Taylor series around $y = y^*$, we have

$$f(y) = f(y^*) + (y - y^*)f'(y^*) + \dots$$

Ignoring higher-order terms and using $f(y^*) = 0$, this simplifies to $f(y) = \eta f'(y^*)$. Substituting this into the original differential equation gives

$$\dot{\eta} = \eta f'(y^*),$$

with the solution

$$\eta(t) = \eta_0 \exp(f'(y^*)t).$$

This shows that if $f'(y^*) < 0$, the perturbation $\eta(t)$ decays exponentially, leading to a stable solution (stable fixed point). Conversely, if $f'(y^*) > 0$, the perturbation grows exponentially, resulting in an unstable solution (unstable fixed point).

1.1.2 Two-Dimensional Systems and Limit Cycles

Linear Systems: Compared to one-dimensional systems, higher-dimensional systems exhibit more diverse dynamical behaviors. We begin with a simple two-dimensional linear system represented as

$$\begin{bmatrix} \dot{x} \\ \dot{y} \end{bmatrix} = \begin{bmatrix} a & b \\ c & d \end{bmatrix} \begin{bmatrix} x \\ y \end{bmatrix}. \tag{1.1}$$

In shorthand, this can be written as $\dot{\mathbf{x}} = A\mathbf{x}$, where

$$\mathbf{x} = \begin{bmatrix} x \\ y \end{bmatrix}, \; A = \begin{bmatrix} a & b \\ c & d \end{bmatrix}.$$

The fixed point solution $\mathbf{x}^*$ is obtained when $\dot{\mathbf{x}} = 0$ 1.1(a,c). For a nonsingular matrix A, the eigenvalue problem $A\mathbf{v} = \lambda\mathbf{v}$ yields eigenvalues $\lambda_{1,2}$ and their corresponding eigenvectors $\mathbf{v}_{1,2}$. When the eigenvalues are distinct and the algebraic multiplicity equals the geometric multiplicity, the eigenvectors are independent. In this case, the general solution can be expressed as a linear combination of the eigensolutions:

$$\mathbf{x}(t) = c_1 e^{\lambda_1 t}\mathbf{v}_1 + c_2 e^{\lambda_2 t}\mathbf{v}_2, \tag{1.2}$$

where c_1 and c_2 are constants. The determinant of A is $\Delta = ad - bc$, and its trace is $\delta = a + d$. The eigenvalues of A are given by

$$\lambda_k = \frac{\delta \pm \sqrt{\delta^2 - 4\Delta}}{2}, \; k \in 1,2$$

The fixed point $\mathbf{x}^*$ is stable if $\mathrm{Re}[\lambda_k] < 0,\ k \in 1,2$, as the solution in Eq. (1.2) decays exponentially. Conversely, the fixed point is unstable if $\mathrm{Re}[\lambda_{1,2}] > 0$ 1.1(b).

If one eigenvalue indicates stability and the other instability, the fixed point is a "saddle point" 1.1(d). For $\mathrm{Im}[\lambda] \neq 0$, trajectories in the vicinity of the fixed point spiral inward or outward. If $\mathrm{Re}[\lambda_k] = 0$, the fixed point is a "center", where $\delta = 0$ and $\lambda_k = \pm i\sqrt{\Delta},\ k \in 1,2$ 1.1(e). In this case, the general solution describes a circular trajectory, with the radius being the distance from the initial point to the centerKuznetsov (2013). Various types of flows along with the nature of eigenvalues are shown in Fig. 1.1.

Nonlinear Systems: When nonlinearity is introduced, the analysis becomes more complex. Unlike linear systems, nonlinear systems can exhibit a range of behaviors such as fixed points, closed orbits, and limit cycles. While the stability of fixed points can still be analyzed by linearizing the system, limit cycles require different techniquesRobinson (1995); Devaney (1989).

Consider a generalized two-dimensional nonlinear system:

$$\dot{x} = f(x,y), \quad \dot{y} = g(x,y). \tag{1.3}$$

Fixed points (x_0, y_0) are defined by the conditions $f(x_0,y_0) = 0$ and $g(x_0,y_0) = 0$. Let $u = x - x_0$ and $v = y - y_0$, and substitute these into Eq. (1.3):

$$\dot{u} = f(u,v), \quad \dot{v} = g(u,v). \tag{1.4}$$

Next, expand $f(u,v)$ and $g(u,v)$ as Taylor series around $u = 0$ and $v = 0$:

$$f(u,v) = f(0,0) + u\frac{\partial f}{\partial u}\Big|_{(0,0)} + v\frac{\partial f}{\partial v}\Big|_{(0,0)} + \mathscr{O}(u^2, v^2),$$

$$g(u,v) = g(0,0) + v\frac{\partial g}{\partial v}\Big|_{(0,0)} + u\frac{\partial g}{\partial u}\Big|_{(0,0)} + \mathscr{O}(u^2, v^2).$$

Since $f(0,0) = 0$ and $g(0,0) = 0$, and ignoring higher-order terms, the system can be linearized

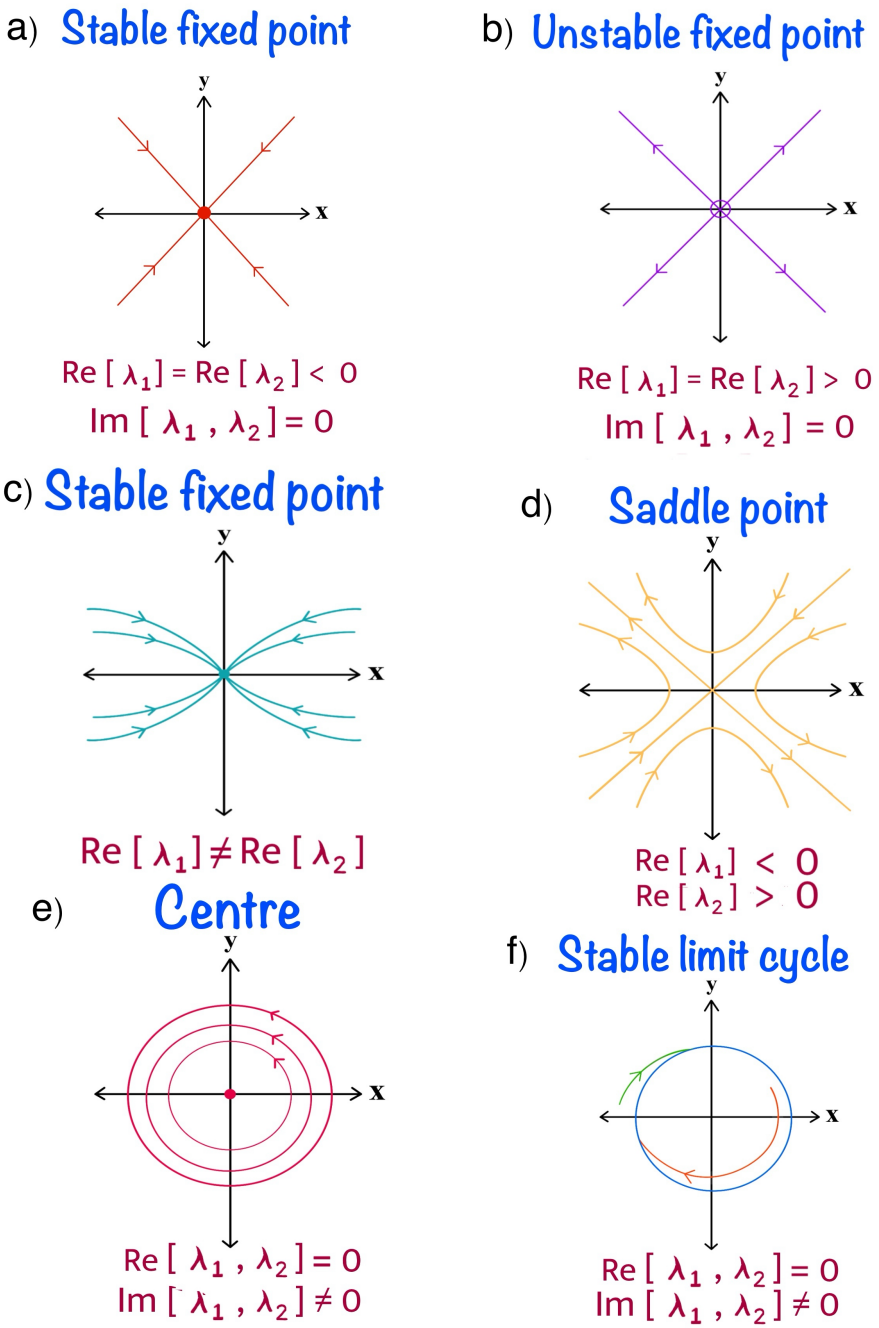

Figure 1.1: Figure describing various types of flows along with the nature of eigenvalues. (a) stable fixed point where all trajectories come towards the red solid circle in a straight line, (b) unstable fixed point where all trajectories come towards the blue open circle in a straight line, (c) Example of a stable fixed point where all trajectories come towards the magenta solid circle with different velocities along the two axes, (d) Saddle point stable along one eigen direction and unstable along the other, (e) Centre with non islolated closed trajectories shown in red. (d) Stable limit cycle (blue closed circle) for a non linear system attracting nearby trajectories.

as:

$$\begin{bmatrix} \dot{u} \\ \dot{v} \end{bmatrix} = \begin{bmatrix} \frac{\partial f}{\partial u}\Big|_{(0,0)} & \frac{\partial f}{\partial v}\Big|_{(0,0)} \\ \frac{\partial g}{\partial u}\Big|_{(0,0)} & \frac{\partial g}{\partial v}\Big|_{(0,0)} \end{bmatrix} \begin{bmatrix} u \\ v \end{bmatrix}. \tag{1.5}$$

The Jacobian matrix J at the fixed point $(0,0)$ is defined as:

$$J = \begin{bmatrix} \frac{\partial f}{\partial u}\Big|_{(0,0)} & \frac{\partial f}{\partial v}\Big|_{(0,0)} \\ \frac{\partial g}{\partial u}\Big|_{(0,0)} & \frac{\partial g}{\partial v}\Big|_{(0,0)} \end{bmatrix}.$$

This linearization preserves the stability properties of the fixed point. The eigenvalues of J determine the stability of the fixed points, following the same procedure as for linear systems.

Limit cycle: A limit cycle is an isolated closed periodic orbit in the state space. Neighboring trajectories are either attracted to a stable limit cycle or repelled from an unstable limit cycle. The primary factor responsible for the existence of a limit cycle is nonlinearity in the system 1.1(f). While linear systems can have closed periodic orbits, these are not isolated. For a generalized linear system of the form $\frac{d\mathbf{x}}{dt} = A\mathbf{x}$, if $\mathbf{x}(t)$ is a solution, any expression of the form $c\mathbf{x}(t)$ (where c is a scalar) will also be a solution. This results in a family or band of stable orbits, not an isolated one. A good example is the simple harmonic oscillator system, where the initial conditions determine the amplitude of the orbit. Another example is the simple pendulum, which is linear for small oscillations and exhibits a non-isolated closed curve trajectory. Furthermore, it can show similar behavior even with large amplitudes, making it an example of a nonlinear center. Hence, while all limit cycles are closed orbits, not all closed orbits are limit cycles Robinson (1995); Kuznetsov (2013). In nature, many systems exhibit self-sustained oscillations, where even when perturbed, the system returns to its earlier oscillatory state. These systems can be represented by limit cycles.

To emphasize the role of nonlinearity in the existence of a limit cycle, we examine the Stuart-Landau equation, which describes a nonlinear system with a limit cycle:

$$\dot{z}(t) = (1 - |z(t)|^2)z + i\omega z, \tag{1.6}$$

where z is a complex variable representing the dynamical state of the oscillator, and ω is its intrinsic frequency. This equation is known to have a stable limit cycle with radius 1. By assuming a solution of the form $z = r\exp(i\omega t)$ and substituting it into Eq. (1.6), we find that $r = 1$, meaning the only possible closed orbit has radius 1 and frequency ω.

Next, examining the vector field, we observe:

$$\dot{r} < 0 \quad \text{if} \quad r > 1, \quad \dot{r} > 0 \quad \text{if} \quad r < 1.$$

This implies that trajectories with $r > 1$ are attracted toward $r = 1$, and those with $r < 1$ are repelled, confirming that $r = 1$ is a stable limit cycle.

There are various methods to rule out closed orbits in systems. For example, gradient systems (where, $\frac{d\mathbf{x}}{dt} = -\nabla V(x)$, V(x) being a scaler function) cannot exhibit closed orbits, and the presence of a Lyapunov function (a real scaler function V(x)) also rules out closed orbits. However, the Poincaré-Bendixson Theorem provides conditions for the existence of closed orbits in two-dimensional systems. If P is a closed, bounded subset of the real plane ($\mathbb{R}^2$), and $\frac{d\mathbf{x}}{dt} = \mathbf{F(x)}$ is a dynamical system where $\mathbf{F(x)}$ is differentiable on P (including its boundary) and has no fixed points inside A, then any trajectory starting in A and staying within it for all time must either be a closed orbit or tend to a closed orbit as $t \to \infty$ Robinson (1995).

In practice, we seek an annular region around a potential limit cycle that contains no fixed points, and where $\mathbf{F(x)}$ is differentiable. The vector field at the boundaries of this annulus should point inward. This ensures that the annular region is a trapping region, meaning that any trajectory starting within it remains there. For example, consider the Stuart-Landau oscillators in Eq. (1.6). We can define an annular region around $r = 1$ with thickness δ. At $r = 1 + \delta$, we have $\dot{r} = -\delta^2 < 0$, and at $r = 1 - \delta$, $\dot{r} = \delta^2 > 0$. Thus, we form a closed trapping region where trajectories stay within the annulus. Since this region must contain a fixed point, we confirm the presence of a closed orbit.

Finally, one-dimensional systems cannot exhibit limit cycles because closed orbits are not possible in such systems.

1.1.3 Bifurcations

A system can reside in various types of dynamical states depending on parameter values and initial conditions. The transition from one dynamical state to another qualitatively different dynamical state by tuning a parameter value is called a "bifurcation", and the parameter values at which these transitions occur are called "bifurcation points". All systems exhibiting a specific type of bifurcation behave similarly around the critical point, and their behavior in this parameter region can be described by a set of differential equations known as the "normal form". Some types of bifurcations relevant to our study are discussed below Fig. 1.2.

Saddle-Node Bifurcation: This bifurcation describes the creation or destruction of a pair of fixed points. In a one-dimensional system, this corresponds to the emergence of a stable and an unstable fixed point, while in higher-dimensional systems, it corresponds to the creation or destruction of a stable point and a saddle point. The normal form is given by:

$$\dot{x} = r - x^2, \tag{1.7}$$

where r is the bifurcation parameter Fig. 1.2(a).

An example of saddle-node bifurcation can be observed in electrical power grids, where this bifurcation occurs during voltage collapse—a critical phenomenon in which the system loses its ability to sustain stable operating points due to excessive load or insufficient power generation Caízares (2001).

Pitchfork Bifurcation: A pitchfork bifurcation occurs when a stable equilibrium point splits into multiple equilibria as a system parameter is varied. This type of bifurcation often arises in systems with symmetry. Pitchfork bifurcations can be classified as either subcritical or supercritical: - In a "supercritical pitchfork bifurcation", a single stable equilibrium branches into two new stable equilibria, while the original equilibrium becomes unstable Fig. 1.2(b). The normal form is given by:

$$\dot{x} = (r - x^2)x. \tag{1.8}$$

For instance, consider a mechanical system where a vertical beam bends under the application of a force or weight. Before applying the weight, the beam has a single stable state (the upright position). After applying the weight, the system exhibits two symmetric stable bent states. - In a "subcritical pitchfork bifurcation", two unstable equilibria merge into a stable equilibrium, which was previously unstable Fig. 1.2(c). The normal form remains the same but is often modified by an additional x^5 term to capture bistability:

$$\dot{x} = (r + x^2)x + x^5. \tag{1.9}$$

This bifurcation is commonly associated with bistability and hysteresis Verma et al. (2019); Suman and Jalan (2024); Rajwani et al. (2023); Sharma et al. (2024).

Pitchfork bifurcations are also referred to as "symmetry-breaking bifurcations" because, prior to bifurcation, the system has only one stable state, whereas after bifurcation, the system chooses between multiple stable states, thereby breaking symmetry Koseska et al. (2013b,a).

Hopf Bifurcation: Hopf bifurcation describes the onset or cessation of oscillations. - A "supercritical Hopf bifurcation" involves a smooth transition from oscillation to a fixed-point state. - In contrast, a "subcritical Hopf bifurcation" involves an abrupt transition, often associated with bistability Fig. 1.2(d,e).

The normal forms for supercritical and subcritical Hopf bifurcations are given respectively by:

$$\dot{r} = (\rho - r^2)r, \ \dot{\theta} = b_1\omega - b_2 r^2 \quad \text{(supercritical)}, \tag{1.10}$$

$$\dot{r} = (\rho + x^2)r, \ \dot{\theta} = b_1\omega - b_2 r^2 \quad \text{(subcritical)}, \tag{1.11}$$

where ρ is the bifurcation parameter Marsden and McCracken (1976). Further details and applications of Hopf bifurcation are discussed in the next section.

Homoclinic Bifurcation: A homoclinic bifurcation occurs when a system's limit cycle collides with a saddle point and collapses, leaving only the saddle point. The trajectory asymptot-

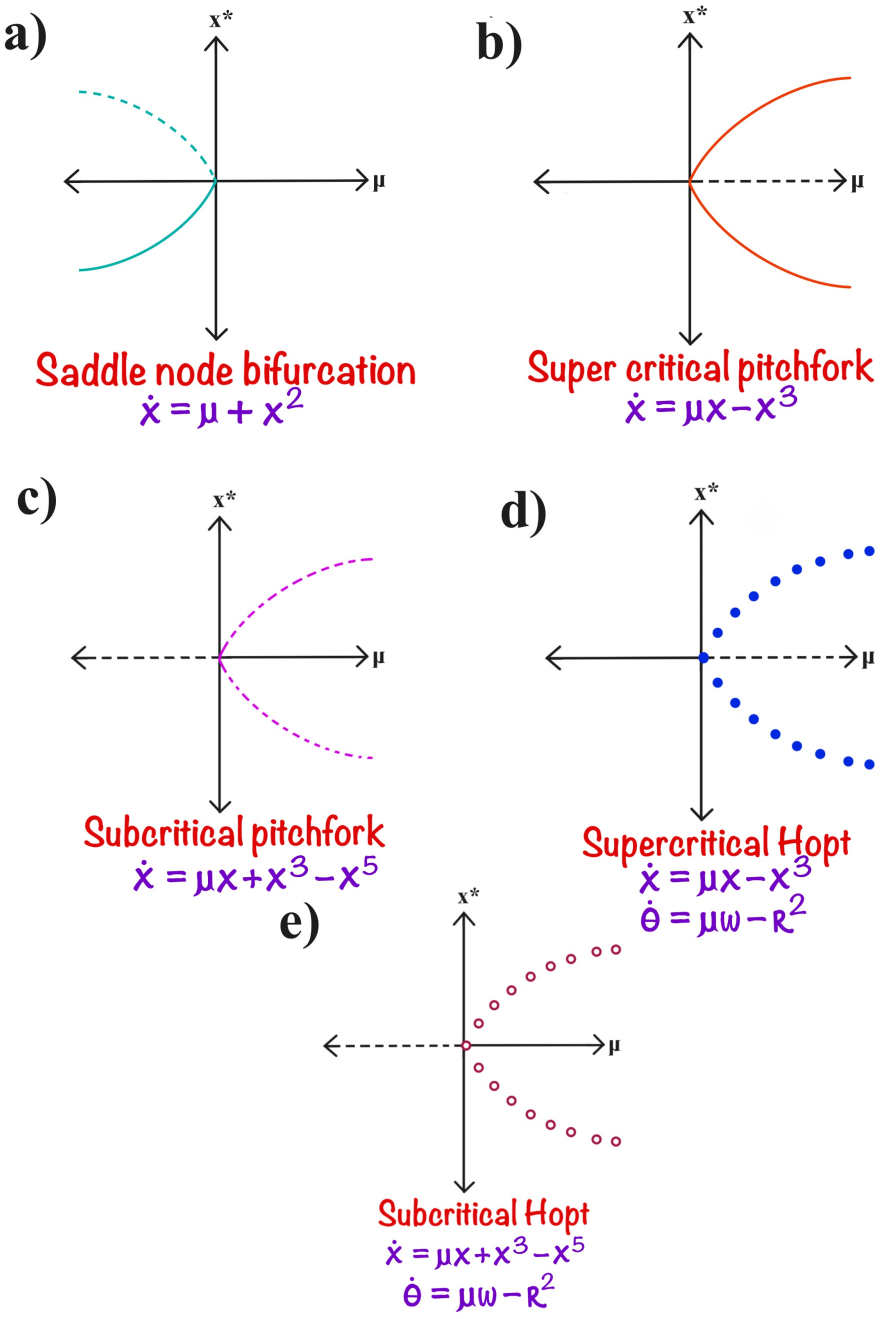

Figure 1.2: Figure illustrating different forms of bifurcation. Solid lines represent stable fixed points; dashed lines denote unstable fixed points; filled circles indicate stable limit cycles; and empty circles represent unstable limit cycles.

ically returns to the saddle point. These bifurcations are often associated with bistability, as the system typically exhibits coexistence of a stable fixed point and a stable limit cycle before the bifurcation Kuznetsov (2013).

The normal form for homoclinic bifurcation is:

$$\dot{x} = y, \tag{1.12}$$

$$\dot{y} = -x + \mu y - x^2, \tag{1.13}$$

where μ is the bifurcation parameter.

1.2 Uncoupled Stuart-Landau oscillators

Earlier, we discussed the existence of a limit cycle in an uncoupled Stuart-Landau (SL) oscillator. The normal form of a Hopf bifurcation is a generalized form of the SL equation (Eq. 1.6) presented earlier and is given by Eq. 1.10. To simplify the analysis, we consider a reduced form of Eq. 1.10 that focuses solely on the bifurcation parameter responsible for the Hopf bifurcation while fixing $b_1 = 1$ and $b_2 = 0$ Marsden and McCracken (1976). The resulting dynamical equation is:

$$\dot{z}(t) = \left(a - |z(t)|^2\right) z + \imath \omega z, \tag{1.14}$$

where z is a complex variable representing the dynamical state of an oscillator, and ω is its intrinsic frequency. This system has an unstable fixed point at the origin, which acts as the unstable focus of a stable circular limit cycle of radius $\sqrt{a}$. The parameter a is referred to as the bifurcation parameter.

Since Eq. 1.10 is the normal form of a Hopf bifurcation, any system undergoing a Hopf bifurcation can be locally represented by this equation at the critical point Kuznetsov (2013). To demonstrate this, consider a general two-dimensional dynamical system:

$$\dot{x} = f(x, y, \mu), \quad \dot{y} = g(x, y, \mu), \tag{1.15}$$

where μ is the bifurcation parameter. In a Hopf bifurcation, a stable fixed point becomes unstable, and a stable limit cycles emerge. This occurs when the eigenvalues of the system cross the imaginary axis. The bifurcation process can occur in two scenarios:

1. A real eigenvalue crosses the imaginary axis (saddle-node bifurcation).

2. A pair of complex conjugate eigenvalues $\pm \imath \omega$ cross the imaginary axis simultaneously.

The second scenario describes a Hopf bifurcation. Assuming the bifurcation occurs at $\mu = 0$, the eigenvalues are $\lambda_{\pm} = \pm \imath \omega$ at $\mu = 0$. For $\mu \neq 0$, the eigenvalues are $\lambda_{\pm} = \sigma(\mu) \pm \imath \omega$, where $\sigma(0) = 0$ and $\sigma(\mu)$ is a smooth function of μ. The simplest assumption is $\sigma(\mu) = \mu$, which satisfies all conditions Kuznetsov (2013); Kuramoto (1984). Hence, a stable Limit cycle exists for $\mu > 0$ and a stable fixed point exists for $\mu < 0$.

The Jacobian matrix at the critical point is given by:

$$J = \begin{bmatrix} \sigma(\mu) & \omega \\ -\omega & \sigma(\mu) \end{bmatrix}.$$

Approximating the dynamics near the bifurcation, we have:

$$\begin{bmatrix} \dot{x} \\ \dot{y} \end{bmatrix} = \begin{bmatrix} \mu & \omega \\ -\omega & \mu \end{bmatrix} \begin{bmatrix} x \\ y \end{bmatrix} + \text{Higher-order terms.} \tag{1.16}$$

Expressing this in complex form as $z = x + \imath y$, the equation becomes:

$$\dot{z} = \mu z - \imath \omega z + \text{Higher-order terms.} \tag{1.17}$$

The SL oscillator must exhibit rotational symmetry, meaning the dynamics are invariant under the transformation $z \to z\exp(\imath\kappa)$. This phase invariance restricts the form of the higher-order terms. The simplest nonlinear term consistent with this symmetry is $|z|^2 z$ García-Morales and Krischer (2022). Thus, the generalized dynamical equation becomes:

$$\dot{z} = \mu z - \imath \omega z - |z|^2 z. \tag{1.18}$$

This equation describes the universal behavior of systems undergoing a Hopf bifurcation.

1.3 Coupled Stuart-Landau Oscillators

In the previous section, we discussed how many natural systems can be effectively described by nonlinear oscillators. Often, these systems are not isolated, but interact with each other, and such interactions can have a significant impact on the system's dynamics. For instance, weak coupling between nonlinear oscillators can lead to synchronization Tumash et al. (2019); Strogatz (1994), a nonlinear phenomenon observed in various systems, such as the flashing of fireflies, Josephson junctions, and more Strogatz (1994). While synchronization is commonly modeled by phase oscillators with nonlinear sinusoidal coupling, certain systems require the consideration of higher-dimensional nonlinear oscillators to account for their more complex behavior.

A particularly important phenomenon arising from the interaction between nonlinear oscillators, which cannot be captured by phase oscillators, is the "quenching of oscillations", a process that requires the presence of a limit cycle. Therefore, it is crucial to study synthetic models of coupled nonlinear oscillators in order to explore the impact of coupling strength and coupling

structure on the overall dynamics of the system.

In this thesis, we focus on the suppression of oscillations. Coupled Stuart-Landau (SL) oscillators provide a prototypical model for understanding the origins of "oscillator death" and the associated changes in the system's stability. Oscillator death can be categorized into two primary forms: "Amplitude Death (AD)" and "Oscillation Death (OD)". These categories are distinguished by the spatial distribution and symmetry of the fixed points of the system.

Amplitude Death (AD): Amplitude death is a form of oscillation suppression where the trivial fixed point of the uncoupled system becomes stabilized due to coupling, within a specific parameter range. The position of the fixed point does not depend on the parameter, and all oscillators in the system eventually converge to the same fixed point. Consequently, AD is also referred to as a "homogeneous steady state" (HSS). The coupled system stabilizes AD through a Hopf bifurcation, while maintaining parity symmetry Koseska et al. (2013a); Saxena et al. (2012).

Earlier investigations of coupled SL oscillators have identified various mechanisms that can lead to oscillation quenching, such as time delays Reddy et al. (1998), conjugate coupling Hens et al. (2013); Wang and Zou (2021); Karnatak et al. (2007), dynamical coupling Konishi (2003), or frequency mismatches Koseska et al. (2013b), all of which contribute to the damping of oscillations. For example, Prasad *et al.* observed that, for a system of Hindmarsh-Rose neuron oscillators interacting through nonlinear coupling, a death state could be reached for sufficiently strong coupling Prasad et al. (2010).

Oscillation Death (OD): In contrast to AD, the phenomenon of oscillation death (OD) involves oscillators that settle into different fixed points, which depend on the system's governing equations. OD is often referred to as an "inhomogeneous steady state" (IHSS), since the oscillators may converge to two or more fixed points, with the exact points depending on the coupling and symmetry-breaking bifurcations. Examples of OD include phenomena like cell differentiation Koseska et al. (2010), where different cells might oscillate in distinct ways due to varying interactions between them Banerjee and Ghosh (2014b).

Applications: AD can find application is systems where disruption or stabilization of oscillation is required such as pathological diseases like Alzheimer and Parkinsons disease or laser systems where fluctuations need to be reduced. In an Parkinson's patient there is a loss of dopamine which in turn affects the basal ganglia in brain increasing the amount of low frequency signals reponsible for symptoms of like tremors and rigidity. Deep brain stimulation is train of high frequency pulse which suppresses the low frequency waves through feedback loop. It has been seen that quenching of low frequency waves can reduce the symptoms.Davidson et al. (2012) Another great example of amplitude death can be observed in external-cavity diode laser systems (ECDL) using optical injection. An ECDL is a diode laser with an external cavity that provides self-feedback, which often leads to chaotic fluctuations and low-frequency pulsations. To stabilize these fluctuations, a master laser is coupled(with time delay) with the ECDL (acting as the slave laser). As the delayed optical injection from the master laser to the slave laser increases, these undesired chaotic outputs can be suppressed, leading to amplitude death. This is significant for enhancing laser performance in practical applications like optical communication, where stability is crucial. Kumar et al. (2008); Kim et al. (2005) A few other systems manifesting quenching of oscillations are weather and climate systems Gallego and Cessi (2001), laser Kim et al. (2005), electronic circuits Banerjee and Ghosh (2014a).

In the following we define an order parameter which quantifies the variance of fluctuation of the dynamical variables over a time span, which tends to 0 for both OD and AD cases:

$$A = \frac{1}{N}\sum_{i=1}^{N}(\langle x_i\rangle_{max,t} - \langle x_i\rangle_{min,t}),\ E = \frac{\sum_{i=1}^{N}|z_i|^2}{N}. \tag{1.19}$$

Here $\langle x_i\rangle_{max,t}$ and $\langle x_i\rangle_{min,t}$ represent the maximum and minimum value, respectively, of x over time t. For the numerical purpose, if $0 < E < 0.001$ and $0 < R < 0.001$, we infer that the system has reached the state of AD. Moreover, to understand phase coherence, we use another order parameter, R, which takes 1 for the synchronized state and 0 for the incoherent state. The order parameters are described by the following equation,

$$R = \left|\frac{\sum_{i=1}^{N} e^{i\theta_i}}{N}\right|. \tag{1.20}$$

These order parameters have been used throughout the next two chapters to detect the presence

Name	A	E
AD	=0	=0
OD	=0	$\neq 0$
OS	$\neq 0$	$\neq 0$

Table 1.1: Amplitude (A) and oscillation (E) death measures for different states.

of AD/OD and phase coherence.

1.4 Networks

Pairwise Networks: Complex pairwise networks consist of basic structural units called *nodes*, which are connected to each other through *edges*. Mathematically, a network is represented by an adjacency matrix A, where the ij^{th} element denotes the connection between the i^{th} and j^{th} nodes. For an unweighted adjacency matrix, a connection between nodes i and j is represented by a value of 1, while no connection is indicated by 0 Albert and Barabási (2002); Barabási (2016). To understand the structural properties of the nodes, various centrality measures, such as degree, clustering coefficient, betweenness centrality, and closeness centrality, are commonly used Newman (2010); Albert and Barabási (2002). Some of these properties are defined below:

Degree: The degree of a node v_i in a network is defined as the number of edges incident to v_i, and is given by:

$$k_i = \sum_{j=1}^{N} A_{ij}$$

where k_i is the degree of node v_i and N is the total number of nodes.

Clustering Coefficient: The clustering coefficient of a node i is defined as the ratio of the number of actual links among the neighbors of node i to the maximum possible number of links that could exist among those neighbors Albert and Barabási (2002).

Betweenness Centrality: Betweenness centrality measures the fraction of shortest paths that

pass through a node. It quantifies the control that a node exerts over the flow of information in the network.

These properties provide insight into the role of individual nodes within a network. For example, a node with high betweenness centrality and low degree often connects two distinct clusters or communities, while a node with a high degree and low clustering coefficient may serve as a hub in the network.

Additionally, to study the network from a global structural perspective, properties like the degree distribution, average clustering coefficient, and average shortest path length are analyzed. These are defined as follows:

Average Degree: The average degree $\langle k \rangle$ of a network is the sum of the degrees of all nodes divided by the total number of nodes N:

$$\langle k \rangle = \frac{1}{N} \sum_{i=1}^{N} k_i$$

Average Clustering Coefficient: The average clustering coefficient is the mean of the clustering coefficients of all nodes in the network.

Average Shortest Path Length: The average shortest path length is the mean of the shortest path lengths between all possible pairs of nodes.

A network is fundamentally a structure comprising nodes and links. The challenge lies in arranging these links in a way that captures the complexity and apparent randomness observed in real-world systems. Various network models, such as regular networks, small-world networks, and scale-free networks, can be used to represent different types of real-world systems.

Network Models: *Regular Networks:* In a regular network, each node is connected to its nearest neighbors. *Small-World networks:* By rewiring the edges of a regular network with a probability p, long-range connections are introduced, resulting in randomness. For certain values of p, the network exhibits low average shortest path length and high average clustering coefficient, which are characteristic of small-world networks. The small-world phenomenon, often referred to as "six degrees of separation," suggests that any two people on Earth can be connected through a chain of no more than six mutual connections Albert and Barabási (2002);

Barabási (2016); Newman (2010).

Erdős–Rényi Random Networks (ER Networks): In Erdős–Rényi random network, the degree distribution follows a Poisson distribution. One algorithm to generate a random is to randomly connect two nodes of a network (of size N) with probability p. ER Random networks generated with the same parameters N and p will have slightly different structures. In these networks, most nodes have similar degrees, making hubs (nodes with exceptionally high degrees) unlikely Albert and Barabási (2002).

Scale-Free Networks: Scale-free networks, characterized by a "rich-get-richer" principle, are designed through the process of preferential attachment. In this process, we begin with a small number of nodes and progressively add new nodes i, with the probability of connecting to an existing node j being proportional to the degree of node j. This leads to a network where a few nodes have very high degrees, while most nodes have low degrees, resulting in a power-law degree distribution. The term "scale-free" refers to the fact that the degree distribution retains its form at different scales, similar to the properties of fractals Albert and Barabási (2002); Barabási (2016); Newman (2010).

Application to Real-World Systems: In this thesis, we initially apply our dynamical models to globally coupled networks, where all oscillators interact with each other. However, for our models to be applicable to real-world systems, it is essential to consider networks that are not fully connected, as most real-world systems involve local or limited interactions. Extrapolating our results from globally coupled networks to model networks is an important step in assessing the robustness of our models and their applicability to more realistic, heterogeneous network structures.

Higher-order Networks: The recognition of irreducible higher-order interactions has a long-standing history. These interactions, which involve three or more entities, cannot be fully captured by simply aggregating pairwise interactions. In linear systems, the overall influence on each component can be decomposed into a sum of pairwise interactions. However, in nonlinear systems, higher-order interactions are essential for an accurate representation of the dynamics Jalan (2023); Battiston et al. (2020).

To illustrate this concept, consider an example inspired by social science, focusing on collab-

oration networks. Imagine mapping the scientific literature as a large network, where nodes represent researchers from various disciplines, and edges (connections) represent co-authored papers. Consider three specific scientists, A, B, and C. If the literature contains at least one paper co-authored by A and B but not C, another co-authored by B and C but not A, and a third co-authored by A and C but not B, these three interactions form a triangle in the network, which can be decomposed into three separate pairwise (dyadic) interactions.

However, in a different scenario, suppose there is a single paper co-authored by all three scientists, A, B, and C. In this case, the relationship among A, B, and C forms a triangle that reflects a genuine triadic interaction, which cannot be reduced to a sum of dyadic interactions. This example underscores how higher-order interactions capture more complex relationships that are not apparent in pairwise interactions. Such interactions are crucial in diverse contexts, including social dynamics within groups, catalytic processes in chemistry, and innovations emerging from the integration of multiple technologies Jalan (2023); Battiston et al. (2020). Including these higher-order interactions in models not only enhances their realism but also uncovers new questions and insights that might otherwise remain hidden or misinterpreted in pairwise frameworks. Similar interactions have been observed in complex systems such as brain networks Santos et al. (2023), social networks Zlatić et al. (2009); Zhu et al. (2018), and biological networks Feng et al. (2021); Klamt et al. (2009).

Higher-order interactions in networks are typically represented using hypergraphs. A hypergraph $H = (V,E)$ consists of a set of nodes $V = \{V_1, V_2, \ldots, V_N\}$ and a set of hyperedges $E = \{e_1, e_2, \ldots, e_M\}$, where N and M denote the number of nodes and hyperedges, respectively. Each hyperedge e_i is a multiset of subsets of V, and the number of nodes involved in a hyperedge is called its cardinality (or order). For instance, a hyperedge of order Q connects Q nodes, capturing the group interaction among these Q entities. A simplex corresponds to a complete hyperedge, where a k-simplex includes all possible subsets of its $k+1$ vertices as faces. For example, a 2-simplex (a triangle) corresponds to a hyperedge connecting three vertices $\{a,b,c\}$ (triadic interaction), and all its subsets $\{\{a,b\},\{a,c\},\{b,c\},\{a\},\{b\},\{c\}\}$ represent pairwise (dyadic) and individual (self) interactions.

To study the effects of higher-order interactions in coupled Stuart-Landau oscillators, we focus on triadic interactions, where the dynamics of three interacting oscillators cannot be reduced to simpler pairwise terms.

1.5 Dynamical modelling of Brian Netwroks

The human brain is an immensely complex system, composed of billions of neurons interacting through trillions of synaptic connections. These interactions are not static—they evolve in time, producing patterns of activity that underlie perception, cognition, and behaviour. Dynamical modelling provides a mathematical framework to describe and understand these time-evolving processes, using tools from nonlinear dynamics, network theory, and statistical physics. Rather than treating the brain as a static structure, dynamical models view it as a system whose state changes continuously, influenced by both internal interactions and external inputs Breakspear et al. (2006). A simple brain network model consists of firing neurons acting as nodes connected through synapses defining interactions between the pairs of neurons. Dynamical behaviors of an individual neuron/node have been successfully cast by the models like Hodgkin-Huxley, and Fitzuh-Nagumou Gerster et al. (2020), in which two-state variables of the corresponding differential equations represent the membrane potential and ion channel conductance. However, in large-scale brain networks, information about the dynamical evolution of each neuron is relatively irrelevant. Few well-known models representing large-scale brain dynamics, such as the neuronal mass model and the brain network model (BNM), present ensemble approach in which the dynamics of a patch of the cortex (a local population of neurons) are represented by a small set of differential equations Breakspear (2017). In the BNM approach, these patches of the cortex are considered as units or nodes coupled with each other according to their anatomical connectivity (edge) patterns. Various attempts have been made in neuroscience to study neurological conditions by modeling them as dynamical systems. A common approach involves comparing the functional connectivity derived from empirical data with that generated by dynamical models Liu et al. (2023); Cabral et al. (2012). To gain a deeper understanding of the dynamical behavior of a system, researchers have also analyzed the time evolution of functional connectivity using methods such as the multiplication of temporal derivatives and functional connectivity dynamics matrices Shine et al. (2015); Hutchison et al. (2013).

1.6 Postictal generalized EEG suppression

Postictal generalized EEG suppression (PGES) is a well-established electrophysiological phenomenon associated with an increased risk of SUDEP (Sudden Unexpected Death in Epilepsy). A landmark prospective multicenter study (called MORTEMUS) published in the prestigious journal Lancet Neurology confirmed the presence of PGES in all the observed cases of SUDEP Ryvlin et al. (2013). PGES is defined as diffuse scalp EEG background suppression $< 10\mu V$ observed postictally (post seizure). The "G" in PGES represents spatial ("generalized or diffuse") suppression observed in scalp EEG. Thus, during the PGES phenomenon, there is unequivocal generalized amplitude suppression as recorded by scalp EEG Lhatoo et al. (2010a); Asadollahi et al. (2018).

Examples of a few intracranial EEG studies during PGES are in references (Bauer et al. (2017); Grigorovsky et al. (2020)). Similarly, over the last five years, we had collated and curated rare intracranial EEG (stereo EEG) data when patients had generalized tonic-clonic seizures followed by scalp EEG confirmed PGES. These patients had simultaneous scalp EEG and invasive stereo EEG recordings from multiple brain regions during epilepsy surgical evaluation. In addition, we recorded invasive EEG from thalamic subregions through IRB-approved protocol. Thus we have rare recordings from cortical and thalamic brain regions during scalp EEG confirmed PGES. To date, no center has reported human thalamocortical invasive EEG changes during PGES. Thus our data is novel and is uniquely poised to provide insights into thalamocortical changes during the scalp and invasive EEG-confirmed amplitude suppression (PGES).

During PGES, there is a diffuse scalp EEG suppression, and we have selected the cases where there is confirmed thalamocortical invasive EEG suppression (as in Fig. 1.3). This Letter only used invasive stereo depth electrode recordings for signal processing and modeling. Further we wish to highlight that for the signal processing, we have only used stereo depth electrode recordings. These recordings (also sometimes called local field potentials-LFP) from clinical depth electrodes are used in developing brain-computer interfaces (like language and motor mapping and modulation), seizure mapping, and subsequent surgical resection with the underlying priori that bipolar montage-derived LFPs from invasive EEG electrodes have high signal fidelity and represent local neural ensemble activity. During PGES, we have confirmed suppression of neu-

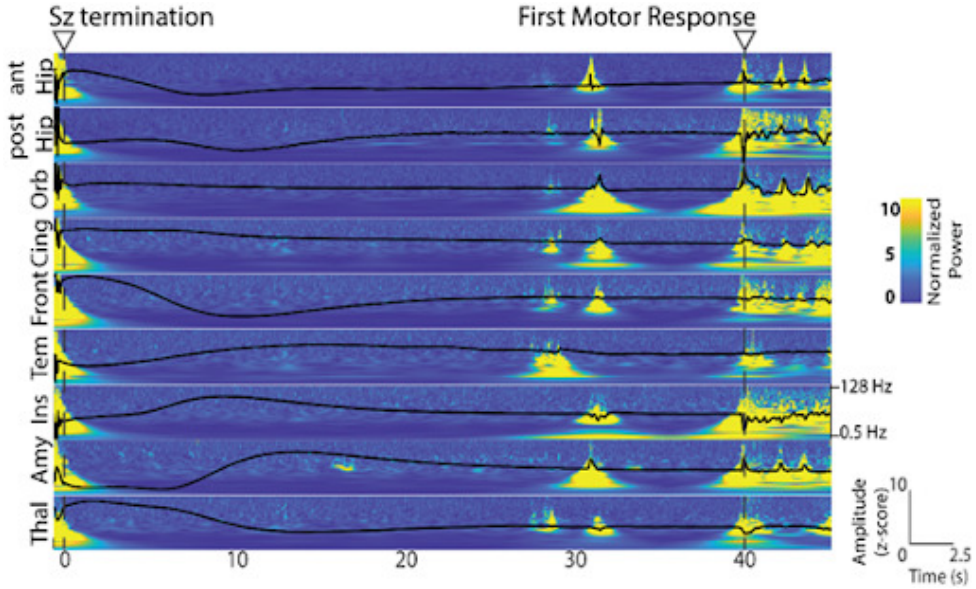

Figure 1.3: Time-frequency representation from Stereo EEG trace showing absence of neural activity between 0-29 secs of PGES. First motor response (t 40 secs) was preceded by burst of neural activity at 30 secs. Thal- centromedian thalamus, Amy-amygdala, Ins-insula, Tem-lateral temporal, Orb-orbitofrontal, Front-lateral frontal, an. And post hippocampus, cing-ant. cingulate. PGES-postictal generalized EEG suppression

ral activity from direct invasive EEG recordings from the thalamocortical regions (like Fig. 1.3), and this data was used for modeling.

1.7 Thesis overview

In this section, we provide a roadmap to guide readers through the various chapters.

- In Chapter 2, we introduce a scheme that combines dissimilar couplings and repulsive feedback links for the interactions of Stuart Landau oscillators to get two different types of quenching of oscillations, namely amplitude and oscillations death. We analytically derive the conditions required for the amplitude death. Finally, we discuss the similarities of the quenching of oscillations phenomenon with the postictal generalized EEG suppression in convulsive seizures.

- In Chapter 3, we move on to introduce a scheme to incorporate higher-order interactions

which can not be decomposed into pairwise interactions, and investigates the dynamical evolution of Stuart-Landau oscillators under the impression of such a coupling. We discover a oscillator death state through first-order (explosive) phase transition in which a single, coupling-dependent stable death state away from the origin exists in isolation without being accompanied by any other stable state usually existing for pair-wise couplings. We call such a state a solitary death state. Contrary to wide-spread subcritical Hopf bifurcation, here we report homoclinic bifurcation as an origin of the explosive death state. Moreover, this explosive transition to the death state is preceded by a surge in amplitude, and followed by a revival of the oscillations. The analytical value of the critical coupling strength for the solitary death state agrees with the simulation results.

- In Chapter 4, we study the post-ictal generalized EEG suppression occurring in patients with generalized tonic-clonic seizures. It consists of marked suppression of low-frequency waves before returning to normal brain function. Moreover, often, the path of return to normal brain function is accompanied by a mixed state consisting of suppression and high amplitude oscillation. We explain these phase transitions from the standpoint of bifurcation theory to attain a proper dynamical model that mimics similar behaviour. We find that various stages of postictal generalized EEG suppression are best modelled via the normal form of sub-critical hopf bifurcation.

- Chapter 5 conclude the study along with future research prospects.

Chapter 2

Oscillation Quenching in Stuart-Landau Oscillators via Dissimilar Repulsive Coupling

2.1 Introduction

Coupled Stuart Landau (SL) oscillators can display a wide range of emerging phenomena, such as synchronization, pattern formation, quenching of oscillations, etc. Especially quenching of oscillations arising due to coupling between the pairs of oscillators has drawn considerable attention from the nonlinear dynamics community due to the widespread occurrence of this phenomenon in many natural systems.

A set of identical SL oscillators ($\omega_i = \omega_j$) is unable to show quenching of oscillation with a simple diffusive coupling through the z variable. However, different coupling schemes play different governing roles in determining steady-state behaviors. For instance, the oscillation death state is achieved for the coupling term being present only in the real or imaginary part of

z Koseska et al. (2013b). In fact, there could be a transition from the oscillatory state (OS) to AD when z is coupled diffusively with its conjugate z^* Wang and Zou (2021). Moreover, in the identical oscillators, repulsive feedback coupling Hens et al. (2013); Nandan et al. (2014) and diffusive coupling in dissimilar (also referred to as conjugate) variables Karnatak et al. (2007); Saxena et al. (2012) can steer AD and OD. In non-identical oscillators, frequency mismatch and coupling strength are enough to bring the oscillator death, even for simple diffusive coupling via the z variable. Non-identical SL oscillators coupled through diffusive couplings on small-world networks have shown to support OD Hou and Xin (2003); Rubchinsky and Sushchik (2000), and on scale-free networks have shown to yield a complete AD state Liu et al. (2009). Lately, the first-order abrupt transition to AD, popularly referred to as explosive death, has become a topic of great interest due to the theoretical curiosity fueled by observations of the phenomenon's existence in many real-world systems. The first-order transition to AD can be successfully induced in coupled oscillators via an environmental coupling scheme in a single layer Verma et al. (2018a, 2019) as well as in multiplex networks Verma and Ambika (2021); Maslennikov and Nekorkin (2018).

Further, there have been persistent efforts to model large-scale brain networks using coupled oscillators on networks O'Sullivan-Greene et al. (2009); Kim et al. (2018); Bauer et al. (2017); Grigorovsky et al. (2020). For example, few previous studies have considered simple linear phase oscillators to understand various emerging dynamical features of brain networks O'Sullivan-Greene et al. (2009). A simple brain network model consists of firing neurons acting as nodes connected through synapses defining interactions between the pairs of neurons. Dynamical behaviors of an individual neuron/node were first studied by the Hodgkin-Huxley model, explaining the initiation and propagation of action potential in neurons Hodgkin and Huxley (1952). Subsequently, other models like Fitzhugh-Nagumo (explaining spiking in neurons) and Hindmarsh-Rose (explaining spiking-bursting in neurons) FitzHugh (1961); Hindmarsh and Rose (1984) were discovered. However, in large-scale brain networks, the collective behavior of the nodes was considered to be quite low-dimensional, and information about the dynamical evolution of each neuron was shown to be relatively irrelevant Breakspear (2017); Pathak et al. (2022). A well-known model representing large-scale brain dynamics is the neural mass model Jansen and Rit (1995), which presents an ensemble approach in which the dynamics of a patch of the cortex (a local population of neurons) are represented by a set of differential equations reduced in dimension Breakspear (2017). Further advances in this field led to the dis-

covery of more realistic models, such as the whole brain model and the brain networks model, where brain areas were treated as nodes in a coupled dynamical system. These patches of the cortex are considered as units or nodes coupled with each other according to their anatomical connectivity (edge) patterns. Simplified models like the Kuramoto oscillator Breakspear et al. (2010) and SL oscillators Demirtaş et al. (2017); López-González et al. (2021); Kim et al. (2018) have been used in a similar fashion to portray large-scale brain dynamics. Different models are constructed such that they can explain the phenomenon of interest Pathak et al. (2022); Breakspear et al. (2010).

Synchronized activities among the different brain regions have been associated with the onset of the seizure from the pre-seizure region O'Sullivan-Greene et al. (2009). It is common knowledge that soon after the generalized tonic-clonic seizures, the brain state exhibits a transition to an isoelectric EEG state, with the existence of a profound scalp EEG voltage attenuation (< 10 microvolts), referred to as the postictal generalized EEG suppression (PGES) Bauer et al. (2017); Grigorovsky et al. (2020). While we do not claim that the model presented here provides a mechanism behind the occurrence of PGES in the human brain, the phenomenon depicted by this model bears a close resemblance to PGES. Furthermore, to make the modelling of PGES more realistic, for the coupling matrix of Eq. 2.2, we have considered the functional correlation matrices generated for the EEG time series data from brain during seizure.

First, we develop a theoretical framework to analyze amplitude death in coupled SL oscillators on complex networks. Earlier theoretical works on SL oscillators pertain to the linear stability analysis for direct mean-field diffusive coupling Mirollo and Strogatz (1990) and diffusive conjugate coupling Wang and Zou (2021) on globally coupled and star networks FRASCA et al. (2012). We consider SL oscillators with dissimilar repulsive feedback couplings and develop an analytical approach that is independent of the size of the underlying coupling network. The method is a generalized one as it facilitates calculations of necessary and sufficient conditions to attain amplitude death for other coupling forms. The key lies in the fact that the analysis uses a generalized form of coupling matrix, providing it an edge over previously existing frameworks. Then, we numerically study the dynamical behaviors of this setup on various network architectures, namely, globally coupled networks, regular lattice networks, Erdös-Renyí (ER) random networks. Finally, we numerically analyze the results of Eq. 1 with the functional coupling matrices generated from real time series EEG data of patients, and discuss the similarity between

the phenomenon depicted by the model with PGES.

2.2 Model

Dynamical evolution of an uncoupled SL oscillator is governed by Eq. 1.6. Upon substituting $z = x + iy$, the resulting equation is,

$$\dot{x}_k = P_k^x,\ \dot{y}_k = P_k^y \tag{2.1}$$

where,

$$P_k^x = (1 - x_k^2 - y_k^2)x_k - w_k y_k,\ P_k^y = (1 - x_k^2 - y_k^2)y_k + w_k x_k$$

An introduction of the dissimilar repulsive feedback coupling between a pair of connected nodes through both the x and y coordinates results in the following equation,

$$\dot{x}_k = P_k^x - \frac{\varepsilon_x}{N}\sum_{j=1}^{N} A_{jk}(y_j + x_k), \dot{y}_k = P_k^y - \frac{\varepsilon_y}{N}\sum_{j=1}^{N} A_{jk}(x_j + y_k) \tag{2.2}$$

Here A_{jk} is the adjacency matrix representing the underlying network structure. For an unweighted network, its elements take the value 1 when j^{th} and k^{th} nodes are connected, and 0 otherwise. Whereas, for a weighted network, the elements of the adjacency matrix are represented by the interaction weights. For identical oscillators, it has been found that an introduction of the similar diffusive coupling does not yield oscillator death (see 2.4.1), whereas dissimilar repulsive feedback links bring oscillator death. Further, we consider different cases with the nodes having different coupling schemes and couplings being in only one dimension. We consider the weighted interaction matrix generated from the post-seizure data. First, we model the eight intracranial channels of the brain as non-identical Stuart-Landau oscillators on a directed weighted network. The dynamical equation of such nodes can be given by Eq. 2.2 with ω chosen from a Lorentzian frequency distribution with parameters corresponding to the frequency band. Further, we study the dynamics of each node and the network as a whole.

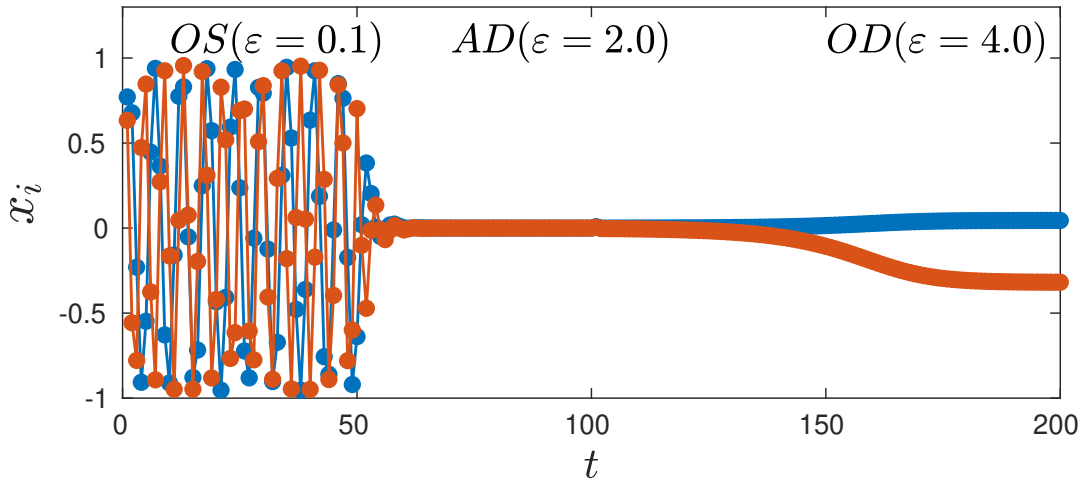

Figure 2.1: x_i vs t plot depicting three different dynamical states for two randomly selected nodes form a network of $N = 1000$ (Eq. 2.2). Lorentzian frequency distribution parameters are $\omega_0 = 2.0$ and $\Delta = 0.30$.

2.3 Analytical Calculation

Let us now provide the mathematical formalism to analyze the stability of coupled SL oscillators on various setups. First, we present generalized characteristic equation the coupled SL oscillators on globally coupled networks. Thereafter, we consider globally coupled nodes having dissimilar repulsive feedback couplings and try to solve using the generalized characteristics equation. We further mix various kinds of couplings and study the dynamical evolution of the coupled oscillators for the mixed setup.

At first, let us consider a setup of globally coupled SL oscillators with a generalized form of the coupling matrix F, which can be changed later according to the different setups. The generalized coupled differential equations for globally coupled networks of the Stuart Landau oscillators can be written as,

$$\begin{bmatrix} \dot{x}_k \\ \dot{y}_k \end{bmatrix} = \begin{bmatrix} (1-x_k^2-y_k^2)x_k - i\omega_k y_k \\ (1-x_k^2-y_k^2)y_k + i\omega_k x_k \end{bmatrix} + F(x_j, x_k, y_j, y_k)$$

The corresponding Jacobian matrix at the fixed point corresponding to AD takes the form 1.1.2:

$$|I\lambda - M| = \begin{pmatrix} M_1+F_1 & . & . & F_1 \\ F_2 & M_2+F_2 & . & . \\ F_i & . & M_i+F_i & . \\ F_N & . & . & M_N+F_N \end{pmatrix}$$

where, $M_i = \begin{pmatrix} \lambda - a_1 & -\omega_i \\ \omega_i & \lambda - a_2 \end{pmatrix}$. However, a_1, a_2 and F_i vary in accord with the coupling scheme of each node and λ is the eigenvalue of the Jacobian matrix. To deduce the stability conditions for the AD state, the challenge lies in solving the characteristic equation for the corresponding Jacobian matrix (M) given by $det(I_{2N}\lambda - M) = 0$. Let us first solve $det(I_{2N}\lambda - M) = 0$, for which we use the following lemma.

Matrix-Determinant Lemma: If X is $n \times n$, and U and V are $n \times m$ matrices,

$$|X + UV^T| = |X| \times |I_m + V^T X^{-1} U| \tag{2.3}$$

where I_m is an identity matrix of the dimension $m \times m$ and $O_{n\times n}$ is a null matrix of dimension $n \times n$.

Proof:

$$|X + UV^T| = \begin{vmatrix} X+UV^T & U \\ O_{n\times n} & I_m \end{vmatrix} \begin{vmatrix} I_n & O_{n\times m} \\ -V^T & I_m \end{vmatrix} = \begin{vmatrix} X & U \\ -V^T & I_m \end{vmatrix}$$

$$\begin{vmatrix} X & U \\ -V^T & I_m \end{vmatrix} = |X| \times |I_2 + V^T X^{-1} U|$$

using identity for the determinant of block matrices,

$$\begin{vmatrix} A & B \\ C & D \end{vmatrix} = |D| \times |D - CA^{-1}B| \tag{2.4}$$

Next, we apply the following lemma to find out the characteristic equation and the corresponding eigenvalues. $(\lambda I_{2N} - M)$ can be written as;

$$(\lambda I_{2N} - M) = M_d + UV^T$$

where

$$M_d = \begin{bmatrix} M_1 & 0 & 0 & . & . & . \\ 0 & M_2 & 0 & 0 & . & . \\ . & . & . & . & . & . \\ . & . & . & . & . & . \\ 0 & 0 & . & . & . & M_N \end{bmatrix}, U = \begin{bmatrix} F_1 \\ F_2 \\ F_3 \\ . \\ . \end{bmatrix}, V = \begin{bmatrix} I_2 \\ I_2 \\ I_2 \\ . \\ . \end{bmatrix}$$

By using the matrix determinant lemma (Eq. 2.3) and Eq. 2.4 we obtain,

$$\begin{aligned} |\lambda I_{N/2} - M| &= |M_d| \times |I_2 + V^T M_d^{-1} U| \\ &= |M_d| \times |I_2 + V^T (\frac{adj(M_d)}{|M_d|}) U| \\ &= \Pi_{i=1}^{N} |M_i| \times |I_2 + \sum_{i=1}^{N} \frac{adj(M_i) F_i}{|M_i|}| \end{aligned}$$

The generalized characteristic equation are given by,

$$\Pi_{i=1}^{N} |M_i| = 0 \text{ and } |I_2 + \sum_{i=1}^{N} \frac{adj(M_i) F_i}{|M_i|}| = 0 \tag{2.5}$$

where $adj(M_i)$ is the adjoint matrix of M_i. What follows that the characteristic equation reduces to a determinant of a 2×2 matrix which is independent of the size of the network. Moreover, such a reduction allows this scheme to work even when nodes are connected through a different form of the coupling provided each node has the same coupling scheme separately. Let us consider various different cases as test-beds for the analysis. Note that, the simplest case is the one where identical oscillators are diffusively coupled. This coupling does not exhibit AD 2.4.1.

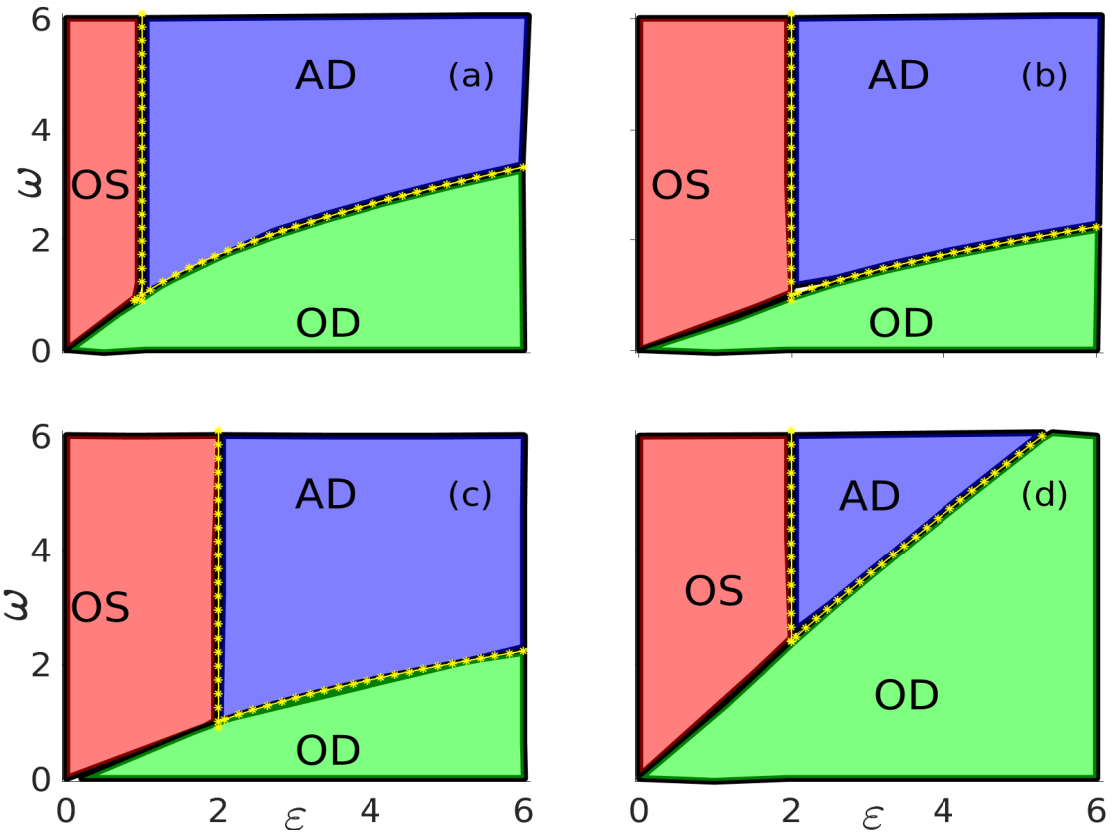

Figure 2.2: Parameter space plot ω vs ε for globally coupled network of size $N = 1000$ consisting of identical oscillators ($\omega_i = \omega_j = \omega \forall i, j$). (a) all nodes having dissimilar repulsive feedback coupling, (b) with half of the nodes having dissimilar repulsive feedback and another half with direct diffusive couplings, (c) dissimilar repulsive feedback coupling via x variable only, (d) dissimilar repulsive feedback coupling via y variable only. The solid black lines represent the transition boundaries calculated numerically, whereas the yellow line represents the analytical region corresponding to the stable origin (AD).

Introduction of dissimilar repulsive feedback coupling: First, we consider a system where all nodes are coupled via dissimilar repulsive feedback. The matrices M_i and F_i which remain the same for all values of i, can be given by, $M_i = \begin{pmatrix} \lambda - 1 + \varepsilon & \omega \\ -\omega & \lambda - 1 + \varepsilon \end{pmatrix}$ and $F_i = \begin{pmatrix} 0 & \varepsilon/N \\ \varepsilon/N & 0 \end{pmatrix}$ and This setup yields the following eigenvalues:

$$\lambda = 1 - \varepsilon \pm \sqrt{\varepsilon^2 - \omega^2},\ \lambda = 1 - \varepsilon \pm i\omega_o \tag{2.6}$$

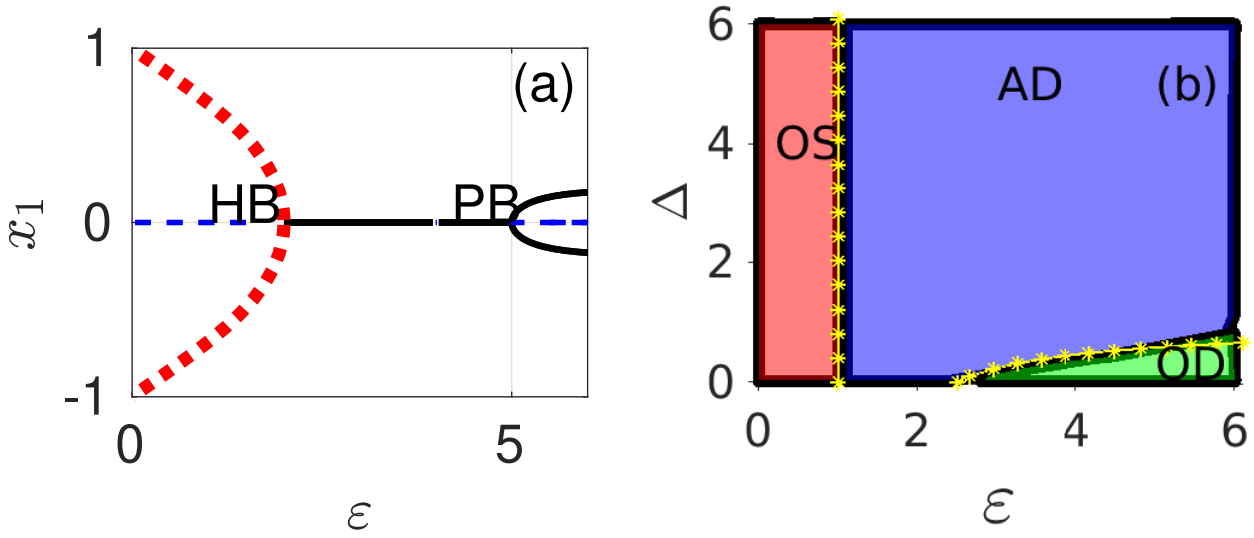

Figure 2.3: (a) Bifurcation plot for dissimilar repulsive coupling via x variables for identical oscillators ($\omega = 2.0$), red dashed line corresponds to stable limit cycle, solid black line represents stable fixed point, and dashed black line represents an unstable limit cycle. (b) Parameter space Δ vs ε plot for non-identical globally coupled networks of size $N = 1000$ and Lorentzian frequency distribution with $\omega_0 = 2.0$. The solid black and yellow dashed lines represent the transition boundaries calculated numerically and analytically, respectively.

The conditions for the origin to be a stable state is satisfied for $Re[\lambda_i] < 0$ for all i. Applying this condition, from Eq. 3.2 we get that for (i) $\varepsilon < \omega$, $\varepsilon > 1$, and (ii) $\varepsilon > \omega$, $1 - \varepsilon \pm \sqrt{\varepsilon^2 - \omega} < 0$ yielding $\varepsilon < (1 + \omega^2)/2$.

Now we consider a system of identical oscillators with two kinds of coupling. Some nodes have coupled via repulsive dissimilar coupling, whereas others have coupled via simple diffusive coupling. The dynamical equation for the simple diffusively coupled nodes can be given by Eq. A1 of the Appendix 2.4.1, whereas the nodes with the repulsive link will be governed Eq. 2.2. Proceeding similarly to the last section, the coupling matrices for the non-repulsive and the repulsive schemes are given by F_1 and F_2, respectively. However, the matrices M_1 and M_2, remain the same for both types of nodes. The M_1,F_1 and F_2 matrix are given by,

$$M_1 = \begin{pmatrix} \lambda - 1 + \varepsilon & \omega \\ -\omega & \lambda - 1 + \varepsilon \end{pmatrix} \text{ and } F_1 = \begin{pmatrix} -\varepsilon/N & 0 \\ 0 & -\varepsilon/N \end{pmatrix} \text{ and } F_2 = \begin{pmatrix} 0 & \varepsilon/N \\ \varepsilon/N & 0 \end{pmatrix}.$$

Next, if we consider a fraction of n nodes coupled with other nodes through the repulsive feedback couplings and a fraction of $1 - n$ nodes coupled without the repulsive links (referred to as the regular nodes), for a globally coupled network, the coupling matrix for the regular nodes

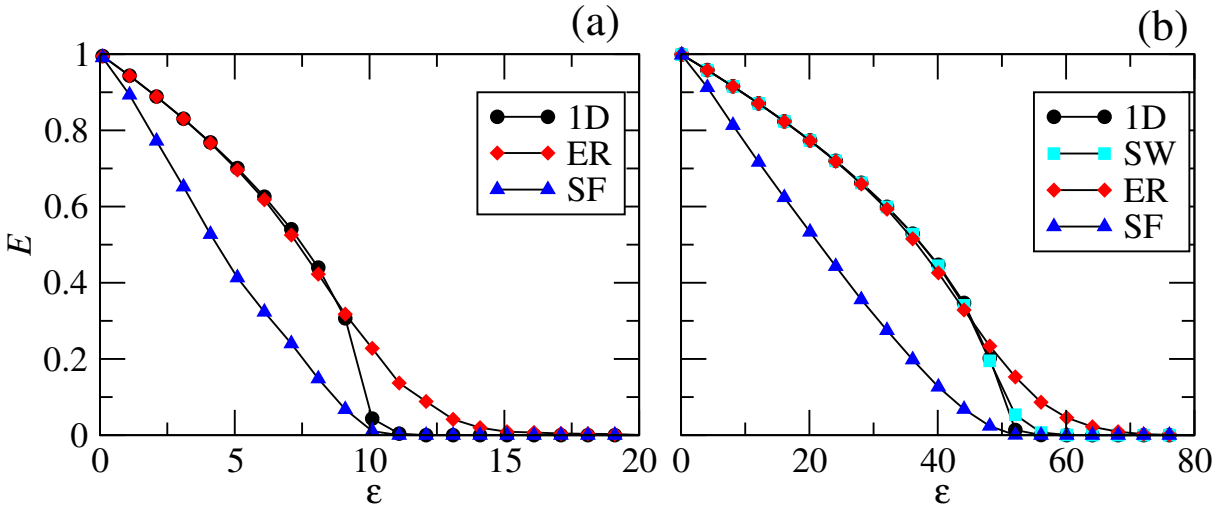

Figure 2.4: E vs ε, for non-identical oscillators with $\omega_0 = 5.0$ for various different network architectures (black circle scale-free, red diamond small-world, blue triangle, and green triangle ER random networks). (a) $N = 100$, $\langle k \rangle = 10$ (b) $N = 1000$, $\langle k \rangle = 20$.

will be given by F_2 and the coupling matrix corresponding to the repulsive nodes will be given by F_1. Substituting them in the Eq. 2.5 leads to the following eigenvalues,

$$\lambda_{1,2} = 1 - \varepsilon n \pm \sqrt{\varepsilon^2 n^2 - \omega^2},\ \lambda_{3,4} = 1 - \varepsilon \pm i\omega \tag{2.7}$$

The real part of these eigenvalues (Eq. 3.3) must be negative for the amplitude death state to occur, which provides us the conditions $n > 1/\varepsilon$ and $\varepsilon < \frac{1+\omega^2}{2n}$. Fig. 2.2(a)-(b) confirms a perfect match between the numerical results and theoretical predictions for both the cases.

Dissimilar repulsive coupling in x variable: For the dissimilar repulsive coupling applied only to the x variable, the dynamics of the corresponding coupled equation will be governed by, $\dot{x}_k = P_k^x - \frac{\varepsilon}{N}\sum_{j=1}^{N}(y_j + x_k),\ \dot{y}_k = P_k^y$ The parameter space diagram obtained through the numerical calculations consists of AD and OS regions only. We find the necessary condition for these states to occur using the expression derived in Eq. 2.5. The matrices required for the calculation are, $M = \begin{pmatrix} \lambda - 1 + \varepsilon & \omega \\ -\omega & \lambda - 1 \end{pmatrix}$ and $F = \begin{pmatrix} 0 & \varepsilon/N \\ 0 & 0 \end{pmatrix}$ substituting them in Eq. 2.5 and solving this equation we get the following eigenvalues,

$$\lambda_{1,2} = \frac{2 - \varepsilon \pm \sqrt{\varepsilon^2 - 4\omega^2 - 4\omega\varepsilon}}{2},\ \lambda_{3,4} = \frac{2 - \varepsilon \pm \sqrt{\varepsilon^2 - 4\omega^2}}{2} \tag{2.8}$$

The necessary conditions can be derived from $Re[\lambda_{1,2} < 0]$ (Eq. 2.8) as $\varepsilon > 2$ and $\varepsilon < (1+\omega^2)/(1-\omega)$ while $\varepsilon^2 - 4\omega^2 - 4\omega\varepsilon > 0$. From $Re[\lambda_{3,4} < 0]$ (Eq. 2.8), one gets the necessary conditions as $\varepsilon > 2$ and $\varepsilon > 1+\omega^2$. However, the condition $2 < \varepsilon < 1+\omega^2$ prevails. This theoretical result matches with the numerical predictions illustrated in Fig. 2.2(c).

Dissimilar repulsive coupling through the y variable: Upon applying the dissimilar repulsive coupling in only y variable, the dynamical equation could be written as,

$$\dot{x_k} = P_k^x, \;\; \dot{y_k} = P_k^y - \frac{\varepsilon}{N}\sum_{j=1}^{N}(x_j + y_k),$$

Again using the same procedure as in the last section, we analytically confirm a match with the numerical results. Here, $M = \begin{pmatrix} \lambda - 1 & \omega \\ -\omega & \lambda - 1 + \varepsilon \end{pmatrix}$ and $F = \begin{pmatrix} 0 & 0 \\ \varepsilon/N & 0 \end{pmatrix}$

Solving the generalized characteristic equation for these M and F values yields the following eigenvalues,

$$\lambda_{1,2} = \frac{2 - \varepsilon \pm \sqrt{\varepsilon^2 - 4\omega^2 + 4\omega\varepsilon}}{2}, \;\; \lambda_{3,4} = \frac{2 - \varepsilon \pm \sqrt{\varepsilon^2 - 4\omega^2}}{2} \tag{2.9}$$

For the origin to be stable, we need $Re[\lambda] < 0$. Therefore, from $Re[\lambda_{1,2}] < 0$ (Eq. 2.9) we derive the conditions $\varepsilon > 2$ and $\varepsilon < (1+\omega^2)/(1+\omega)$, and similarly $Re[\lambda_{1,2}] < 0$ (Eq. 2.9) yields $\varepsilon > 2$ and $\varepsilon < (1+\omega^2)$. The condition $\varepsilon < (1+\omega^2)/(1+\omega)$ is dominant and provides us the governing equation characterizing the transition between the AD and OD states, which also matches with the numerical results (Fig. 2.2(d)).

Non-identical oscillators: Next, we consider the case of non-identical oscillators, i.e., $\omega_i \neq \omega_j$. For Lorentzian intrinsic frequency distribution given by, $g(\omega) = \frac{\Delta}{\pi[(\omega-\omega_o)^2+\Delta^2]}$, one obtains

the following characteristic equation:

$$\frac{1}{\varepsilon^2} = \left[\int_{-\infty}^{+\infty} \frac{\lambda - 1 + \varepsilon}{(\lambda - 1 + \varepsilon)^2 + (\omega)^2} g(\omega) d\omega)\right]^2 + \left[\int_{-\infty}^{+\infty} \frac{\omega}{(\lambda - 1 + \varepsilon)^2 + (\omega)^2} g(\omega) d\omega)\right]^2$$

which can further be written as,

$$\frac{1}{\varepsilon^2} = \int_{-\infty}^{+\infty} \frac{1}{\lambda - 1 + \varepsilon + i\omega} g(\omega) d\omega \times \int_{-\infty}^{+\infty} \frac{1}{(\lambda - 1 + \varepsilon) - i(\omega)} g(\omega) d\omega$$

The eigenvalues of this equation then can be given by,

$$\lambda = 1 - \varepsilon + \Delta + \sqrt{\varepsilon^2 - \omega^2},$$

which yields the following condition for stability of the origin;

$$\text{if } \Delta > 1, \varepsilon > 1; \text{ and if } \Delta < 1,\ 1 < \varepsilon < \frac{(1-\Delta)^2 + \omega_o^2}{2(1-\Delta)} \tag{2.10}$$

As seen from Fig. 2.3(b), the numerical results are in agreement with the analytical results (Eq. 2.10). The time series of two nodes for a system($N = 1000$) with Lorentzian distribution ($\omega_o = 2.0$ and $\Delta = 0.33$) is shown in Fig. 2.1.

Bifurcation diagram: Fig. 2.3(a) is drawn using XPPAUTO software Ermentrout (2012) depicting two types of bifurcation. The first one is reverse Hopf bifurcation (HB) where a stable origin transforms into an unstable origin along with two stable limit cycles as the coupling strength decreases. The second one is pitchfork bifurcation (PB) where a stable origin becomes unstable and two more symmetric fixed points come into existence as coupling strength increases.

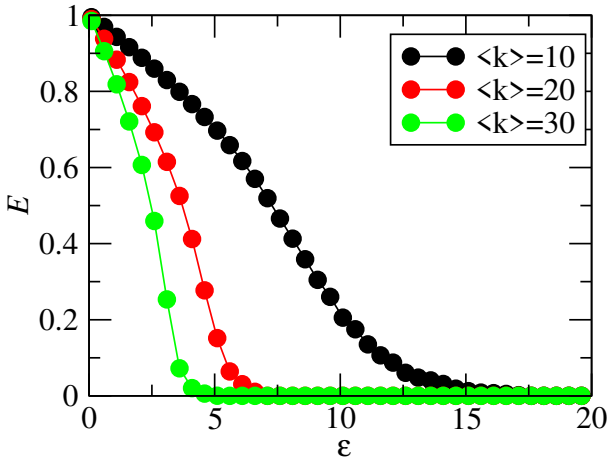

Figure 2.5: E vs ε, SL oscillators with dissimilar repulsive coupling on ER Random network with N=100 with Lorentzian frequency distribution with $\omega_o = 5.0$

2.4 Numerical results for various model networks

Next, we analyze the dynamical behaviors of coupled SL oscillators for this setup on various network architectures. We investigate how a particular network structure affects the onset of the oscillator death by considering four different network architectures apart from the globally coupled network, namely, the regular 1-d lattice, ER random, small-world, and scale-free networks.

Among these, the scale-free and 1-d lattice have the same lowest critical coupling strength at which AD occurs. While the small-world network has a slightly more critical coupling value as compared to the 1-d lattice, ER random network achieves AD at higher critical coupling strength (Fig. 2.4). The above observation implicates that the critical coupling strength increases when the regular 1-d lattice is distorted and changed to the ER random networks. Moreover, with an increase in the average degree of these, we observe a similar rise in the critical coupling network. Here in Fig.2.5 we have observed the dynamical behavior of non-identical SL oscillators on ER random networks with the various average degrees. It was found that the critical value of coupling strength decreases as we increase the average degree of the ER random network.

2.4.1 Oscillators without repulsive feedback coupling

An introduction of the diffusive coupling between a pair of connected nodes through both the x and y coordinates results in the following equation,

$$\dot{x}_k = P_k^x + \frac{\varepsilon}{N}\sum_{j=1}^{N} A_{jk}(x_j - x_k),\ \dot{y}_k = P_k^y + \frac{\varepsilon}{N}\sum_{j=1}^{N} A_{jk}(y_j - y_k) \tag{2.11}$$

Here A_{jk} is the adjacency matrix representing the underlying network structure. For an unweighted network, its elements take the value 1 when j^{th} and k^{th} nodes are connected, and 0 otherwise. Whereas, for a weighted network the elements of the adjacency matrix are represented by the interaction weights. Here, we consider the case of identical oscillators with all the nodes having the same frequency ω_o. Next, we can proceed to calculate the Jacobian matrix and then F and M matrices. The coupling matrix F and matrix M for this model will be the following. $M = \begin{pmatrix} \lambda - 1 + \varepsilon & -\omega_0 \\ \omega_0 & \lambda - 1 + \varepsilon \end{pmatrix}$ and $F = \begin{pmatrix} -\varepsilon/N & 0 \\ 0 & -\varepsilon/N \end{pmatrix}$ Next inserting them in Eq. 6, we get the solutions for the eigenvalues as,

$$\lambda_{1,2} = (1-\varepsilon) \pm i\omega$$

$$\lambda_{3,4} = 1 \pm i\omega$$

As we can see that one of these eigenvalues will always have a positive real part which can never be negative with the change in parameters, we can conclude that we can never obtain the amplitude death for this setup.

2.5 Seizure data networks

Postictal generalized EEG suppression (PGES) refers to the diffuse background attenuation ($< 10V$) in the postictal state. The phenomenon is often observed following bilateral tonic-

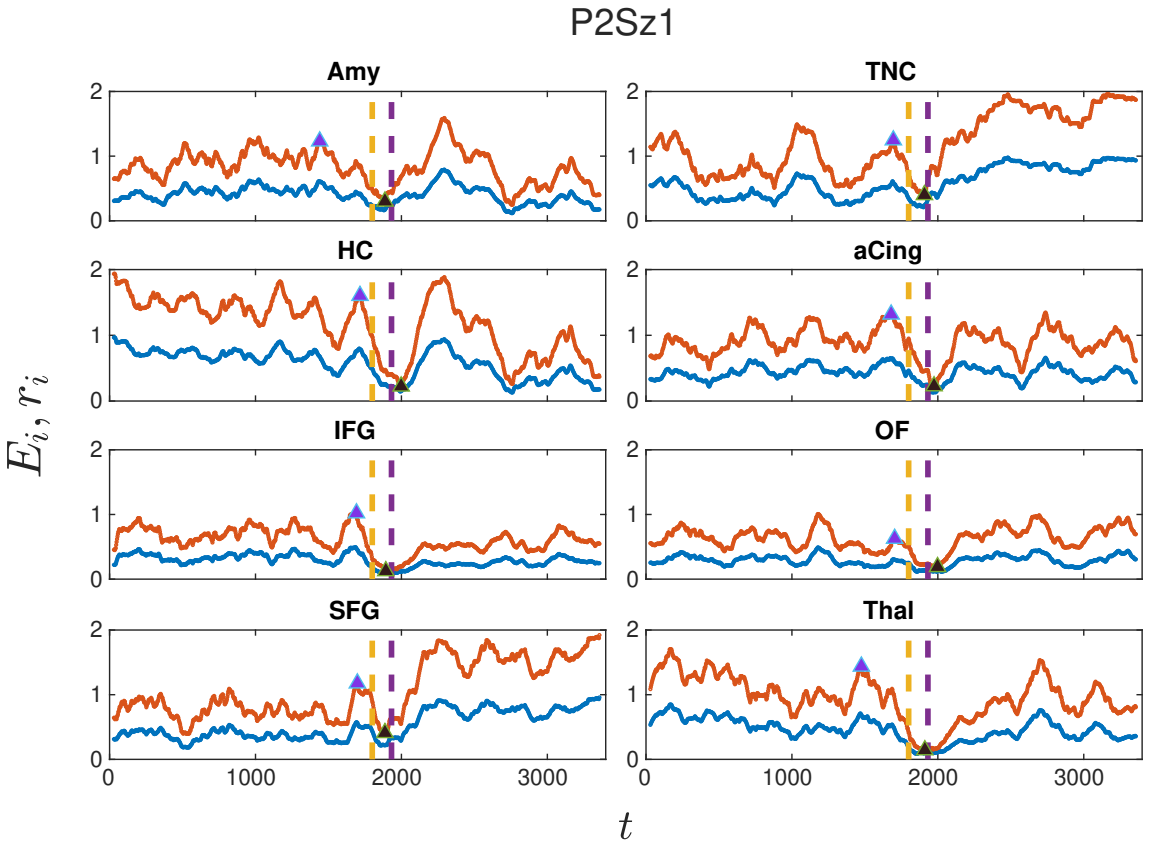

Figure 2.6: Δ band for P2Sz1: The red and blue lines represent E_i vs t and r_i vs t, respectively. The yellow and violet dashed lines correspond to start and end of the ictal region. Each subfigure represents the dynamics of a node.

clonic seizures (TCS), and has been associated with a sudden unexpected death in epilepsy Asadollahi et al. (2018); Lhatoo et al. (2010a). The mechanism and origin of occurrence of PGES are under intense investigations Seyal et al. (2012); Kanth et al. (2022); Aiba and Noebels (2015). Here we show similarities of the phenomenon observed by Eq. 2.2 with PGES in convulsive seizure. We do not claim that the Eq. Eq. 2.2 presents an accurate model to the brain activities, nevertheless, the quenching of oscillations manifested by the model bears a resemblance to PGES. Moreover, to bring the model a step closer to the Brain activities, we present result for the coupling architecture corresponding to the correlations matrices for the EEG multivariate time series data for seizure. This correlation matrix dataset consists of $8 \times 8 \times f \times t$ tensor where f and t are, respectively, the number of the frequency levels and time steps for which data is recorded. The whole frequency range is divided into five bands or levels. The bands are as follows- $\Delta : 2-4$, $\theta : 4-7$, $\alpha : 8-12$, $\beta : 12-30$, $\gamma : 30-40$. Hence, each

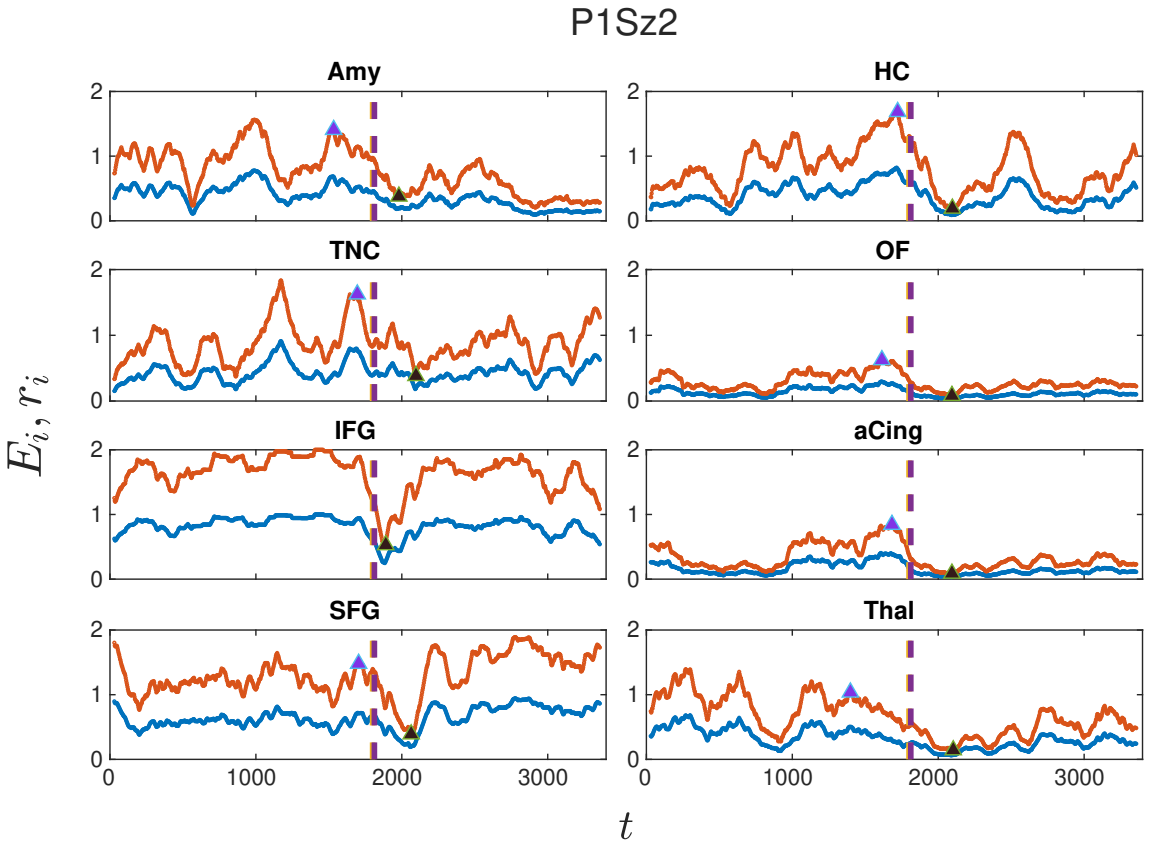

Figure 2.7: Δ band for P1Sz2: Red and blue lines represent E_i vs t and r_i vs t, respectively. Yellow and violet dashed lines correspond to the beginning and ending of the ictal region. Each subfigure represents dynamics of a node.

8×8 matrix represents an adjacency matrix at a particular time at a particular frequency level. Each of these adjacency matrices is constructed by calculating the correlation between the time series of the 8 channels at the corresponding frequency level for a particular time window. The detailed method for calculating gPDC matrices is given in next subsection.

2.5.1 Patient and surgical procedure

2 adult patients with suspected drug-resistant temporal lobe epilepsy (TLE) (mesial and temporal plus) underwent stereo electroencephalography (SEEG) for localization of seizure foci. The Institutional Review Board approved the study for recording local field potentials (LFP) from

the thalamus during SEEG exploration (IRB-170323005). Before the surgery, the patients provided written consent for thalamic electrode implantation and recording for research purposes. The ethics, consenting process, safety, and accuracy of our thalamic implantation have been published previously Chaitanya (2020). The thalamic implantation was unilateral and ipsilateral to the seizure foci and none of the patients had any thalamic bleed or related neurological complications. Overall, 4 focal to bilateral tonic-clonic seizures (2 seizures per patient) were analyzed.

2.5.2 Data acquisition

The optimal SEEG electrode implantation strategies were planned using Robotic assistance (ROSA device, Medtech, Syracuse, NY) to sample thalamic nuclei and preplanned temporal network regions of interest. The multi-electrodes (PMT® Corporation, Chanhassen, MN) have $12-16$ contacts per depth electrode, $2mm$ contact length, $0.8mm$ contact diameter, and $1.5mm$ inter-contact distance. Natus Quantum (Natus Medical Incorporated, Pleasanton, CA, sampling rate $2048Hz$, hardware filters were present in the acquisition procedure: $0.08Hz-1/3$ of sampling frequency hardware filtering, input noise $\leq 2V$ peak to peak, and $16-$bit precision) was used to record intracranial video-EEG. Signals were referenced to a common extracranial electrode placed posteriorly in the occiput near the hairline.

2.5.3 Electrode localization

Electrode localization was performed by co-registering Pre-implantation MRI and post-implantation CT axial images using Lead-DBS software Horn and Kühn (2015) (www.lead-dbs.org) and the electrode trajectories were mapped using iElectrodes software Blenkmann et al. (2017). Eight brain regions were uniformly selected constituting the thalamocortical network, which is composed of amygdala (Amy), hippocampus (HC), temporal neocortex (TNC), superior and inferior frontal gyrus (S/I FG), anterior cingulate (aCing), orbitofrontal (OF), and thalamus (Thal). Moreover, as a representative of this global phenomenon we have sampled neural activity within the cortical (frontal, cingulate, lateral temporal) and subcortical regions (amygdala, hippo and

thalamus). More importantly, these regions sampled are part of the limbic network that is involved in temporal lobe epilepsy and are commonly sampled for epilepsy surgery Rajmohan and Mohandas (2007) So these regions are functionally connected and are clinically relevant in epilepsy Bonilha et al. (2012)."

2.5.4 Data Preprocessing and MVAR model

For each of the four seizures, the continuous sEEG data is composed of 30-minute preictal, ictal, and 30-minute postictal periods. The data were divided into 30 seconds epochs each with 3 seconds overlaps. The data were detrended and filtered by an 8th order bandpass Butterworth filter with cutoff frequencies of$1-500$ Hz. A multivariate autoregressive (MVAR) model $X(t) = \sum_{\tau=1}^{p} A(\tau)X(t-\tau) + \varepsilon(t)$ of order $(p = 8)$ was fit to each sEEG epoch from 8 channels. The coefficients of the model, $A(\tau)$, were estimated using minimization of the residual noise $\varepsilon(n)$ and were estimated via the Vieira-Morf partial correlation method. If the model fits the data well, the noise (innovation) vector $\varepsilon(n) = [\varepsilon_1(n), ...\varepsilon_k(n)]^T$ follows a MV standard white noise process having zero mean and covariance matrix $\Sigma_e = \begin{pmatrix} \sigma_{11} & . & . & \sigma_{1K} \\ . & . & . & . \\ \sigma_{11} & . & . & \sigma_{1K} \end{pmatrix}$, assuming that each vector component is at least a weakly stationary time series. If we denote the $(K \times K)$ identity matrix as I_K, the MVAR model can be transformed to the frequency domain, as: $E(f) = B(f)y(f)$, where $E(F)$ is the Fourier transform of the residual noise vector and $B(f) = I_k - \sum_{\tau=1}^{p} A(\tau)e^{-j2\pi f\tau}$. Assuming that $\varepsilon(n)$is the input signal to the model and $y(n)$ the output signal from the model, $B(f)$ essentially results from the Fourier transform of the augmented matrix of the coefficients of the model (setting $A(0) = I_k$).

2.5.5 Directed Functional Connectivity Measure

Partial directed coherence (PDC) was introduced by Baccala and Sameshima in 2001 as a normalized estimate between the interval [0,1] and measures per frequency of the ratio of the outflow of the channel to channel i overall outflows from channel j Baccalá and Sameshima

(2001). PDC inherently distinguishes between direct and indirect interactions and can capture the directed and weighted (DW) Granger-connectivity structure scheme between each pair in the network. A generalized form of PDC (gPDC) was proposed by Baccala in 2007 which introduced a second inner normalization that makes it very robust with regards to inaccuracies and variability of measured data Baccala et al. (2007). is based on the Fourier transformed augmented coefficient matrix, $B_{ij}(f)$, and the diagonal elements of the covariance matrix, σ_{kk}, of the innovation process of the MVAR model, and is defined as:

$$gPDC_{j->i}(f) = \frac{|B_{ij}(f)|/\sigma_{ii}}{\sqrt{\sum_k |B_{kj}(f)|^2/\sigma_{kk}^2}}$$

gPDC is normalized between the interval [0,1], as well.

2.5.6 Dynamics on the functional network

We consider all the interactions having dissimilar repulsive feedback links. In other words, dynamics of the brain network have been modeled with the help of Eq. 2.2. The dynamical evolution of these differential equations are influenced by the adjacency matrices (A) which are calculated from EEG data. This is under the assumption that there exists a direct relationship between the anatomical connections and dynamical behavior reported in this section. We calculate the order parameters required to test for suppression of oscillation and study their evolution with time. We have reported results of two seizure in this section and two more seizure in the Appendix **??**.

Overall oscillation suppression: While, different regions for different patients reflect different behaviors, one typical pattern common in most of the nodes for all the patients is that the amplitude starts to decrease in the ictal region as compared to the preictal region. Ergo, there exists a considerable suppression of the oscillation in the majority of the nodes around the ictal and in the initial stages of the postictal region for all the patients' data we have investigated. The amplitude remains low for the initial points of the postictal region and then slowly recovers with time.

Name	P1Sz1	P1Sz2	P2Sz1	P2Sz2
Amy	1428,2208	1533,1971	1440,1887	1710,1848
HC	1659,2193	1722,2097	1716,1998	1710,1944
TNC	1638,1941	1695,2097	1695,1908	1545,1896
OF	1386,1950	1614,2094	1704,1998	1764,1944
IFG	1644,2145	1470,1890	1692,1893	1431,2028
aCing	1383,1950	1683,2094	1680,1974	1590,2031
SFG	1623,2145	1704,2064	1698,1887	1485,1908
Thal	1647,2145	1398,2103	1476,1911	1431,2028

Table 2.1: Onset and recovery time (in seconds) for the oscillation suppression across various patients for different nodes.

Temporal and spatial heterogeneity: The oscillation suppression phenomenon for most of the nodes is more prominent in two Seizure data considered here (P2Sz1 and P2Sz2).To illustrate the temporal heterogeneity more clearly, we create a table for the time points indicating the onset of the oscillation suppression and recovery of the amplitude, respectively. We obtain similar results for other frequency bands such as θ, α, β, and γ. The source of this phenomenon lies in the changes in the network structure.

Mechanism of the amplitude death: The uncoupled equation represents a limit cycle oscillator, to which the coupling acts as a decaying term resulting in the amplitude death at certain values of the frequency and the coupling strength. The impact of this coupling term as a whole also depends on the associated coupling matrices (underlying network architectures), and therefore there exists a change in the critical coupling strength for which death occurs with the network structure. Additionally, the average degree of the network also plays a decisive role in deciding the amount of suppression of oscillations on the network.

As pointed out earlier, these results are derived under the assumption that the structural connectome and the functional network exhibit a close resemblance. While the connectome provides the physical basis for functional connectivity (gPDC matrix), it is important to note that brain regions can exhibit functional connectivity even in the absence of direct structural connections. This phenomenon may arise due to indirect pathways or complex network dynamics Blanco

et al. (2024). In nonlinear dynamics, *remote synchronization* serves as a notable example of similar behavior, where nodes display correlated time series despite the lack of direct connections Gambuzza et al. (2013). However, despite these limitations, our model demonstrated promising signs of replicating the empirical behavior.

2.6 Conclusion

This article proposes a coupling setup that yields oscillation death in coupled Stuart-landau oscillators, and develops a theoretical framework to derive the necessary and sufficient conditions for attaining the oscillator death state for this setup with a fraction of nodes having repulsive feedback couplings. The analytical predictions are confirmed with the numerical experiments. Additionally, numerical results for the amplitude death on a few other model networks has been presented. Furthermore, we numerically analyzed the coupled dynamics model for the weighted correlations matrix constructed from the seizure data, and found that the phenomenon of amplitude suppression in the model resemble with the PGES. One of the immediate future extensions of this work is to derive analytical conditions for other states than AD, and to develop a generalized theoretical framework that can incorporate various forms of the couplings Jalan and Sarkar (2017), and adaptation rules Kachhvah and Jalan (2022); Jalan and Suman (2022). Further future directions are to have a more realistic model for the brain and to replicate these results in a larger cohort, particularly by including a postictal state that lacked PGES to understand the origin of PGES. Furthermore, the neural underpinning of such OD to AD transition or oscillation suppression could also be harnessed towards developing neuro-modulation therapy principled to perturbation of the coupling process to prevent or rescue OD/AD.

This page was intentionally left blank.

Chapter 3

Solitary death in coupled limit cycle oscillators with higher-order interactions

3.1 Introduction

In Chapter 2 we saw that suppression of oscillations in dynamical systems has been an area of persistent interest due to its occurrence in a wide range of real-world dynamical systems. Quenching of oscillations in large-scale dynamical systems made of interacting units arises primarily from the coupling between these units. In the last chapter we studied the effect of various types interaction in coupled SL system. Here we try to look beyond that.

It has increasingly been realized that real-world complex systems made of dynamical units may not only have pairwise interactions but also possess higher-order structures; examples include cliques in the human brain Sizemore et al. (2018), scientific collaborations Vasilyeva et al. (2021) etc. It is intriguing to explore the dynamics of higher-order interaction accounts and it has been explored in recent years. For example, studies on phase oscillators with higher-order interactions have revealed existence of an infinite number of multi-stable synchronized

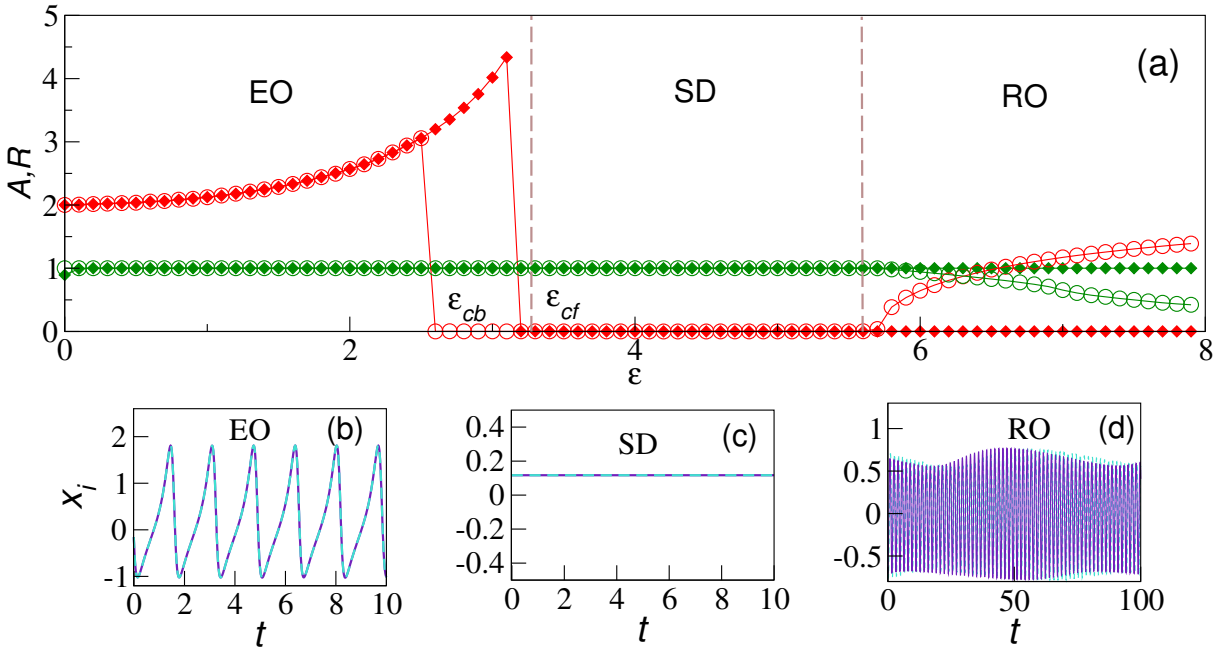

Figure 3.1: (a) A, R vs ε, (b)-(d) time-series of globally coupled identical SL oscillators (Eq. 3.1), (b) synchronized state with enhanced oscillation (EO) ($\varepsilon = 2.3$), (c) solitary death (SD) ($\varepsilon = 3.4$), (d) revival of oscillations (RO) state with toroid ($\varepsilon = 7.5$). Red diamond (circle) represents A in the forward (backward) direction, and green diamond (circle) is R in the forward (backward) direction. Other parameters are $N = 1000$, $\omega = 4.0$, $x_i(0), y_i(0) \in [0,1] \, \forall \, i$.

state Tanaka and Aoyagi (2011); Skardal and Arenas (2019). Later, in 2019, this existence of multistability has been confirmed Skardal and Arenas (2019) also showing the existence of backward synchronization with no forward synchronization. The Kuramoto oscillator model describes only phase of a system, however, many real-world complex systems are better described by a model consisting both amplitude and phase. SL oscillators is a limit cycle model which takes into account both the factors.

Recently, Carletti *et al.* investigated coupled SL oscillators with linear higher-order interactions on networks Carletti et al. (2020). Note that the form of higher-order interactions considered in Ref. Carletti et al. (2020) gets decomposed into pairwise interactions for globally coupled systems, i.e. in absence of a network structure. This chapter considers coupled SL oscillators with higher-order non-linear multiplicative coupling which can not be decomposed into pairwise interactions. We find synchronization, first-order transition to oscillator death and revival of the oscillations after the death state. A surge in the amplitude of the dynamical variable is accompanied by the synchronization. Importantly, the oscillator death observed here does

not get manifested in the pairwise coupled SL oscillators. Usually, the AD state arises when an unstable fixed point of the uncoupled system becomes stable due to the coupling, and the parity symmetry of the system is preserved with an introduction of the coupling, whereas OD state, which corresponds to the birth of more than one fixed points, arises as a consequence of parity symmetry-breaking of the uncoupled system due to coupling. This chapter reports a new state of a single pair of stable and saddle fixed points in SL oscillators upon introduction of the coupling which preserves the parity symmetry. In saddle-node bifurcation, a stable and a saddle point appear together where the saddle point has both stable and unstable manifolds. This single stable fixed point arises through the saddle-node bifurcation upon coupling through triadic interactions. The birth of these new fixed points does not change the stability properties of the already existing unstable fixed point of the system. We refer to such a single stable fixed point as solitary death (SD) state to distinguish it from other coupling-created death states which correspond to an existence of more than one stable fixed points. We perform the linear stability analysis to find the criteria for the occurrence of the SD state. Also, we analyze the basin of attraction of the bi-stable regions during synchronization, and the first-order transition to death states and draw bifurcation plots for the coupled system. Finally, we check the robustness of the occurrence of all the phenomena against change in the value of the intrinsic frequency, the introduction of pairwise interaction, and for non identical oscillators in the system.

3.2 Model

The dynamical equation for an uncoupled SL oscillator can be written as,

$$\dot{z}(t) = (a^2 - |z(t)|^2)z + i\omega z.$$

Here z is a complex variable depicting the dynamical state of an oscillator with ω being its intrinsic frequency. The oscillator has one unstable fixed point acting as a centre for a stable circular limit cycle of radius a. We propose a coupling scheme for incorporating higher-order interactions among dynamical units. Our prime consideration while proposing the scheme is that it should not be decomposed into pairwise terms. One of the simplest ways of satisfying this condition is to consider the product of the dynamical states of the interacting oscillators.

Moreover, we avoided the conjugate variable (z^*) in the coupling function since it already yields quenching of the oscillations for pairwise coupling Sathiyadevi et al. (2022). Hence, it will be difficult to assess if the particular types of oscillations quenching state reported in this chapter arises due to higher-order or conjugate couplings. However, the feedback coupling through z_k in pairwise interaction does not result in quenching. Further, when transformed to polar coordinates, Eq. 3.1 signifies periodic coupling between the phases of the interacting oscillator, just like the form of higher-order coupling used in lower dimensional counterpart (Kuramoto oscillator) Skardal and Arenas (2019) of SL oscillators. The coupled dynamical equation is given by,

$$\dot{z}_j(t) = (1-|z_j(t)|^2)z_j + i\omega z_j + \frac{\varepsilon}{N^2}\sum_{k=1}^{N}\sum_{l=1}^{N} z_k z_l. \tag{3.1}$$

Upon substituting $z_j = r_j e^{i\theta_j}$, we get,

$$\begin{aligned}
\dot{r}_j &= (1-r_j^2)r_j + \frac{\varepsilon}{N^2}\sum_{k,l=1}^{N} r_k r_l \cos(\theta_k+\theta_l-\theta_j), \\
\dot{\theta}_j &= \omega_j + \frac{\varepsilon}{N^2 r_j}\sum_{k,l=1}^{N} r_k r_l \sin(\theta_k+\theta_l-\theta_j),
\end{aligned}$$

where r and θ are the amplitude and phase of the oscillator, respectively. Upon substituting $z_j = x_j + iy_j$, the resulting equation is,

$$\begin{aligned}
\dot{x}_j &= P_j^x + \frac{\varepsilon}{N^2}\sum_{k,l=1}^{N}(x_k x_l - y_l y_k), \\
\dot{y}_j &= P_j^y + \frac{\varepsilon}{N^2}\sum_{k,l=1}^{N}(x_k y_l + x_l y_k),
\end{aligned}$$

where,

$$P_j^x = (1-x_j^2-y_j^2)x_j - w y_j,\ P_j^y = (1-x_j^2-y_j^2)y_j + w x_j.$$

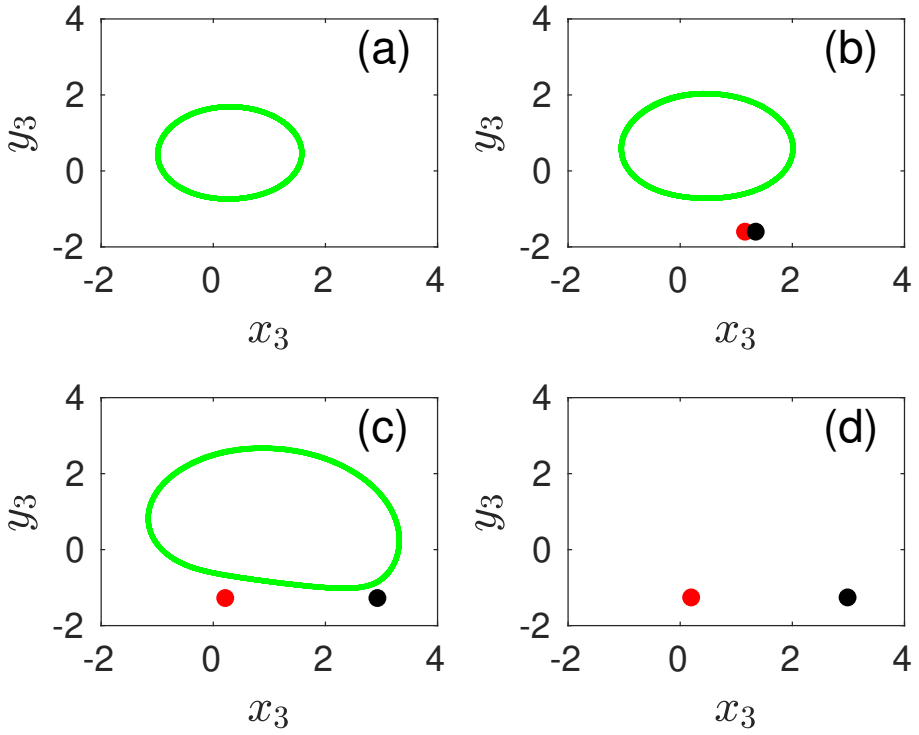

Figure 3.2: Coordinate space plot y_3 vs x_3 at various coupling strengths depicting disappearance of the stable limit cycle via homoclinic bifurcation for SL oscillators (Eq. 3.1). (a) $\varepsilon = 2.0$; existance of limit cycle, (b) $\varepsilon = 2.51$; birth of a pair of stable and saddle fixed points, (c) $\varepsilon = 3.14$; increase in the amplitude of limit cycle and approaching the saddle point, (d) $\varepsilon = 3.18$; disappearance of limit cycle through homoclinic bifurcation. Other parameters are $N = 3$ and $\omega = 4.0$. Red and black dots represent the stable fixed point and the saddle fixed point, respectively.

3.3 Different dynamical states

The population of SL oscillators coupled via higher-order interactions (Eq. 3.1) is affluent in dynamics and manifests several distinct dynamical states (Fig. 3.1(a)). Starting with the initial conditions drawn from a uniform random distribution between 0 and 1 ($x_i(0) \in [0,1]$, $y_i(0) \in [0,1] \, \forall \, i$), as we increase ε, the system gets synchronized immediately on a limit cycle at a very small value of ε. Upon a further increase in ε, the amplitude of the limit cycle keeps on increasing, and we call this state as enhancement of oscillation (EO) (Fig. 3.1(b)). In the forward direction, this state disappears yielding the oscillator death state named solitary death (SD) depicted by 0 value of A at a critical coupling strength ε_{cf} (Fig. 3.1(c)). In the backward

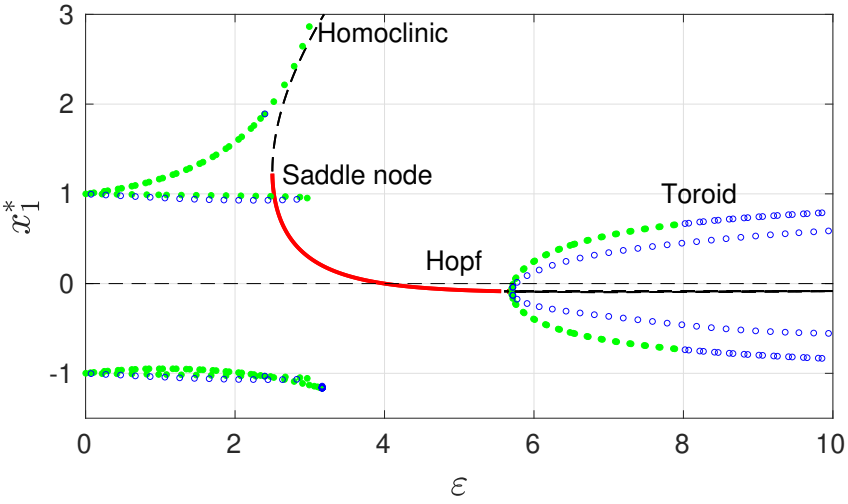

Figure 3.3: Bifurcation diagram plotted using XPPAUT Ermentrout (2012) for $\omega = 4.0$ and $N = 3$. The stable oscillatory state is depicted by filled green circle, while the unstable oscillatory state is depicted by empty blue circle. A stable steady state is represented by a red solid line while an unstable steady state is represented by the black dashed line.

direction, again starting with a homogeneous distribution for x_i, as ε is decreased adiabatically, initially, we encounter a state that oscillates (limit cycle) but not synchronized, and label it as revival of oscillations (RO) state (Fig. 3.1(d)). A further decrease in ε yields SD state which is finally encountered by a transition to EO state. However, this transition happens at a lesser critical coupling strength than ε_{cf} and is marked as ε_{cb}, thereby giving rise to hysteresis region. In the following, we describe all these states in detail.

3.3.1 Enhancement of oscillations (EO)

The first state we encounter while moving in the forward direction is EO. Here the oscillators are synchronized with the size of the limit cycle increasing with ε. This state disappears at the forward critical point ε_{cf} through a homoclinic bifurcation. For $\varepsilon < \varepsilon_{cb}$ we have the EO state without the existence of SD state (Fig. 3.2(a)), however, at ε_{bf} a pair of stable fixed and saddle fixed point are born (Fig. 3.2(b)). The saddle point and the stable limit cycle approach each other with increasing ε (Fig. 3.2(c)) and collide at ε_{cf}, beyond which the limit cycle disappears while the saddle point survives (Fig. 3.2(d)). From ε_{cb} to ε_{cf}, EO shares its basin with the SD state as both the states coexists. Additionally, the backward and forward transition points are

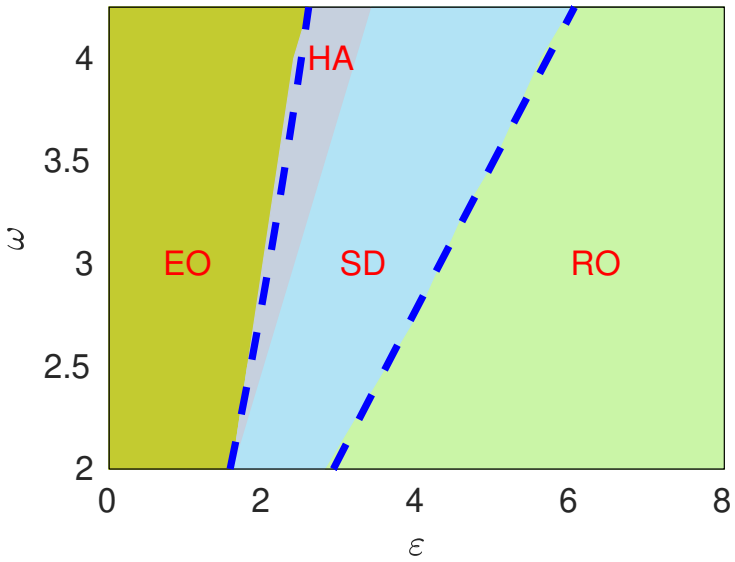

Figure 3.4: Phase diagram in the parameter space (ε, ω). Different states are EO (enhancement of oscillations), HA (hysteresis), SD (solitary death), RO (revival of oscillations). The blue dashed line is obtained from analytical calculations (Eq. 3.2). The other parameters are $x_i(0), y_i(0) \in [0,1]\ \forall\, i$ and $N = 1000$.

different. As illustrated by the bifurcation diagram (Fig. 3.3), the EO state is depicted in the form of a stable limit cycle whose amplitude increases with ε.

3.3.2 Solitary death (SD) state

Upon a further increase in ε, the system undergoes a first-order transition to the SD state (explosive death). Only one unstable fixed point exists before the critical ε (ε_{cb}). At ε_{cb}, due to the higher-order couplings in the system, a new pair of fixed points is born through the saddle-node (limit point) bifurcation, yielding one stable and one unstable branch (Fig. 3.3). The stable branch corresponds to the solitary death state and it loses stability when ε increases beyond a certain value. Before that until ε_{cf}, this stable fixed point coexists with two other stable limit cycles. This regime is depicted as the hysteresis loop whose width increases with an increase in the value of ω.

The numerical simulations indicate that all the oscillators settle to a common fixed point away from the origin (Fig. 3.1(c)). The position of the fixed points depends on w and k and is given by $x^{*1} = -\frac{-\omega-2\varepsilon y^*+\sqrt{(\omega+2\varepsilon y^*)^2+4y^*(y^*-y^{*3})}}{2y^*}$, $y^{*1} = -\frac{\omega}{\varepsilon}$ and, $x^{*2} = \frac{\omega+2\varepsilon y^*+\sqrt{(\omega+2\varepsilon y^*)^2+4y^*(y^*-y^{*3})}}{2y^*}$,

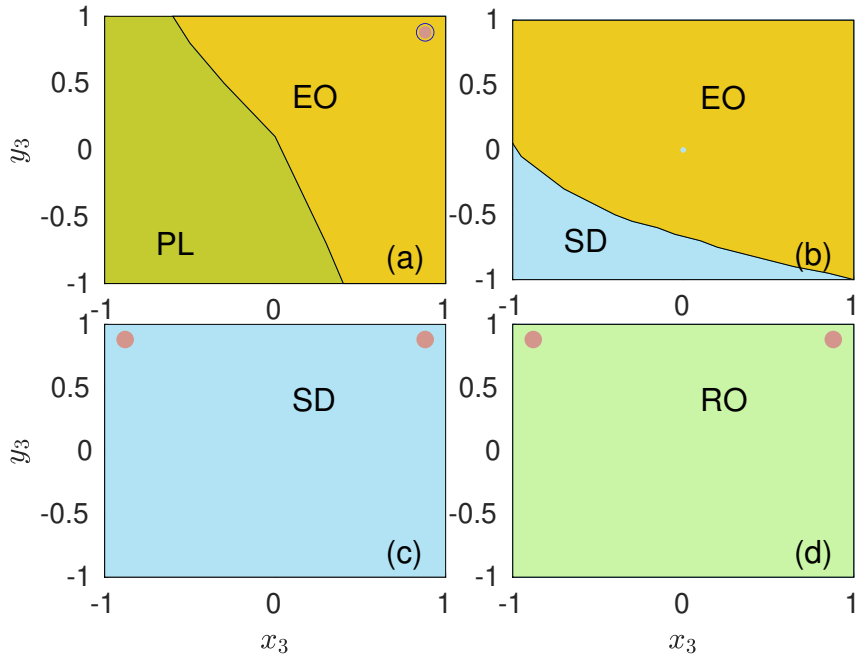

Figure 3.5: Basin of attraction for $N = 3$ and $\omega = 4.0$ in Eq. 3.1. (a) Synchronized state $\varepsilon = 1.0$, (b) hysteresis at $\varepsilon = 2.7$, (c) solitary death at $\varepsilon = 4.0$, (d) RO state at $\varepsilon = 7.0$. Different states are EO (enhancement of oscillations), PL (phase locked), SD (solitary death), RO (revival of oscillations).

$y^{*2} = -\frac{\omega}{\varepsilon}$ along with the preexisting fixed point $x^{*3} = 0$, $y^{*3} = 0$. Next, the characteristic equation for the Jacobian (J), which is a $2N \times 2N$ matrix, can be written in the form of,

$$|I\lambda - redJ| = \begin{vmatrix} M_1 + F_1 & . & . & F_1 \\ F_2 & M_2 + F_2 & . & . \\ F_i & . & M_i + F_i & . \\ F_N & . & . & M_N + F_N \end{vmatrix},$$

where, $M_1 = M_2 ... = M_N = M = \begin{pmatrix} \lambda - 1 + 3x^2 + y^2 & +\omega - 2xy \\ +\omega - 2xy & \lambda - 1 + x^2 + 3y^2 \end{pmatrix}$ and, $F_1 = F_2 ... = F_N = F = \frac{2\varepsilon}{N}\begin{pmatrix} x & y \\ y & x \end{pmatrix}$. The characteristic equation of these types of solutions is given by Dutta et al. (2023a),

$$\Pi_{i=1}^{N} |M| = 0 \text{ and } |I_2 + \sum_{i=1}^{N} \frac{adj(M)F}{|M|}| = 0.$$

The fixed point x^{*1} is unstable for all the values of ε and ω, confirming the simulation results. We focus on the following eigenvalues for x^{*2}, y^{*2} to get the stability condition for the SD state.

$$\lambda_{1,2} = 1 - \frac{2\omega^2}{\varepsilon^2} - \frac{\varepsilon^2\eta^2}{2\omega^2} \pm \sqrt{-\omega + \frac{\omega^4}{\varepsilon^4} + \frac{\eta^2}{2} + \frac{\varepsilon^4\eta^4}{16\omega^4}}, \tag{3.2}$$

$$\lambda_{3,4} = 1 - \frac{2\omega^2}{\varepsilon^2} - \frac{\varepsilon^2\eta}{\omega} - \frac{\varepsilon^2\eta^2}{2\omega^2} \pm \sqrt{-\omega + \frac{\omega^4}{\varepsilon^4} + \frac{\eta^2}{2} + \frac{\varepsilon^4\eta^4}{16\omega^4}}, \tag{3.3}$$

where, $\eta = -\omega + \sqrt{\omega^2 - \frac{4\omega}{\varepsilon}(-\frac{\omega}{\varepsilon} + \frac{\omega^3}{\varepsilon^3})}$. The real part of these eigenvalues (Eq. 3.2) must be negative for the fixed point to be stable, which provides us with the conditions $\varepsilon < \sqrt{\frac{1+4\omega^2}{2}}$, the upper bound for the stability of the fixed point. Similarly, the lower bound is derived by using the fact that the real part of Eq. 3.3 is less than zero and consequently $\varepsilon > \sqrt{-2 + 2\sqrt{1+\omega^2}}$. According to these stability conditions, when $\omega = 4.0$, we get $2.5 < \varepsilon < 5.7$, which are in complete agreement with the numerical results (Fig. 4.7). Upon increasing ω, while both the forward and backward critical coupling strengths corresponding to SD shift towards the right,

ε_{cf} shifts much larger than ε_{cb}, and consequently, the width of the hysteresis increases. Additionally, the stability region for SD state also increases with an increase in intrinsic frequency ω. Note that stability of SD state is independent of the system size. This helps us to compare the results of numerical simulation ($N = 1000$, Fig. 3.1) with the bifurcation plot ($N = 3$, Fig. 3.3) and draw inferences.

3.3.3 Revival of Oscillations (RO):

In the forward direction, once a death state is reached, it persists in an increase in ε. In the backward direction, starting from a set of random initial conditions, an oscillatory state is achieved with the decrease in ε. The fixed point corresponding to the SD state does lose its stability at critical ε; however, in the forward direction, we change ε adiabatically, the oscillators stay at the fixed point, and the unstable fixed point keeps getting manifested. Whereas, if we do not set the initial condition corresponding to a fixed point solution (as in the case of backward direction), an oscillatory state is achieved at critical ε. This state is, however, not simply elliptic in nature; rather resembles more like a torus. The bifurcation diagram points out that the stable fixed point loses its stability via Hopf bifurcation yielding an unstable fixed point and a stable limit cycle. This stable limit cycle again loses its stability via toroid bifurcation to become torus Appendix B. This torus rotates around an unstable limit cycle illustrated in the bifurcation diagram (Fig. 3.3).

3.4 Sensitivity to initial conditions

As depicted by Fig. 3.3, for lower ε values, the phase space is shared by two limit cycles. The first one remains as it is with an increase in ε and the oscillators are not synchronized but are phase locked (PL state). Whereas, in the other branch, the amplitude of the limit cycle (A) increases with ε and corresponds to all oscillators being synchronized (Fig. 3.1). The system chooses either of the limit cycles to settle based on the initial conditions as evident from the basin plot (Fig. 3.5)(a). Furthermore, in the hysteresis region, depending on the initial conditions, the system goes to the synchronized or the OD state. Since both the probable states in

this region satisfy the condition that $x_i = x_j$ and $y_i = y_j \; \forall \, i, j$ we have assumed $x_i = x_j = x_3$ and $y_i = y_j = y_3$ (Fig. 3.5)(b). The SD state after $\varepsilon = \varepsilon_{cf}$ does not share its basin with any other state (Fig. 3.5)(c). Similarly, in the RO state, if we start the simulations close to the unstable fixed point, the system remains in the SD state; else, it goes to the oscillatory state (Fig. 3.5)(d).

3.5 Introduction of pairwise couplings

Next, we add pairwise couplings along with the triadic couplings in the following manner;

$$\dot{z}_j(t) = (1 - |z_j(t)|^2) z_j + i\omega z_j + \frac{\varepsilon_p}{N} \sum_{k=1}^{N} z_k + \frac{\varepsilon}{N^2} \sum_{k=1}^{N} \sum_{l=1}^{N} z_k z_l, \tag{3.4}$$

where ε_p is the pairwise coupling strength. Fig. 3.6(a) indicates that even for small values of ε_p, synchronization is achieved. Moreover, with the introduction of pair-wise couplings, the hysteresis width decreases with an increase in ε_p.

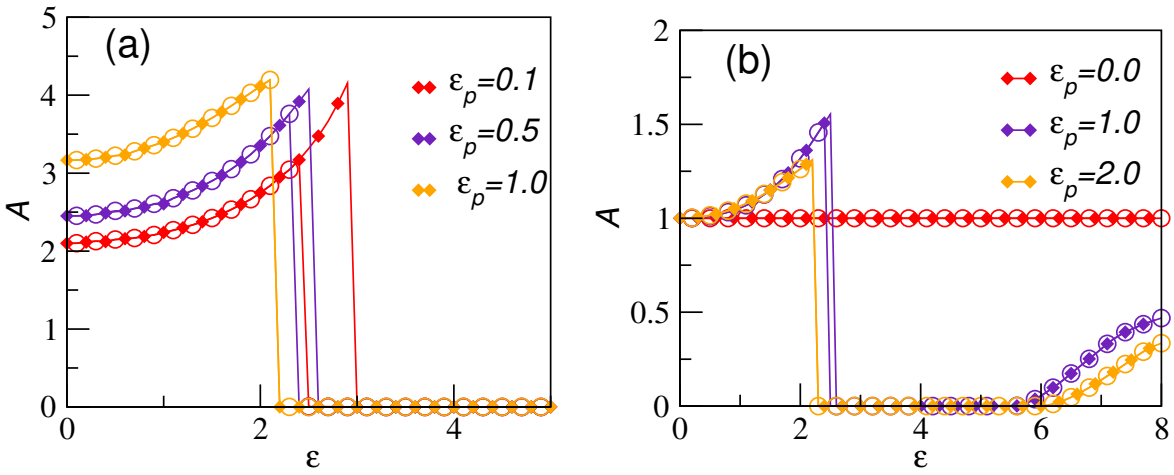

Figure 3.6: (a) A vs ε for globally coupled identical SL oscillators having pairwise interactions as well (Eq. 3.4) for $\varepsilon_p = 0.1$, $\varepsilon_p = 0.5$ and $\varepsilon_p = 1.0$; $\omega = 4.0$, $N = 1000$, (b) A vs ε for globally coupled non identical SL oscillators (Eq. 3.5) for $\varepsilon_p = 0.0$, $\varepsilon_p = 1.0$ and $\varepsilon_p = 2.0$; $\omega \in [4,5]$, $N = 1000$, diamond - A in the forward direction, circle - A in the backward

3.6 Non-identical coupled oscillators

To gauge the generality of the results presented here, we consider an ensemble of N non-identical SL oscillators coupled through higher-order as well as pairwise couplings. The dynamics of such a coupled system can be given by,

$$\dot{z}_j(t) = (1-|z_j(t)|^2)z_j + i\omega_j z_j + \frac{\varepsilon_p}{N}\sum_{k=1}^{N} z_k + \frac{\varepsilon}{N^2}\sum_{k=1}^{N}\sum_{l=1}^{N} z_k z_l, \tag{3.5}$$

where intrinsic frequencies of SL oscillators are uniformly distributed between $\omega_j \in [4,5]$. We find that in the absence of pairwise couplings, even for a small spread in the intrinsic frequencies, the system fails to stabilize to a death state (Fig. 3.6(b)). In other words, in the absence of pairwise couplings, the death state arising due to higher-order couplings becomes unstable and system stays on the same limit cycle even when ε increases. Moreover, at higher ε_p values, the both ε_{cb} and ε_{cf} decreases and so does the hysteresis width.

3.7 Conclusion

This chapter investigates globally coupled identical oscillators with higher-order interactions. We propose a scheme for incorporating higher-order interactions, which can not be decomposed into lower-order interactions and also contains a physical meaning in the polar coordinate counterpart. We report the emergence of a coupling-dependent SD state, a single stable quenched state arising from the higher-order interactions. This state might be relevant for real-world complex systems, where a single stabilization point is desired, and can be set using the coupling strength. Moreover, incorporation of higher-order interactions yields first order transition to death popularly known as explosive death. At lower coupling values the system is usually synchronized along with a surge in the amplitude and at very high coupling values we observe a RO state from SD state in the form of a torus. The surge in the amplitude just after the synchronization resembles the pre-ictal regime in which synchronization is accompanied by an

increase in brain activity, which is further followed by PGES (Post-ictal generalized epileptic seizure) corresponding to a considerable suppression of brain activity Grigorovsky et al. (2020); O'Sullivan-Greene et al. (2009). These states can be compared to the EO and SD states manifested by Eq. 3.1. Moreover, at the end of PGES, the brain might return to a normal state Fisher and Engel Jr (2010) which resembles the RO state discussed here. Further, we calculated the critical coupling strength for occurrence of SD state using the linear stability analysis which suggested system size independence. To the end we investigated dynamical evolution of the non-identical oscillators, and found that the non identical frequency distribution was responsible for destabilizing the SD state. However, an introduction of the pairwise coupling feedback helped in resorting the stability of SD.

This chapter only considers triadic couplings to model higher-order interactions. A straightforward extension of the present work is to incorporate other higher-order interactions, such as quadratic and other coupling forms. The effect of network structure on the dynamics of the system could also be an interesting avenue to have a more in-depth understanding of how higher-order interactions bring about emerging dynamical features beyond the scope of pairwise interactions.

This page was intentionally left blank.

Chapter 4

Dynamical phase transitions in post-ictal generalized EEG suppression

4.1 Introduction

Abnormal oscillatory activity in the brain and other physiological systems is frequently linked to pathological conditions arising from disruptions in underlying neurological control mechanisms Milton et al. (1989). To gain deeper insights into these phenomena, a range of mathematical models have been developed, offering a framework to investigate how variations in system parameters can lead to deviations from normal function. Such deviations often manifest as bifurcations or phase transitions, providing a mechanistic understanding of the onset and progression of disease states Ashwin et al. (2016).

Such pathological dynamics include the emergence of hypersynchronous oscillations during epileptic seizures Ren et al. (2021); Truccolo et al. (2014), or the loss of diurnal cortisol oscillations—typically modeled as a shift to a stable equilibrium—in patients with depression Hollister et al. (1980). Altered neuronal synchrony across temporal and spatial scales has been

implicated in several brain disorders, including Alzheimer's disease, Parkinson's disease, and schizophrenia Uhlhaas and Singer (2006); Aron and Yankner (2016). Furthermore, the spread of focal seizures has been modeled as a phase transition in computational frameworks of epilepsy Moosavi et al. (2022), reinforcing the relevance of bifurcation dynamics in pathological brain states.

One such condition is postictal generalized EEG suppression (PGES), a transient state that occurs in most patients following a generalized tonic-clonic seizure and is strongly associated with an increased risk of sudden unexpected death in epilepsy (SUDEP). PGES is characterized by a generalized suppression of EEG activity to amplitudes below $10\mu V$ (in scalp EEG recordings) within 30 seconds after the seizure, ignoring the presence of muscle movements, breathing, and electrode artifacts Lhatoo et al. (2010b); Surges et al. (2011); Rajakulendran and Nashef (2015); Xu et al. (2016). The duration of PGES has emerged as a potential clinical biomarker, as prolonged suppression is correlated with heightened SUDEP risk Marchi et al. (2019); Tao et al. (2013); Mier et al. (2020).

In neuroscience, various efforts have been made to model neurological conditions as dynamical systems. A common approach involves comparing functional connectivity patterns derived from empirical data with those generated by computational models Liu et al. (2023); Cabral et al. (2012). The time evolution of functional connectivity has been analyzed using methods such as the multiplication of temporal derivatives and the construction of functional connectivity dynamics matrices. Shine et al. (2015); Hutchison et al. (2013). Dynamical models have been particularly useful in exploring the resting state of the brain, where complex patterns of neural activity emerge in the absence of explicit stimuli Deco and Jirsa (2012); Cabral et al. (2017, 2012). It has been proposed that multistability in these models can account for the temporal fluctuations and spatial patterns observed in resting-state signals Deco and Jirsa (2012); Freyer et al. (2009). In particular, noise-induced switching between coexisting dynamical states has been shown to effectively reproduce the variability found in empirical recordings Cabral et al. (2017). Ghosh et al. further hypothesized that certain brain regions may operate near the critical point of a supercritical Hopf bifurcation, where fluctuations in coupling strength can drive transitions between a fixed point and a limit cycle, thereby capturing the dynamic range of brain activity observed in neurophysiological data Ghosh et al. (2008). Taking a different approach, Freyer *et al.* utilized a stochastic Hopf model to compare power distributions with

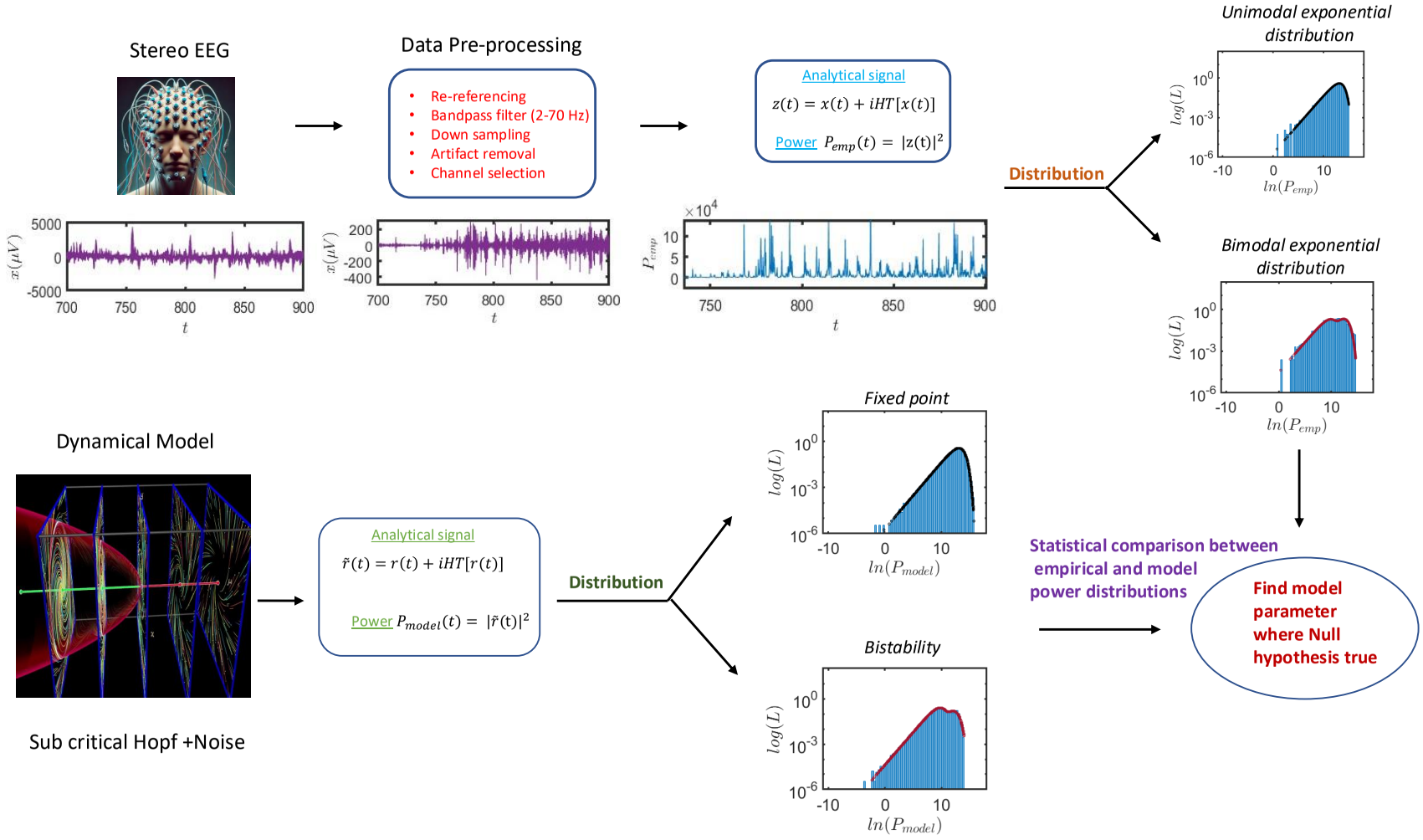

Figure 4.1: Flowchart illustrating the sequence of techniques used in this Chapter, starting from EEG data and the dynamical model to the determination of model parameters where the model and empirical data align.

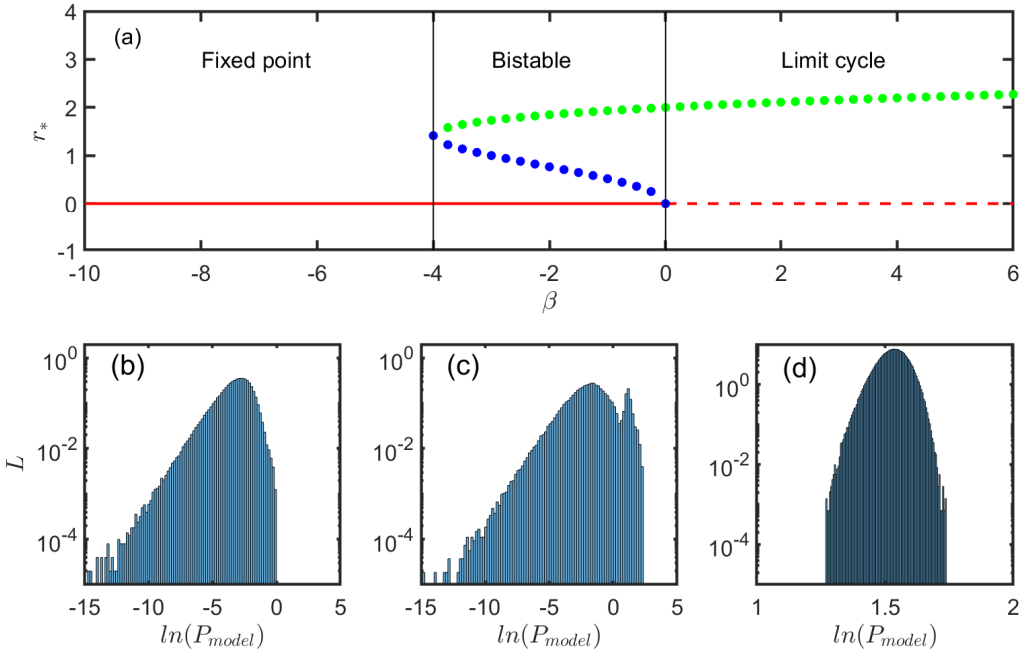

Figure 4.2: (a) The bifurcation plot r^* vs. β for Eq. 4.3 at $\lambda = 4$ and $\omega = 3.0$. The red solid and dashed line corresponds to stable fixed point, and unstable fixed point, respectively. Blue and green circles represent the unstable and stable limit cycle, respectively. (b), (c), (d) depict the power distribution at $\beta = -8$ (fixed point region), $\beta = -3.0$ (bistable region) and at $\beta = 1.0$ (limit cycle region).

their empirical counterparts, rather than focusing solely on functional connectivity Freyer et al. (2009, 2012), ultimately concluding that multi-stability could be a key factor in resting-state brain signals. In this study, we adopt a similar approach to investigate these dynamical properties further.

Although bifurcations at the onset and offset of epileptic seizures have been extensively studied Breakspear et al. (2006); Jirsa et al. (2014); Nazarimehr et al. (2018), to our knowledge, there exists no study on the phase transitions during the return to normal brain function. This chapter investigates the mechanisms behind postictal generalized PGES and the revival of normal brain function after PGES. We provide evidence that in the δ band, PGES primarily consists of a suppressed low-power state, which is followed by a bistable region consisting of switching between high- and low-power states before returning to the normal state. Suppression of oscillations is a well-known dynamical phenomenon that can be achieved by tuning the model parameters. The

normal form of the Hopf bifurcation model provides a prototypical framework for such systems, where oscillations cease by adjusting the model parameters for a single oscillator. Additionally, in coupled oscillators with various coupling forms, such as conjugate coupling Verma et al. (2018b); Dutta et al. (2023b), different mechanisms of oscillation suppression can arise, including amplitude death and oscillation death. This chapter reports that the transition from PGES to the normal state can be modeled using the normal form of a subcritical Hopf bifurcation, and it identifies the corresponding parameters of the differential equation that best replicate the empirical data in different states. We summarize the structure of this study in the form of a flow chart in Fig. 4.1.

4.2 Methods and techniques:

Dataset The data set is a stereo EEG time series of 5 subjects with one seizure each, and 1 subject with 2 seizures containing 276 channels with a sampling frequency of 2048 Hz. The data set was first referenced to a bipolar montage, following which it was filtered using the Finite impulse response (FIR) bandpass with a frequency range of $2-70$ Hz. Subsequently, the line noise was removed, and a notch filter was applied at 60 Hz. Afterwards, nine-time series were selected to represent the following areas - Anterior Hippocampus, Posterior hippocampus, Orbitofrontal, Cingulate, Frontal, Temporal, Insula, Amygdala, and Thalamus. The data was clipped to 10 minutes before and after a seizure. The duration of the ictal state differs from subject to subject. For an analytical EEG time series, the power at a particular time is defined as the square of the amplitude at that instant. The initial data set is a real-valued time series ($x(t)$). The Hilbert transform of $x(t)$ is given by

$$\bar{x(t)} = \frac{1}{\pi} PV \int_{-\infty}^{+\infty} \frac{x(\tau)}{t-\tau}.$$

PV represents the Cauchy principal value. The analytical signal is defined as $x(t) + i\bar{x(t)}$, and hence the amplitude of the signal at time t can be described as $\sqrt{x(t)^2 + \bar{x(t)}^2}$. Moreover, to get the power time series for a particular frequency band, the real-valued signal should be passed through a bandpass filter of the desired bandwidth (for example, $2-4$ Hz for δ band) before

calculating the analytical signal. Another way to get a similar outcome is to use the Morley wavelet transform Cohen (2014). The ethics, consenting process, safety, and accuracy of our thalamic implantation have been published previously Chaitanya (2020).

Exponential distribution: The central limit theorem states that the average of a large number of identical and independent random events tends to follow a Gaussian distribution. This theorem holds even when the random variables are not Gaussian. Applying a similar principle, one could argue that EEG signals may exhibit Gaussian characteristics Feller (1991). Each electrode in a scalp EEG captures millions of neurons firing independently in a temporally uncorrelated manner, not necessarily following a Gaussian distribution. However, the central limit theorem suggests that the combined effect measured at an electrode should approximate a Gaussian distribution. Any deviation from normality would indicate a violation of the basic assumptions of the theorem. Based on this, it was proposed that EEG signals may generally be Gaussian processes Gonen and Tcheslavski (2012); Lion and Winter (1953); Saunders (1963). However, later studies suggested that these results may depend on the length of the signal segment considered for the distribution McEwen and Anderson (1975). Longer signal segments were concluded to reduce the likelihood of obtaining a normal distribution. In addition to segmentation, other factors, such as sampling frequency and patient states, also affect normality Gonen and Tcheslavski (2012). A comparison between the amplitude distributions of task-dependent states and the resting state revealed that the former were less likely to follow a Gaussian distribution.

To prove the hypothesis, let us assume that the real-valued signal is a random variable X, and its Hilbert transform is another random variable Y. Both of these have Gaussian fluctuations, and their marginal distribution can be represented by a Gaussian distribution with zero mean and equal variance (σ^2) by $f_X(x) = \frac{1}{\sigma\sqrt{2\pi}} exp(\frac{-x^2}{2\sigma^2})$ and $f_Y(y) = \frac{1}{\sigma\sqrt{2\pi}} exp(\frac{-y^2}{2\sigma^2})$, respectively. Next, since X and Y are orthogonal to each other (as Y is Hilbert transform of X), the covariance matrix is given by, $\begin{pmatrix} \sigma^2 & 0 \\ 0 & \sigma^2. \end{pmatrix}$ Therefore, the joint probability distribution is defined as $f_{X,Y}(x,y) = \frac{1}{\sigma\sqrt{2\pi}} exp(\frac{-(x^2+y^2)}{2\sigma^2})$. Since the amplitude is defined as $R = \sqrt{X^2+Y^2}$ and the power as $P = R^2$, we perform a variable transformation of $P = X^2 + Y^2$ in the joint probability distribution to obtain the distribution of the power. The general equation for the transformation of variables in a probability distribution function is given by $P_Y(y) = |J| P_X(x)$ and we obtain $P_X(x) = \eta\, exp(-\eta x)$, known as the exponential distribution, η being the shape param-

eter. Henceforth, it can be stated that when the correlation among individual firing of neurons is low enough, the power distribution of an electrode is exponential. Any deviation from this distribution might suggest the presence of a correlation between the firing of neurons. Scaling the variable x as $y = ln(x)$, the scaled distribution

$$P_Y(y) = \left|\frac{dx}{dy}\right| \; P_Y(y) \; = \eta \; exp(y - exp(\eta \, y)). \tag{4.1}$$

A deviation from exponential statistics indicates the presence of temporal correlation. Moreover, in some cases, there exists a switching between the two states which can result in bimodal exponential statistics given by,

$$P_{XX}(x) = (1-\delta)\,\eta_1 \, exp(-\eta_1 x) + \delta \, \eta_2 \, exp(-\eta_2 x). \tag{4.2}$$

We expect the power distribution to follow an exponential distribution due to its stochastic nature. We find the parameters for the best fit (both unimodal (Eq. 4.1) and bimodal (Eq. 4.2)) of the empirical power distributions at various time windows using maximum likelihood estimation, and use the Bayesian information criterion (BIC) to compare the unimodal and the bimodal exponential distributions. BIC incorporates a penalty term proportional to the number of parameters used while fitting, and is defined as $BIC = -2 \times ln(L) - ln(n) \times number\,of\;parameters$. where L is the likelihood and n is the number of bins used for the distribution. The penalty term is the deciding factor in cases where both models fit the data equally. The lower the BIC value, the better is the fit. We calculate ΔBIC which is defined as $BIC(unimodal) - BIC(bimodal)$. Therefore, a negative BIC value infers a better unimodal fit and the vice versa.

Model: The objective here is to identify a suitable dynamical model to explain the bifurcations or phase transitions that occur in the postictal region of a tonic-clonic seizure. Two major models exhibit a bistable region shared between a limit cycle and a fixed point within a region of their parameter space; saddle-homoclinic bifurcation and subcritical Hopf bifurcation. In saddle-homoclinic bifurcation, a pair of saddle points emerges in the phase space where a limit cycle already exists. As the bifurcation parameter increases, the bistable region in phase space disappears due to the collision of a stable fixed point with a stable limit cycle. In subcritical

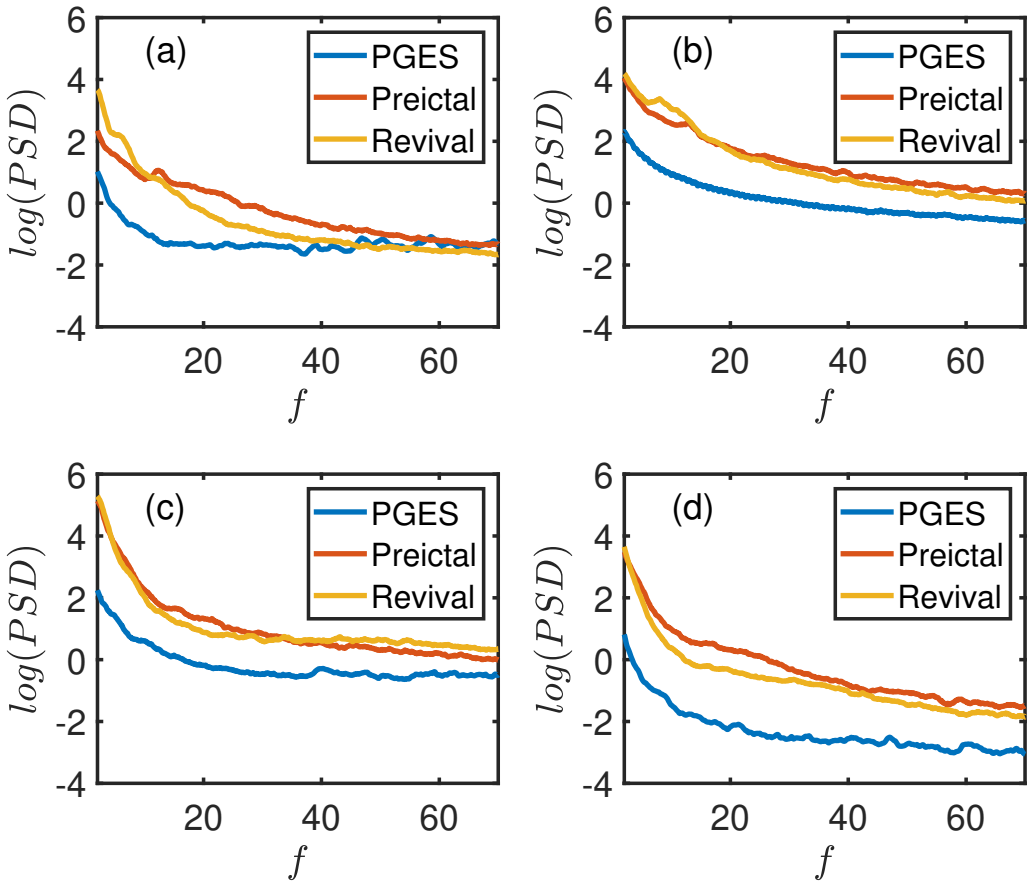

Figure 4.3: $log(PSD)$ vs f : Power spectrum for (a) Subject 1, (b) Subject 2, (c) Subject 3, and (d) Subject 4. The blue, red and yellow lines represent the PGES, preictal region and revival state, respectively.

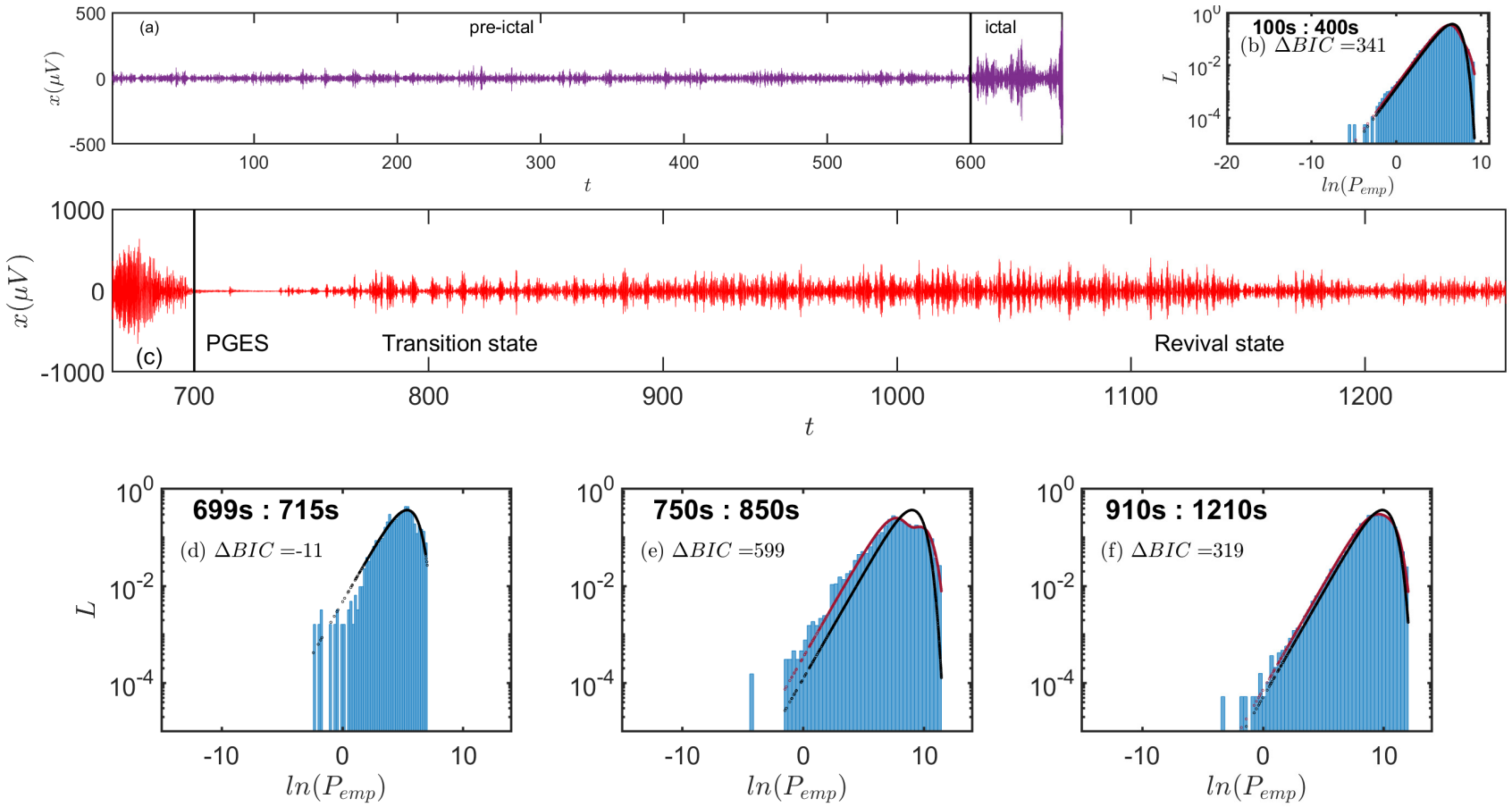

Figure 4.4: Real-valued EEG time series (x vs. t) and corresponding power distributions over various time intervals for subject 1 (Frontal region) in the δ band. (a) Time series for the preictal and ictal stages, separated by a solid black line; (b) Power distribution for the preictal region from 100s to 400s; (c) Time series for the postictal stage; (d) Power distribution for the PGES (suppressed state) in the time interval from 699s to 715s; (e) Power distribution for the transition state between 750s and 850s; (f) Power distribution for the revival state from 910s to 1210s. The solid black and red lines corresponds to the unimodal and bimodal exponential fit, respectively.

Hopf bifurcation, a stable fixed point bifurcates into an unstable fixed point and an unstable limit cycle. This unstable limit cycle later changes its stability, leading to a hysteresis effect (Fig. 4.2). However, in saddle-homoclinic bifurcation, the fixed point is typically parameter dependent, which is analogous to a changing baseline in EEG data Jirsa et al. (2014). Since the system considered here does not exhibit any significant baseline shift, we proceed with the "subcritical Hopf model", described by the following differential equation,

$$\dot{r} = \lambda r^3 + \beta r - r^5\,, \;\; \dot{\theta} = \omega. \tag{4.3}$$

This system of differential equations can be written in the cartesian coordinates as,

$$\dot{x} = (\lambda r^2 + \beta - r^4)x - \omega y\,, \;\; \dot{y} = (\lambda r^2 + \beta - r^4)y + \omega x$$

Here, ω is the intrinsic frequency, and β and λ are model parameters. The fixed points of these equations are given by $r^*_{\pm} = \sqrt{\frac{\lambda \pm \sqrt{\lambda^2+4\beta}}{2}}$, where r^*_+ is the stable branch and r^*_- is the unstable branch. The parameter λ controls the forward critical point of the limit cycle, and the fixed point always loses its stability at $\beta = 0$. Therefore, the parameter λ actually controls the width of the hysteresis. The parameter β is the bifurcation parameter required to obtain sub critical Hopf bifurcation. We tune these parameters to switch between the various states of our interest. However, in this model, there is a bistable state which is dependent on the initial conditions. Hence, to obtain the switching between the states we add additive and multiplicative Gaussian white noise to the system (Eq. 4.3) Freyer et al. (2012).

$$\dot{r} = \lambda r^3 + \beta r - r^5 + D_{add}\xi(t) + D_{mult} r\zeta(t)\,, \tag{4.4}$$

Here, $\xi(t)$ and $\zeta(t)$ represent Gaussian white noise with zero mean and unit variance, respectively, and D_{mult} and D_{add} correspond to the additive and multiplicative noise strengths, respectively. We calculate the amplitude as $A(t) = \sqrt{x(t)^2 + y(t)^2}$ and the power at time t as $P_{model}(t) = A(t)^2$. We expect the distribution of globally stable states to have a unimodal exponential distribution, and bistable state to have bimodal exponential distribution at appropriate values of η. The dynamics of this model can be understood through the bifurcation plot (Fig. 4.2). For, $\lambda = 4$ and $\omega = 3$ sub-critical Hopf bifurcation takes place at $\beta = 0$. For $\beta > 0$

we have a globally stable limit cycle with its amplitude scaling as $\sqrt{\beta}$. Moreover, we encounter a stable fixed point for $\beta < -4.0$ which again is globally stable. However, for $-4 < \beta < 0$ there is a bistable region where the basin of attraction is shared by the stable fixed point and the stable limit cycle.

The range of $x(t)$ varies from one patient to the other, and the same is true for the various channels in each patient. However, in our model, the range depends on the applied noise strengths D_{add} and D_{mult}. Numerical simulations are only possible for a certain noise strength before the solution diverges. We transform Eq. 4.4 using a scale factor to counteract this. This scaling preserves the bifurcation and other dynamical properties of the system. Substituting $r \to r/s$ we get,

$$\dot{r} = (\lambda \frac{r^2}{s^2} + \beta - \frac{r^4}{s^4})r + sD_{add}\xi(t) + D_{mult}r\zeta(t)\,, \tag{4.5}$$

where s is the scale factor. Eq. 4.5 was simulated using the Heun's method with step size $dt = 0.001$. All simulations were performed for 10^6 steps, and the initial 5×10^5 steps were discarded as transient.

Determining model parameter values: Here, our objective is to find the model parameters of Eq. 4.5 for which it will produce a power distribution statistically similar to the empirical power distribution. We perform non-parametric two-sample statistical tests like the Mann-Whitney test, mean-based permutation test, and Kolmogorov-Smirnov test to assess the fact that the differences between the two samples are not statistically significant.

Mann-Whittney test: The two-sample Mann-Whitney test evaluates whether there exists a statistically significant difference in the distribution of two independent groups. The test is based on ranking all the observations from both groups together and then comparing the ranks between the two groups. By calculating the sum of the ranks for each group, the Mann-Whitney test assesses whether one group tends to have higher or lower ranks than the other. The resulting U-statistic, which reflects the difference between the rank sums, is then used to determine the significance of the observed difference. A p-value is obtained by comparing the observed U-statistic and its distribution under the null hypothesis.

Mean based permutation test: The null hypothesis states that the difference of the mean be-

tween the two distributions is not statistically significant. The data from both groups are combined into a single pooled dataset, which is then randomly shuffled to create a permuted dataset. After each shuffle, the observations are reassigned to the two groups, and the difference in their means is calculated. This process is repeated 10,000 times. The p-value is determined by calculating the proportion of permuted mean differences that are as extreme or more extreme than the observed mean difference of the original data.

Kolmogorov-Smirnov test: The two sample Kolmogorov-Smirnov (KS) test is a non parametric statistical test used to determine whether two independent samples are drawn from the same continuous distribution. It compares the empirical cumulative distribution functions of the two samples and calculates the maximum absolute difference between them which determines the p-value. This approach is particularly useful for identifying distributional shifts or differences in the shape of the distributions.

For all tests, a significance level of 0.05 was used to determine whether the null hypothesis is accepted. The three tests used in this study are based on different criteria for comparing distributions. The Mann-Whitney test focuses on the median, the mean-based permutation test on the mean, and the KS test compares the cumulative distributions. This diverse statistical approach allows us to assess the similarity of distributions from multiple perspectives, thereby, enhancing the validity of our hypothesis. However, due to the stochastic nature of Eq. 4.5, a particular set of parameters can yield different power distributions. To account for this variability, we simulate 100 power distributions for each set of parameters and report the fraction of simulations where the null hypothesis was accepted. The determination of the optimal set of parameters was achieved through manual searching of the parameter space grid. Manual searching was done due to the high sensitivity of parameters to statistical tests.

4.3 Results

Generally, detection of PGES from EEG data analysis is an intensive and manual process Mier et al. (2020). However, identification of PGES can also be done by analyzing the time-series data and the power spectrum Marchi et al. (2019); Tao et al. (2013); Bateman et al. (2019). In δ and θ frequency bands, the power spectral density(*PSD*) is much lower than the preictal

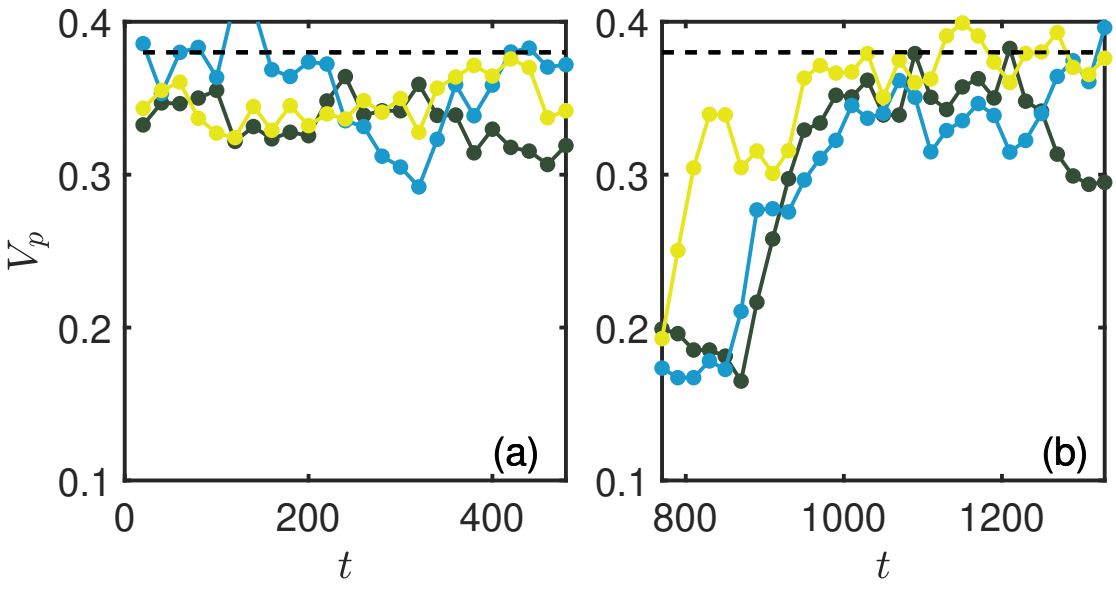

Figure 4.5: V_p vs t (Subject 1). (a) The peak value of the preictal power distribution remains constant over time, indicating the absence of a phase transition in this region. (b) The peak value of the postictal power distribution is slightly lower than $\frac{1}{e}$, suggesting a bimodal distribution. Blue, black and yellow circle corresponds to Orbitofrontal, Posterior hippocampus and Thalamus region, respectively.

counterpart. The subjects reported in Fig. 4.3 illustrates that the difference in the *PSD* for lower frequency bands (δ, θ) is considerably higher than the high frequency bands (α, β, γ) (Fig. 4.3). This indicates reduced brain activity immediately after a seizure compared to the preictal state. According to the definition of PGES, the absence of activity below $10\mu V$ for at least 1 second within 30 seconds of seizure can be classified as PGES. Therefore, combining these observations can serve as a reliable marker for identifying PGES.

Upon analyzing the empirical power (P_{emp}) distribution in the preictal region, we observe a bimodal exponential distribution in all the subjects (Fig. 4.4(a,b)). We find positive ΔBIC values for the subjects with bimodal distributions (Appendix III). Analysis of δ and θ bands reveals three stages of the postictal state: PGES, the transition state and the revival state. In the first stage, the EEG signal is wholly attenuated immediately after the seizure. This period is referred to as the PGES (Fig. 4.4(c,d)), which lasts approximately 15 to 20 seconds in our subjects. During PGES, we report an unimodal exponential distribution with negative values of ΔBIC in all subjects with the average ΔBIC around -10.74. The resurgence of the background activity marks the end of PGES, typically intermittent slow activity. This phase in the time series is characterized by a mixture of signal bursts and suppression (Fig. 4.4(c)). We refer to this phase as the transition region, representing an intermediate state between PGES and normal brain function. In this region, intervals of suppressed signals appear as a low-power mode. At the same time, sudden bursts correspond to a high-power mode in the power distribution of the transition region (Fig. 4.4(e)). This pattern suggests the presence of two distinct states, with the system switching between them. The ΔBIC values in this state are positive and consistently higher for all subjects compared to other time-series intervals (preictal and revival), indicating stronger bimodality. The $\langle \Delta BIC \rangle$ over all subjects in transition state is 662, which is much higher than revival ($\langle \Delta BIC \rangle = 308$) and preictal ($\langle \Delta BIC \rangle = 203$) states. This further supports the idea of two coexisting states with transitions between them. As the series progresses, these fluctuations become more frequent, resembling the preictal state. Finally, the time series transitions into a state similar to the preictal phase, which we term the revival state (Fig. 4.4(c,f)). The similarity between the preictal and revival states is evident from their ΔBIC values, indicating that the brain has returned to normal function. Moreover, the power spectral density (Fig. 4.3) of preictal and revival states are similar unlike the PGES, further asserting the similarity between these two states.

To understand the transition in the postictal state, we analyze the temporal behaviour of the peak value V_p (highest frequency) in the power distribution. The normalized unimodal exponential distribution has a consistent V_p of $1/e$ at $P = \frac{1}{\eta}$, regardless of the distribution's shape parameter (Eq. 4.1). However, in the case of a normalized bimodal exponential distribution, V_p depends on the shape and proportionality parameters and is always equal to or less than $1/e$, the maximum peak value (Eq. 4.2). A more significant deviation from this maximum peak value indicates increased bimodality in the empirical distribution. Fig. 4.5(a) shows that V_p for the preictal power distribution remains constant with time, indicating no phase transition in this region. Furthermore, for most subjects, V_p is slightly lower than the maximum, suggesting a mild degree of bimodality.

Fig. 4.4(d) further illustrates that in the suppressed region, which is unimodal, the peak value V_p remains at $1/e = 0.37$. In Fig. 4.5(b), we start from the transition state and continue up to the revival state. Here, we observe a sudden drop in V_p (transition state), followed by a gradual increase over time in the postictal region, as it progresses toward the revival state (Fig. 4.5(b)). This confirms the earlier observation of a transition from a state with higher bimodality (more positive ΔBIC values and lower V_p) to a state with lower bimodality following the suppressed state. Interestingly, Fig. 4.5 also shows that all channels exhibit varying degrees of bimodality and different durations of the transition state. In the case of Subject 1, we observe that the Frontal region exhibits a more prominent transition state.

Next, we demonstrate that the dynamical model accurately simulates the four stages: preictal state, postictal suppression state, transition state, and revival state (Fig. 4.6). Stages exhibiting bimodality fall within the bistable region of the dynamical system, while those showing an unimodal state likely correspond to the fixed-point region of the system. Our analysis shows that the dynamical model best mimics the preictal region when the parameters are on the verge of the bistable region and the fixed point, with a tendency toward the bistable region for all subjects Fig. 4.7(a-f). Furthermore, Fig. 4.6 reports the parameter values of the fitted exponential distribution (unimodal or bimodal) for both the empirical and model generated power distributions, denoted as $\hat{p}_{emp}$ and $\hat{p}_{model}$, respectively. For an unimodal distribution, the parameters are given by, $\hat{p}_{emp(model)} = \frac{1}{\eta}$. For a bimodal distribution, they are defined as: $\hat{p}_{emp(model)} = \left[\frac{1}{\eta_1}, \frac{1}{\eta_2}, \delta\right]$,where η, η_1, η_2, and δ have the same definitions as in Eqs. 4.1 and 4.2. From the Fig. 4.6, it is evident that the parameter values of the empirical data closely match those of the model

generated data for each state.

The PGES state is characterized by parameters in the fixed-point region for all subjects. The scale factor (s), which is one of the factors controlling η, is lower in this state compared to the preictal and revival counterparts. A lower scale factor indicates a reduced mean in the unimodal distribution, which suggests a suppression of signal fluctuations. This highlights an important observation: PGES is associated with reduced variability in brain activity. Additionally, during the transition phase, the parameter set for all subjects falls within the bistable region Fig. 4.7. The value of (β) depends on the position and proportion of the two modes in the bimodal distribution. A higher proportion of the high-power mode results in a (β) value deeper within the bistable region, further away from the boundary between the fixed-point and bistable regions in phase space. Finally, the parameters in the revival region closely resemble those of the preictal state. The transition from the suppressed state to the transition state can be interpreted as a shift from a fixed point to a bistable state in the model. However, since multiple parameters must be adjusted to progress from PGES to the transition state and the revival state, we refrain from classifying this as a strict bifurcation and instead call it a phase transition.

As mentioned earlier, we performed three statistical tests, namely, the Mann-Whitney test, the mean-based permutation test, and the Kolmogorov-Smirnov test to assess whether the null hypothesis (that the empirical and simulated power distributions come from the same distribution) can be rejected. While, we successfully identified model parameters where the null hypothesis was supported by all the three tests for some of the PGES and transition states, the Kolmogorov-Smirnov test often failed for highly bimodal distributions like the transition state. This issue primarily stems from the nature of the test, which compares the cumulative distributions of the samples, making it sensitive to small fluctuations that can lead to the failure of the test (Appendix III).

PGES is a scalp EEG phenomenon. A similar phenomenon, called intercranial postictal attenuation (IPA), has been observed in intracranial EEG exhibiting similar EEG signal suppression following a seizure, much like PGES. The primary difference between them is the γ wave activity, which is seen in IPA while being absent in PGES. Additionally, IPA has been reported to show a mixture of high-amplitude and low-amplitude segments in the time series, resembling the patterns observed in our system Marchi et al. (2019); Bateman et al. (2019). Although it is unknown whether PGES and IPA are manifestations of the same phenomenon, we point out

another similarity (apart from those reported earlier Bateman et al. (2019)) found between the two phenomena i.e. existence of the bistable transition state.

4.4 Conclusion:

Postictal dynamics vary across brain regions and individuals but typically begin with a suppressed phase marked by significant signal attenuation. This is followed by a transitional phase where bursts of high-amplitude activity intermittently interrupt the suppressed state, eventually leading to recovery characterized by a return to preictal-like activity. In this study, we analyzed the power distribution across EEG channels and found that the suppressed state exhibits a unimodal distribution, while the transitional phase displays pronounced bimodality. To capture this behavior, we employed the subcritical Hopf normal form, identifying parameter regimes that reproduce these empirical features. While the complexity of parameter interactions prevents us from definitively attributing the observed transitions to a classical subcritical Hopf bifurcation, our results support a transition from a fixed-point regime to a bistable state as a plausible underlying mechanism of EEG recovery during PGES.

A natural extension of this work involves incorporating coupling into the current model to better replicate EEG dynamics across different pathological states. Exploring the influence of various coupling schemes may yield insights into the mechanisms governing inter-regional coordination. Furthermore, integrating time-varying functional connectivity into dynamical modeling could enhance the accuracy and interpretability of models describing neurobiological phenomena.

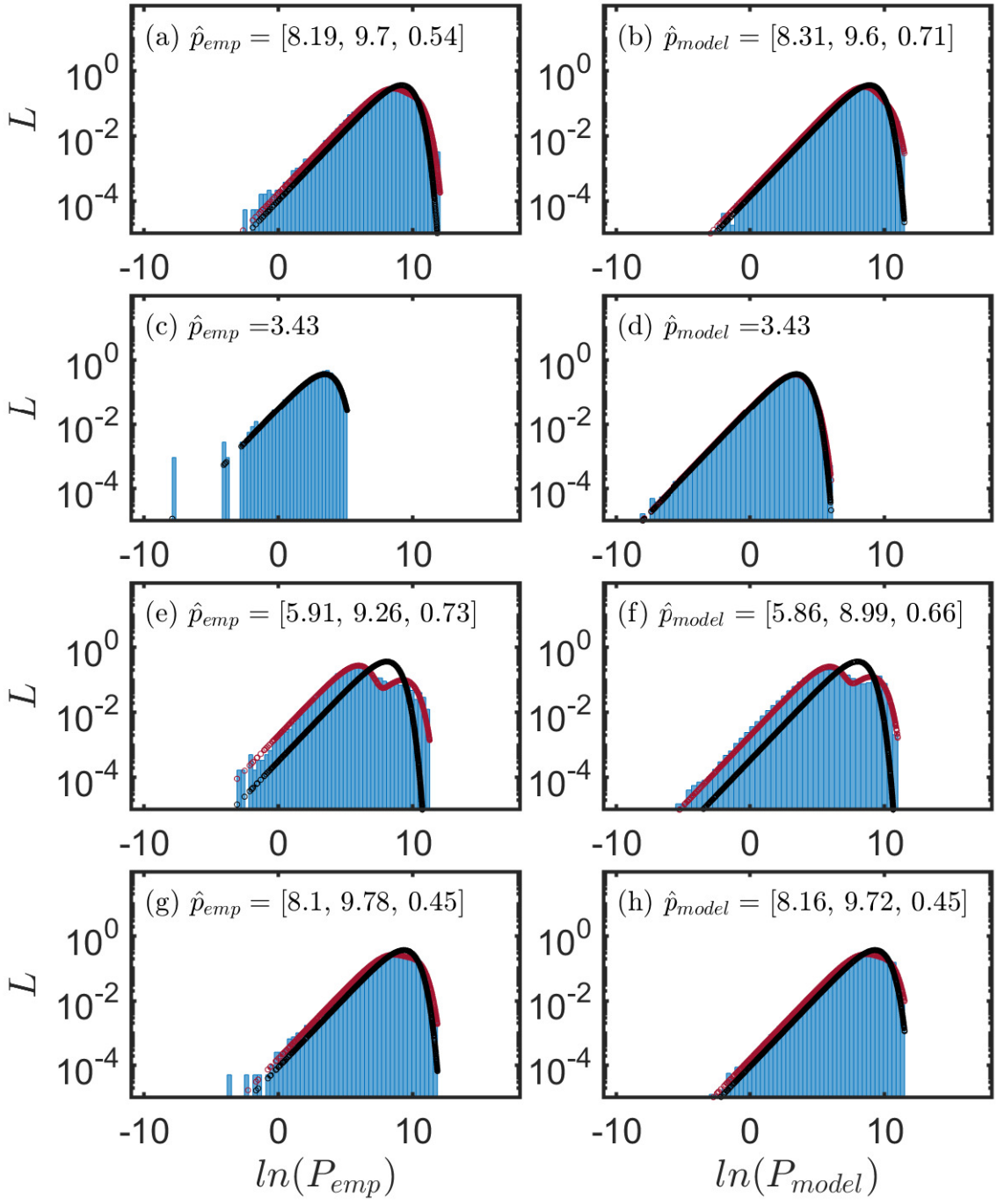

Figure 4.6: L vs. $\ln(P_{emp})$ ($\ln(P_{model})$) for Subject 4. The power P_{model} is calculated using Eq. 4.5. (a) Distribution of P_{emp} in the preictal state, (b) distribution of P_{model} at $\Delta\beta = 0.99$, $\lambda = 4.0$, $D_{add} = 19$, $D_{mult} = 0$, $2\ln s = 11.6$, (c) distribution of P_{emp} in the PGES state, (d) distribution of P_{model} at $\Delta\beta = 15$, $\lambda = 4.0$, $D_{add} = 15$, $D_{mult} = 0$, $2\ln s = 6.8$, (e) distribution of P_{emp} in the transition state, (f) distribution of P_{model} at $\Delta\beta = 0.4$, $\lambda = 8.0$, $D_{add} = 15$, $D_{mult} = 70$, $2\ln s = 7.6$, (g) distribution of P_{emp} in the revival state, (h) distribution of P_{model} at $\Delta\beta = 0.85$, $\lambda = 4.0$, $D_{add} = 15$, $D_{mult} = 0$, $2\ln s = 9.9$. $\Delta\beta = \frac{\beta}{-4}$.

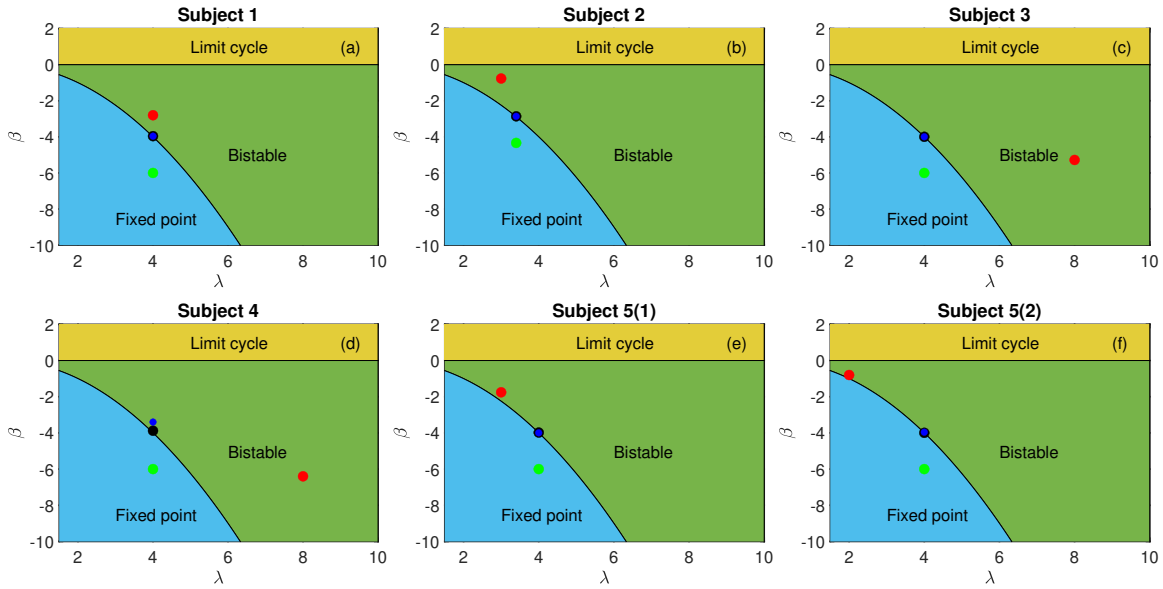

Figure 4.7: β vs λ bifurcation plot for normal form of subcritical Hopf given by Eq. 4.4 with $D_{add} = 0$ and $D_{mult} = 0$. black solid circle corresponds to preictal state, blue solid circle corresponds to revival state, red solid circle corresponds to transition state, green solid circle corresponds to PGES state. Each sub figure corresponds to a seizure, (a) subject 1, (b) subject 2, (c) subject 3, (d) subject 4, (e) subject 5(1), (f) subject 5 (2).

This page was intentionally left blank.

Chapter 5

Summary and Conclusions

The overall theme of this thesis is the study of the phenomenon of oscillation suppression and its application to a neurological condition called Postictal Generalized EEG Suppression (PGES). Typically, oscillators exhibiting limit cycle oscillations can be suppressed by altering a bifurcation parameter. Hopf bifurcation is a classic mathematical framework for describing the cessation of oscillations. Various mathematical oscillator models exhibit Hopf bifurcation in their uncoupled form, with the Stuart-Landau (SL) oscillator being the most prominent example, as it represents the normal form of Hopf bifurcation. In this oscillator, the bifurcation parameter can be adjusted to transition the system from a limit cycle state to a fixed point state.

However, real-world systems are inherently interactive, with oscillators often coupled to others. Hence, in our first work, we investigate various pairwise coupling forms, focusing on repulsive dissimilar coupling, to achieve oscillation suppression via Hopf bifurcation. We develop an analytical framework to determine the stability conditions for equilibrium states in both identical and non-identical systems. This formulation is a generalized extension of existing frameworks, as it is independent of network size and accommodates heterogeneous coupling. Nonetheless, it has limitations when applied to complex network structures.

To explore real-world applications of our model, we turn to neuropathological conditions.

PGES is a state observed in patients following tonic-clonic seizures, characterized by a marked suppression in EEG signals. We construct functional connectivity matrices from the EEG signals of such patients and use these as the network structure in our dynamical model. Our findings reveal significant suppression in the model's dynamics immediately following a seizure, aligning with observed EEG patterns.

In the next chapter, we move beyond pairwise interactions, applying the SL model to triadic interactions. We observe a first-order transition to a single-death state, which is coupling-dependent. This state cannot be classified as an amplitude death (AD) state, as it is not the trivial state of the uncoupled system. Furthermore, a first-order transition to amplitude death is theoretically forbidden. The other possible candidate, oscillation death (OD), corresponds to an inhomogeneous steady state. However, in our case, only one stable equilibrium exists, which we term a "solitary death (SD)" state. Notably, we encounter a saddle homoclinic bifurcation during the transition to SD, an uncommon occurrence in SL oscillators, where first-order transitions to death typically occur via subcritical Hopf bifurcations. We hypothesize that the higher-order interactions are responsible for this phenomenon and other unique findings associated with the SD state.

In the final chapter, we address the limitations encountered in applying our model to PGES. In Chapter 2, we used functional connectivity matrices derived from EEG data as the adjacency matrices of our dynamical model. While prior studies suggest that functional connectivity and structural connectivity are similar over longer time scales, this assumption may not hold for shorter time scales). To address this limitation, we adopt an alternative approach. Here, we use a simpler uncoupled dynamical model and introduce stochasticity to generate time series that mimic EEG signals. We identify parameter values in the dynamical model corresponding to different stages of PGES. Our results show statistical similarity between the model-generated signals and the EEG data. Additionally, we observe a phase transition from a stable to a bistable state as the patient recovers from PGES.

5.1 Scope for Future Research

- In the future, we aim to introduce coupling in our model to discover the appropriate forms of coupling required to generate signals similar to EEG signals from various pathological conditions. These results can then be compared with resting-state dynamics.
- We plan to explore alternative approaches for modeling neurobiological data using dynamical differential equations. Incorporating the dynamics of functional connectivity in EEG data may enable more accurate modeling.
- Higher-order interactions have rarely been studied in real data but hold significant potential. Developing a framework to identify higher-order interactions in EEG data could address fundamental questions in neuroscience and further bridge the gap between neuroscience and nonlinear dynamics.

This page was intentionally left blank.

Appendix A

Simulation results for two more seizures

We have performed numerical simulations using dissimilar repulsive feedback coupled SL oscillators on networks obtained from two more seizure data (Fig. A.1 and Fig. A.2). The results show similar behavior to other seizures which helps us in proving the robustness of our findings.

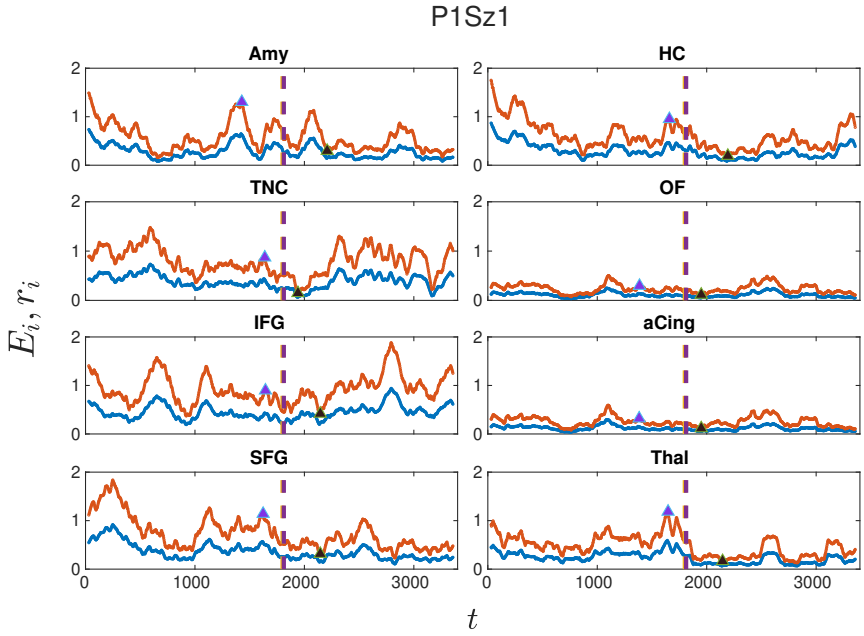

Figure A.1: Δ band for P1Sz1: Red and blue lines correspond to E_i vs time r_i vs time respectively, the yellow dashed line corresponds to the time where the ictal region starts and the violet dashed line represents the end time of ictal region ends.

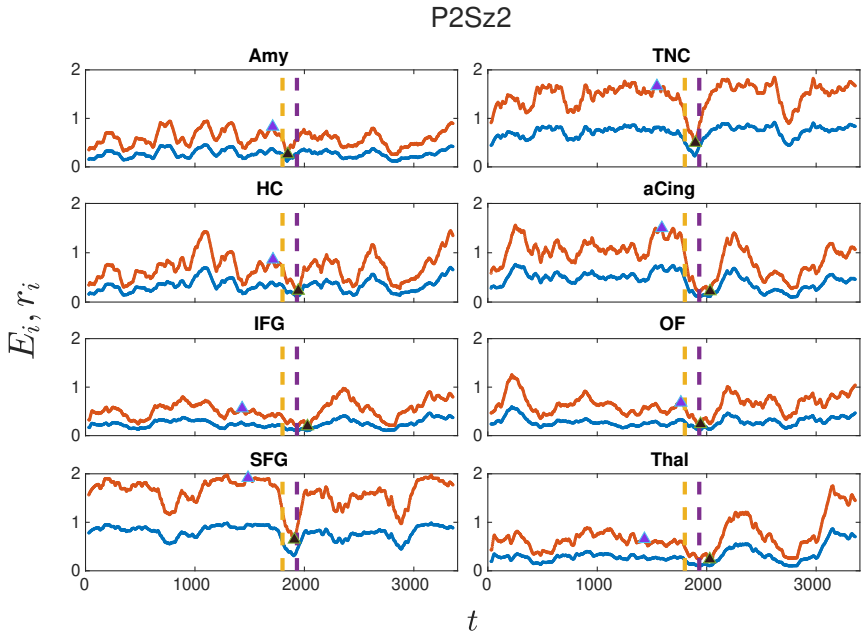

Figure A.2: Δ band for P2Sz2: Red and blue lines correspond to E_i vs time and r_i vs time respectively, the yellow dashed line represents the time where the ictal region starts and the violet dashed line corresponds to the end time of ictal region ends.

Appendix B

Solitary death

Now we are considering an ensemble of N SL oscillators, which are interacting with each other via higher-order interaction similar to Chapter 3 3.1. The dynamics of coupled SL oscillators are given by,

$$\dot{z}_j(t) = (1 - |z_j(t)|^2)z_j + i\omega z_j + \frac{\varepsilon}{N^2}\sum_{k=1}^{N}\sum_{l=1}^{N} z_k z_l \tag{B.1}$$

Trajectory: Initially, in the incoherent state the trajectories are elliptical which is shown in Fig. B.1(a). However, there is no presence of a limit cycle since different initial conditions assume different closed orbits. Upon increasing the coupling strength the system attains a synchronized state, where the shape of the orbit deforms which is shown in Fig. B.1(b). Coupled system stabilized at a coupling-dependent steady state for a higher value of coupling, which is shown in Fig. B.1(c). We also observed toroid orbit for a higher value of the coupling strength which is shown in Fig. B.1(d).

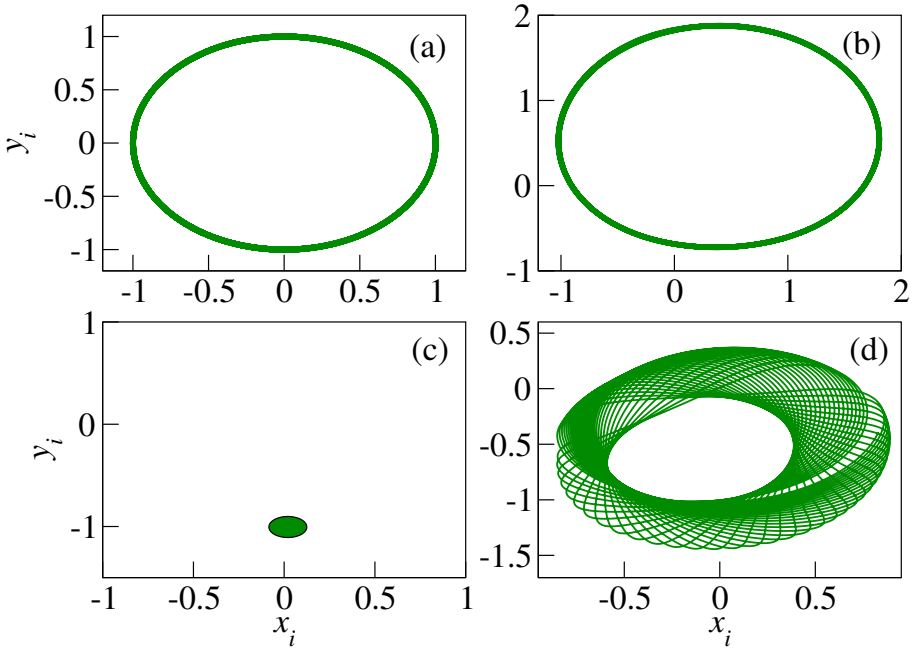

Figure B.1: Trajectory of the coupled SL oscillator governed by Eq. 3.1 in (x, y) phase space for (a) incoherent state ($\varepsilon = 1.0$), (b) synchronized state ($\varepsilon = 3.0$), (c) oscillation death ($\varepsilon = 4.0$) (d) torus ($\varepsilon = 8.0$).

Effects of noise: To check the robustness of the results, we analyze the effects of noise. We include Gaussian noise $\xi_j(t)$ in Eq. 3.1. The dynamics equation of coupled SL oscillators in the presence of noise can be written as

$$\dot{z}_j(t) = (1 - |z_j(t)|^2)z_j + i\omega z_j + \frac{\varepsilon}{N^2}\sum_{k=1}^{N}\sum_{l=1}^{N} z_k z_l + \gamma\xi_j(t)$$

where γ is the strength of Gaussian noise. We set noise strength $\gamma = 0.001$ and calculate amplitude order parameter A in both forward and backward directions (Fig. B.2). In the forward direction, we observe a revival of oscillation in the presence of noise which is not observed in the absence of noise. Due to the presence of noise in the forward transition, the initial conditions in each value of coupling strength can be slightly different for all the synchronized oscillators. Then, at a critical coupling strength, the system oscillates.

Conjugate coupling in higher order: Here, we propose another form of higher-order coupling, where three oscillators interact via a multiplicative conjugate coupling. The dynamics of

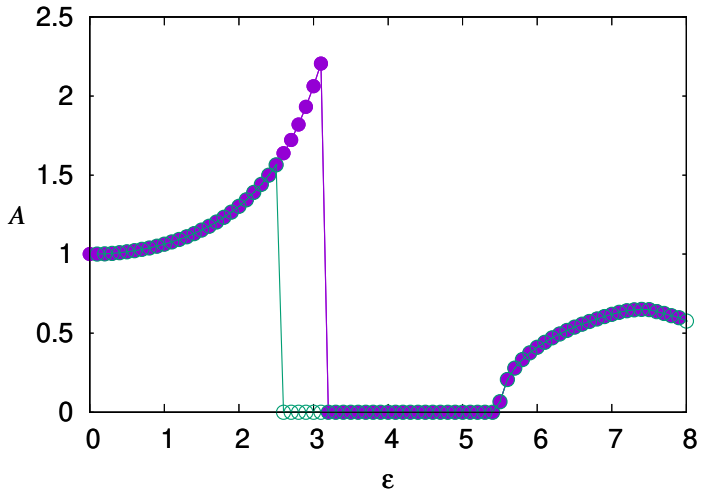

Figure B.2: Amplitude order parameter A plotted with coupling strength ε in both forward and backward direction in the presence of noise. The other parameters are $\omega = 4$, $N = 1000$ and $\gamma = 0.001$.

the coupled system can be written as,

$$\dot{z}_j(t) = (1 - |z_j(t)|^2)z_j + i\omega z_j + \frac{\varepsilon}{N^2}\sum_{k=1}^{N}\sum_{l=1}^{N} z_k z_l^*$$

An introduction of the higher-order conjugate coupling between a pair of connected nodes and upon substituting $z = x + iy$, the resulting equation is,

$$\begin{aligned} \dot{x}_j &= (1 - x_j^2 - y_j^2)x_j - w_j y_j + \frac{\varepsilon}{N^2}\sum_{k,l=1}^{N}(x_k x_l + y_l y_k), \\ \dot{y}_j &= (1 - x_j^2 - y_j^2)y_j + w_j x_j \end{aligned}$$

(B.2)

In this model, the dynamics are a little different than in the previous model. We first calculate the synchronization order parameter S in both forward and backward directions which is shown

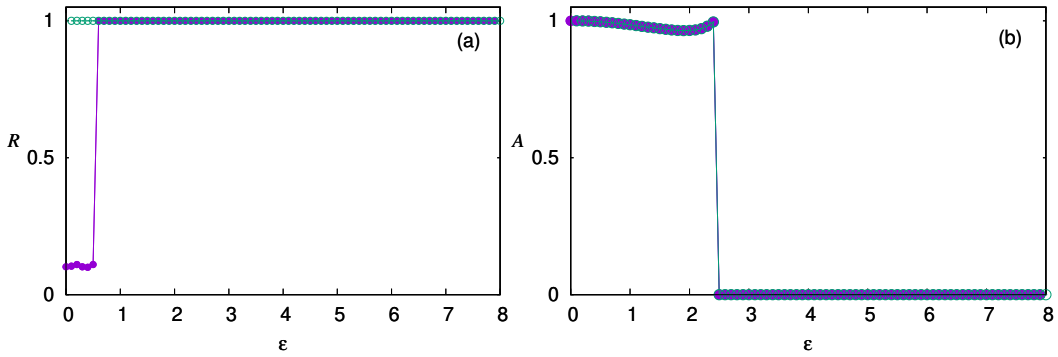

Figure B.3: (a) Synchronization order parameter R and (b) Amplitude order parameter A calculated in both forward and backward direction of coupled SL oscillators governed by Eq. B.2. The other parameters are $N = 1000$ and $\omega = 4.0$.

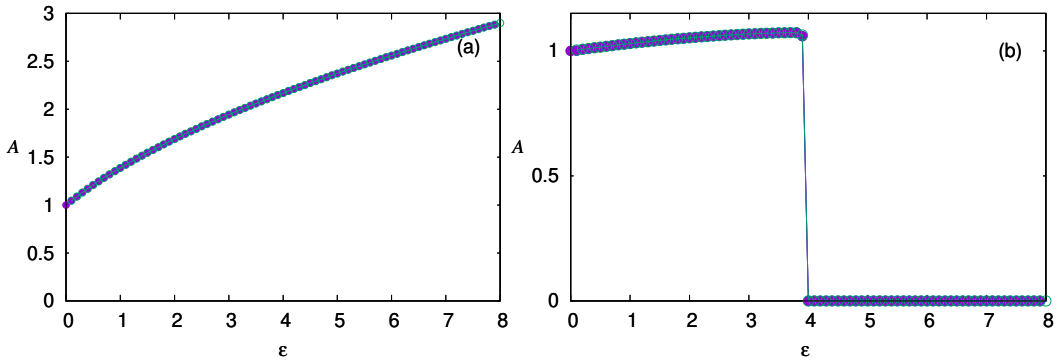

Figure B.4: Amplitude order parameter A calculated in both forward and backward direction of coupled SL oscillators of Eq. B.3 (a) positive feedback coupling in both variable x and y (b) positive feedback in x variable and negative feedback coupling in variable y. The other parameters are $N = 1000$, and $\omega = 4.0$.

in Fig. B.3(a). Here we can see that the order parameter shows a sudden transition in the forward direction, however, there is no transition in the backward direction. The amplitude order parameter A is also calculated in both forward and backward directions (Fig. B.3(b)). Here, we can see that both forward and backward transition points occur at the same value, showing no hysteresis. In this case, we also observe that there is no increase in the amplitude of the oscillator after synchronization.

Stuart-Landau oscillators with pairwise interaction: Next, we consider an ensemble of N SL oscillators, which interact via pairwise interaction. The dynamics of coupled SL oscillators

are given by,

$$\dot{z}_j(t) = (1 - |z_j(t)|^2)z_j + i\omega z_j + \frac{\varepsilon}{N^2}\sum_{k=1}^{N} F_k \tag{B.3}$$

where $F_k = z_k$ or z_k^*. In the case of pairwise interaction, when both variable x and y get positive feedback (i.e. we are considering $F_k = z_k$ in coupling term in the Eq. B.3) we observe that only the amplitude of the coupled system is increasing, which is shown in Fig. B.4(a). On the other hand when the x variable is getting positive feedback and y variable getting negative feedback (i.e. we consider $F_k = z_k^*$ in the coupling term of Eq. B.3) we observe a sudden transition from oscillatory state to death state in both forward and backward continuation (Fig. B.4(b)). Here both forward and backward transition points are the same.

This page was intentionally left blank.

References

Aiba, I., Noebels, J. L., 2015. Spreading depolarization in the brainstem mediates sudden cardiorespiratory arrest in mouse sudep models. Science Translational Medicine 7 (282), 282ra46–282ra46.
URL https://www.science.org/doi/abs/10.1126/scitranslmed.aaa4050

Albert, R., Barabási, A.-L., Jan 2002. Statistical mechanics of complex networks. Rev. Mod. Phys. 74, 47–97.
URL https://link.aps.org/doi/10.1103/RevModPhys.74.47

Aron, L., Yankner, B. A., 2016. Neural synchronization in alzheimer's disease. Nature 540 (7632), 207–208.

Asadollahi, M., Noorbakhsh, M., Simani, L., Ramezani, M., Gharagozli, K., 2018. Two predictors of postictal generalized eeg suppression: Tonic phase duration and postictal immobility period. British Epilepsy Association.

Ashwin, P., Coombes, S., Nicks, R., 2016. Mathematical frameworks for oscillatory network dynamics in neuroscience. The Journal of Mathematical Neuroscience 6, 1–92.

Baccalá, L. A., Sameshima, K., 2001. Partial directed coherence: a new concept in neural structure determination. Biological Cybernetics 2001 84:6 84 (6), 463–474.
URL https://link.springer.com/article/10.1007/PL00007990

Baccala, L. A., Sameshima, K., Takahashi, D. Y., 2007. Generalized partial directed coherence. 2007 15th International Conference on Digital Signal Processing, DSP 2007, 163–166.

Banerjee, T., Ghosh, D., Jun 2014a. Experimental observation of a transition from amplitude to oscillation death in coupled oscillators. Phys. Rev. E 89, 062902.
URL https://link.aps.org/doi/10.1103/PhysRevE.89.062902

Banerjee, T., Ghosh, D., May 2014b. Transition from amplitude to oscillation death under mean-field diffusive coupling. Phys. Rev. E 89, 052912.
URL https://link.aps.org/doi/10.1103/PhysRevE.89.052912

Barabási, A.-L., 2016. Network Science. Cambridge University Press.
URL http://networksciencebook.com/

Bateman, L. M., Mendiratta, A., Liou, J.-Y., Smith, E. J., Bazil, C. W., Choi, H., McKhann, G. M., Pack, A., Srinivasan, S., Schevon, C. A., 2019. Postictal clinical and electroencephalographic activity following intracranially recorded bilateral tonic–clonic seizures. Epilepsia 60 (1), 74–84.

Battiston, F., Abaid, E. T. N., Arenas, A., Kühn, R., Porter, M. A., Gleeson, J. P., Domenico, M. D., 2020. Networks beyond pairwise interactions: Structure and dynamics. Physics Reports 874, 1–92.

Bauer, P. R., Thijs, R. D., Lamberts, R. J., Velis, D. N., Visser, G. H., Tolner, E. A., Sander, J. W., Lopes da Silva, F. H., Kalitzin, S. N., 01 2017. Dynamics of convulsive seizure termination and postictal generalized EEG suppression. Brain 140 (3), 655–668.
URL https://doi.org/10.1093/brain/aww322

Blanco, R., Preti, M. G., Koba, C., Ville, D. V. D., Crimi, A., 2024. Comparing structure–function relationships in brain networks using eeg and fnirs. Scientific Reports 14, Article number: 28976.

Blenkmann, A. O., Phillips, H. N., Princich, J. P., Rowe, J. B., Bekinschtein, T. A., Muravchik, C. H., Kochen, S., mar 2017. Ielectrodes: A comprehensive open-source toolbox for depth and subdural grid electrode localization. Frontiers in Neuroinformatics 11, 14.

Bonilha, L., Nesland, T., Martz, G. U., Joseph, J. E., Spampinato, M. V., Edwards, J. C., Tabesh, A., 2012. Medial temporal lobe epilepsy is associated with neuronal fibre loss and paradoxical increase in structural connectivity of limbic structures. Journal of Neurology, Neurosurgery, and Psychiatry 83 (9), 903–909.

Breakspear, M., 2017. Dynamic models of large-scale brain activity. Nature Neuroscience 20, 342–350.
URL https://doi.org/10.1038/nn.4497

Breakspear, M., Heitmann, S., Daffertshofer, A., 2010. Generative models of cortical oscillations: neurobiological implications of the kuramoto model. Frontiers in Human Neuroscience 4, 190.

Breakspear, M., Roberts, J. A., Terry, J. R., Rodrigues, S., Mahant, N., Robinson, P. A., 2006. A unifying explanation of primary generalized seizures through nonlinear brain modeling and bifurcation analysis. Cerebral Cortex 16 (9), 1296–1313.

Cabral, J., Hugues, E., Kringelbach, M. L., Deco, G., 2012. Modeling the outcome of structural disconnection on resting-state functional connectivity. NeuroImage 62 (3), 1342–1353.

Cabral, J., Kringelbach, M. L., Deco, G., 2017. Functional connectivity dynamically evolves on multiple time-scales over a static structural connectome: Models and mechanisms. NeuroImage 160, 84–96.

Carletti, T., Fanelli, D., Nicoletti, S., 2020. Dynamical systems on hypergraphs. Journal of Physics: Complexity 1 (3), 035006.

Caízares, C. A., 2001. On bifurcations, voltage collapse and load modeling. IEEE Transactions on Power Systems 16 (3), 617–623.

Chaitanya, S. P., apr 2020. Robot-assisted stereoelectroencephalography exploration of the limbic thalamus in human focal epilepsy: implantation technique and complications in the first 24 patients. Neurosurgical focus 48 (4).
URL `https://pubmed.ncbi.nlm.nih.gov/32234983/`

Cohen, M. X., 2014. Analyzing neural time series data: theory and practice. MIT Press.

Davidson, C. M., de Paor, A. M., Lowery, M. M., 2012. Insights from control theory into deep brain stimulation for relief from parkinson's disease. In: 2012 ELEKTRO. pp. 2–7.

Deco, G., Jirsa, V. K., 2012. Ongoing cortical activity at rest: Criticality, multistability, and ghost attractors. Journal of Neuroscience 32 (10), 3366–3375.

Demirtaş, M., Falcon, C., Tucholka, A., Gispert, J. D., Molinuevo, J. L., Deco, G., 2017. A whole-brain computational modeling approach to explain the alterations in resting-state functional connectivity during progression of alzheimer's disease. Neuroimage 16, 343–354.

Devaney, R. L., 1989. An Introduction to Chaotic Dynamical Systems, 2nd Edition. Addison-Wesley.

Dutta, S., Alamoudi, O., Vakilna, Y. S., Pati, S., Jalan, S., 2023a. Oscillation quenching in stuart-landau oscillators via dissimilar repulsive coupling. Physical Review Research 5 (1), 013074.

Dutta, S., Alamoudi, O., Vakilna, Y. S., Pati, S., Jalan, S., 2023b. Oscillation quenching in stuart-landau oscillators via dissimilar repulsive coupling. Physical Review Research 5 (1), 013074.

Ermentrout, B., 2012. XPPAUT. Springer Netherlands, Dordrecht, pp. 519–531.
URL https://doi.org/10.1007/978-94-007-3858-4_17

Feller, W., 1991. An introduction to probability theory and its applications, Volume 1. John Wiley & Sons.

Feng, S., Dickerson, S. R., Goutsias, J. G., 2021. Hypergraph models of biological networks to identify genes critical to pathogenic viral response. BMC Bioinformatics 22 (1), 154.

Fisher, R. S., Engel Jr, J. J., 2010. Definition of the postictal state: when does it start and end? Epilepsy & Behavior 19 (2), 100–104.

FitzHugh, R., 1961. Impulses and physiological states in theoretical models of nerve membrane. Biophysical Journal 1 (6), 445–466.

FRASCA, M., BERGNER, A., KURTHS, J., FORTUNA, L., 2012. Bifurcations in a star-like network of stuart–landau oscillators. International Journal of Bifurcation and Chaos 22 (07), 1250173.
URL https://doi.org/10.1142/S0218127412501738

Freyer, F., Aquino, K., Robinson, P. A., Ritter, P., Breakspear, M., 2009. Bistability and non-gaussian fluctuations in spontaneous cortical activity. Journal of Neuroscience 29 (26), 8512–8524.

Freyer, F., Roberts, J. A., Ritter, P., Breakspear, M., 2012. A canonical model of multistability and scale-invariance in biological systems.

Gallego, B., Cessi, P., 2001. Decadal variability of two oceans and an atmosphere. Journal of Climate 14 (13), 2815–2832.

Gambuzza, L. V., Cardillo, A., Fiasconaro, A., Fortuna, L., Gómez-Gardenes, J., Frasca, M., 2013. Analysis of remote synchronization in complex networks. Chaos: An Interdisciplinary Journal of Nonlinear Science 23 (4).

García-Morales, V., Krischer, K., 2022. The complex ginzburg–landau equation: An introduction. Contemporary Physics.

Gerster, M., Berner, R., Sawicki, J., Zakharova, A., Škoch, A., Hlinka, J., Lehnertz, K., Schöll, E., 2020. Fitzhugh–nagumo oscillators on complex networks mimic epileptic-seizure-related synchronization phenomena. Chaos: An Interdisciplinary Journal of Nonlinear Science 30 (12), 123130.
URL https://doi.org/10.1063/5.0021420

Ghosh, A., Rho, Y., McIntosh, A. R., Kötter, R., Jirsa, V. K., 2008. Cortical network dynamics with time delays reveals functional connectivity in the resting brain. Cognitive Neurodynamics 2 (2), 115–120.

Gleick, J., 1987. Chaos: Making a New Science. Viking, New York.

Goldstein, H., Poole, C. P., Safko, J. L., 2002. Classical Mechanics, 3rd Edition. Addison-Wesley.

Gonen, F. F., Tcheslavski, G. V., 2012. Techniques to assess stationarity and gaussianity of eeg: An overview. International Journal Bioautomation 16 (2), 135.

Grigorovsky, V., Jacobs, D., Breton, V. L., Tufa, U., Lucasius, C., del Campo, J. M., Chinvarun, Y., Carlen, P. L., Wennberg, R., Bardakjian, B. L., 11 2020. Delta-gamma phase-amplitude coupling as a biomarker of postictal generalized EEG suppression. Brain Communications 2 (2), fcaa182.
URL https://doi.org/10.1093/braincomms/fcaa182

Hens, C. R., Olusola, O. I., Pal, P., Dana, S. K., Sep 2013. Oscillation death in diffusively coupled oscillators by local repulsive link. Phys. Rev. E 88, 034902.
URL https://link.aps.org/doi/10.1103/PhysRevE.88.034902

Hindmarsh, J. L., Rose, R. M., 1984. A model of neuronal bursting using three coupled first order differential equations. Proceedings of the Royal Society of London. Series B, Biological Sciences 221 (1222), 87–102.

Hodgkin, A. L., Huxley, A. F., 1952. Propagation of electrical signals along giant nerve fibres. Philosophical Transactions of the Royal Society of London. Series B, Biological Sciences 140, 177–183.

Hollister, L. E., Davis, K. L., Davis, B. M., 1980. Hormones in the treatment of psychiatric disorders. In: Kreiger, D. T., Hughes, J. C. (Eds.), Neuroendocrinology. Sinauer, Sunderland, MA, pp. 167–175.

Horn, A., Kühn, A. A., feb 2015. Lead-DBS: a toolbox for deep brain stimulation electrode localizations and visualizations. NeuroImage 107, 127–135.
URL https://pubmed.ncbi.nlm.nih.gov/25498389/

Hou, Z., Xin, H., Nov 2003. Oscillator death on small-world networks. Phys. Rev. E 68, 055103.
URL https://link.aps.org/doi/10.1103/PhysRevE.68.055103

Hutchison, R. M., Womelsdorf, T., Allen, E. A., Bandettini, P. A., Calhoun, V. D., Corbetta, M., Della Penna, S., Duyn, J. H., Glover, G. H., Gonzalez-Castillo, J., Handwerker, D. A., Keilholz, S., Kiviniemi, V., Leopold, D. A., de Pasquale, F., Sporns, O., Walter, M., Chang, C., 2013. Dynamic functional connectivity: promise, issues, and interpretations. NeuroImage 80, 360–378.

Jalan, S., 2023. Synchronization transitions in adaptive kuramoto–sakaguchi oscillators with higher-order interactions. Chaos: An Interdisciplinary Journal of Nonlinear Science 33 (10), 103101.

Jalan, S., Sarkar, C., 2017. Complex networks: An emerging branch of science. Physics News 47, 3–4.

Jalan, S., Suman, A., 2022. Multiple first-order transitions in simplicial complexes on multilayer systems. Physical Review E 106 (4), 044304.

Jansen, B. H., Rit, V. G., 1995. Electroencephalogram and visual evoked potential generation in a mathematical model of coupled cortical columns. Biological Cybernetics 73, 357–366.

Jirsa, V. K., Stacey, W. C., Quilichini, P. P., Ivanov, A. I., Bernard, C., 2014. On the nature of seizure dynamics. Brain 137 (8), 2210–2230.

Kachhvah, A. D., Jalan, S., 2022. Hebbian plasticity rules abrupt desynchronization in pure simplicial complexes. New Journal of Physics 24 (5), 052002.

Kanth, K. M., Zimmerman, C. S., Toprani, S., Seyal, M., 2022. Duration of postictal impaired awareness after bilateral tonic-clonic seizures: Eeg and patient characteristics. Epilepsy & Behavior 128.

Karnatak, R., Ramaswamy, R., Prasad, A., Sep 2007. Amplitude death in the absence of time delays in identical coupled oscillators. Phys. Rev. E 76, 035201.
URL https://link.aps.org/doi/10.1103/PhysRevE.76.035201

Kim, H., Moon, J.-Y., Mashour, G. A., Lee, U., 08 2018. Mechanisms of hysteresis in human brain networks during transitions of consciousness and unconsciousness: Theoretical principles and empirical evidence. PLOS Computational Biology 14 (8), 1–22.
URL https://doi.org/10.1371/journal.pcbi.1006424

Kim, M.-Y., Roy, R., Aron, J. L., Carr, T. W., Schwartz, I. B., Feb 2005. Scaling behavior of laser population dynamics with time-delayed coupling: Theory and experiment. Phys. Rev. Lett. 94, 088101.
URL https://link.aps.org/doi/10.1103/PhysRevLett.94.088101

Klamt, S., Haus, U. U., Theis, F., 2009. Hypergraphs and cellular networks. PLoS Computational Biology 5 (5), e1000385.

Konishi, K., 2003. Amplitude death induced by dynamic coupling. Physical Review E 68 (6), 067202.

Koseska, A., Ullner, E., Volkov, E., Kurths, J., García-Ojalvo, J., 2010. Cooperative differentiation through clustering in multicellular populations. Journal of Theoretical Biology 263 (2), 189–202.

Koseska, A., Volkov, E., Kurths, J., 2013a. Oscillation quenching mechanisms: Amplitude vs. oscillation death. Physics Reports 531 (4), 173–199, oscillation quenching mechanisms: Amplitude vs. oscillation death.
URL https://www.sciencedirect.com/science/article/pii/S0370157313002652

Koseska, A., Volkov, E., Kurths, J., Jul 2013b. Transition from amplitude to oscillation death via turing bifurcation. Phys. Rev. Lett. 111, 024103.
URL https://link.aps.org/doi/10.1103/PhysRevLett.111.024103

Kumar, P., Prasad, A., Ghosh, R., 2008. Stable phase-locking of an external-cavity diode laser subjected to external optical injection. Journal of Physics B: Atomic, Molecular and Optical Physics 41 (13), 135402.

Kuramoto, Y., 1984. Chemical Oscillations, Waves, and Turbulence. Vol. 19 of Texts in Applied Mathematics. Springer.

Kuznetsov, Y. A., 2013. Elements of Applied Bifurcation Theory, 2nd Edition. Springer.

Lhatoo, S. D., Faulkner, H. J., Dembny, K., Trippick, K., Johnson, C., Bird, J. M., 2010a. An electroclinical case-control study of sudden unexpected death in epilepsy. Annals of Neurology 68 (6), 787–796.

Lhatoo, S. D., Faulkner, H. J., Dembny, K., Trippick, K., Johnson, C., Bird, J. M., 2010b. An electroclinical case-control study of sudden unexpected death in epilepsy. Annals of Neurology 68 (6), 787–796.

Lion, K., Winter, D., 1953. A method for the discrimination between signal and random noise of electrobiological potentials. Electroencephalography and Clinical Neurophysiology 5 (1), 109–111.

Liu, W., Wang, X., Guan, S., Lai, C.-H., sep 2009. Transition to amplitude death in scale-free networks. New Journal of Physics 11 (9), 093016.
URL https://doi.org/10.1088/1367-2630/11/9/093016

Liu, Z., Han, F., Wang, Q., 2023. Task-relevant brain dynamics among cognitive subsystems induced by regional stimulation in a whole-brain computational model. Physical Review E 108 (4), 044402.

López-González, A., Panda, R., Ponce-Alvarez, A., Zamora-López, G., Escrichs, A., Martial, C., 2021. Loss of consciousness reduces the stability of brain hubs and the heterogeneity of brain dynamics. Communications Biology 4, 1–15.

Marchi, A., Giusiano, B., King, M., Lagarde, S., Trébuchon-Dafonseca, A., Bernard, C., Rheims, S., Bartolomei, F., McGonigal, A., 2019. Postictal electroencephalographic (eeg) suppression: A stereo-eeg study of 100 focal to bilateral tonic–clonic seizures. Epilepsia 60 (1), 63–73.

Marsden, J. E., McCracken, M., 1976. The Hopf Bifurcation and Its Applications. Vol. 19 of Applied Mathematical Sciences. Springer.

Maslennikov, O. V., Nekorkin, V. I., 2018. Hierarchical transitions in multiplex adaptive networks of oscillatory units. Chaos: An Interdisciplinary Journal of Nonlinear Science 28 (12), 121101.
URL https://doi.org/10.1063/1.5077075

McEwen, J. A., Anderson, G. B., 1975. Modeling the stationarity and gaussianity of spontaneous electroencephalographic activity. IEEE transactions on Biomedical Engineering (5), 361–369.

Mier, J. C., Kim, Y., Jiang, X., Zhang, G.-Q., Lhatoo, S., 2020. Categorisation of eeg suppression using enhanced feature extraction for sudep risk assessment. BMC Medical Informatics and Decision Making 20, 1–6.

Milton, J. G., Longtin, A., Beuter, A., Mackey, M. C., Glass, L., 1989. Complex dynamics and bifurcations in neurology. Journal of Theoretical Biology 138 (2), 129–147.

Mirollo, R., Strogatz, S. H., 1990. Amplitude death in an array of limit-cycle oscillators. Journal of Statistical Physics 60, 245–262.

Moosavi, S. A., Jirsa, V. K., Truccolo, W., 2022. Critical dynamics in the spread of focal epileptic seizures: Network connectivity, neural excitability, and phase transitions. PLOS One 17 (8), e0272902.

Nandan, M., Hens, C. R., Pal, P., Dana, S. K., 2014. Transition from amplitude to oscillation death in a network of oscillators. Chaos: An Interdisciplinary Journal of Nonlinear Science 24 (4), 043103.
URL https://doi.org/10.1063/1.4897446

Nazarimehr, F., Hashemi Golpayegani, S. M. R., Hatef, B., 2018. Does the onset of epileptic seizure start from a bifurcation point? The European Physical Journal Special Topics 227, 697–705.

Newman, M., 2010. Networks: An Introduction. Oxford University Press.

O'Sullivan-Greene, E., Mareels, I., Freestone, D., Kulhmann, L., Burkitt, A., 2009. A paradigm for epileptic seizure prediction using a coupled oscillator model of the brain. In: 2009 Annual International Conference of the IEEE Engineering in Medicine and Biology Society. pp. 6428–6431.

Pathak, A., Roy, D., Banerjee, A., 2022. Whole-brain network models: From physics to bedside. Frontiers in Computational Neuroscience 16, 866517.

Prasad, A., Dhamala, M., Adhikari, B. M., Ramaswamy, R., 2010. Amplitude death in nonlinear oscillators with nonlinear coupling. Physical Review E 81 (2), 027201.

Rajakulendran, S., Nashef, L., 2015. Postictal generalized eeg suppression and sudep: A review. Journal of Clinical Neurophysiology 32 (1), 14–20.

Rajmohan, V., Mohandas, E., 2007. The limbic system. Indian Journal of Psychiatry 49 (2), 132–139.

Rajwani, P., Suman, A., Jalan, S., 2023. Tiered synchronization in kuramoto oscillators with adaptive higher-order interactions. Chaos: An Interdisciplinary Journal of Nonlinear Science 33 (12), 123101.

Reddy, D. R., Sen, A., Johnston, G. L., 1998. Time delay induced death in coupled limit cycle oscillators. Physical Review Letters 80 (23), 5109–5112.

Ren, X., Brodovskaya, A., Hudson, J. L., Kapur, J., 2021. Connectivity and neuronal synchrony during seizures. Journal of Neuroscience 41 (36), 7623–7635.

Robinson, C., 1995. Dynamical Systems: Stability, Symbolic Dynamics, and Chaos, 2nd Edition. CRC Press.

Rubchinsky, L., Sushchik, M., Nov 2000. Disorder can eliminate oscillator death. Phys. Rev. E 62, 6440–6446.
URL https://link.aps.org/doi/10.1103/PhysRevE.62.6440

Ryvlin, P., Nashef, L., Lhatoo, S. D., Bateman, L. M., Bird, J., Bleasel, A., Boon, P., Crespel, A., Dworetzky, B. A., Høgenhaven, H., et al., 2013. Incidence and mechanisms of cardiorespiratory arrests in epilepsy monitoring units (mortemus): a retrospective study. The Lancet Neurology 12 (10), 966–977.

Santos, F. A. N., Tewarie, P. K. B., Baudot, P., Luchicchi, A., de Souza, D. B., Girier, G., Milan, A. P., Broeders, T., Centeno, E. G. Z., Cofre, R., Rosas, F. E., Carone, D., Kennedy, J., Stam, C. J., Hillebrand, A., Desroches, M., Rodrigues, S., Schoonheim, M., Douw, L., Quax, R., 2023. Emergence of high-order functional hubs in the human brain. Preprint or journal (to be replaced with correct source if published)Details on volume, issue, pages, or DOI to be added when available.

Sathiyadevi, K., Premraj, D., Banerjee, T., Lakshmanan, M., 2022. Additional complex conjugate feedback-induced explosive death and multistabilities. Physical Review E 106 (2), 024215.

Saunders, M. G., 1963. Amplitude probability density studies on alpha and alpha-like patterns. Electroencephalography and clinical Neurophysiology 15 (5), 761–767.

Saxena, G., Prasad, A., Ramaswamy, R., 2012. Amplitude death: The emergence of stationarity in coupled nonlinear systems. Physics Reports 521 (5), 205–228, amplitude Death: The Emergence of Stationarity in Coupled Nonlinear Systems.
URL https://www.sciencedirect.com/science/article/pii/S0370157312002645

Seyal, M., Hardin, K., Bateman, L., 2012. Postictal generalized eeg suppression is linked to seizure-associated respiratory dysfunction but not postictal apnea 53(5), 825–831.

Sharma, A., Rajwani, P., Jalan, S., 2024. Synchronization transitions in adaptive kuramoto–sakaguchi oscillators with higher-order interactions. Chaos: An Interdisciplinary Journal of Nonlinear Science 34 (1), 013102.

Shine, J. M., Koyejo, O., Bell, P. T., Gorgolewski, K. J., Gilat, M., Poldrack, R. A., 2015. Estimation of dynamic functional connectivity using multiplication of temporal derivatives. NeuroImage 122, 399–407.

Sizemore, A. E., Giusti, C., Kahn, A., Vettel, J. M., Betzel, R. F., Bassett, D. S., 2018. Cliques and cavities in the human connectome. Journal of Computational Neuroscience 44, 115–145.

Skardal, P. S., Arenas, A., 2019. Abrupt desynchronization and extensive multistability in globally coupled oscillator simplexes. Physical Review Letters 122 (24), 248301.

Steinfeld, J. I., Francisco, J. S., Hase, W. L., 1999. Chemical Kinetics and Dynamics, 2nd Edition. Prentice Hall.

Strogatz, S. H., 1994. From kuramoto to crawford: Exploring the onset of synchronization in populations of coupled oscillators. Physics of D 74 (2), 164–177.

Strogatz, S. H., 2015. Nonlinear Dynamics and Chaos: With Applications to Physics, Biology, Chemistry, and Engineering, 2nd Edition. CRC Press.
URL https://doi.org/10.1201/9780429492563

Suman, A., Jalan, S., 2024. Finite-size effect in kuramoto oscillators with higher-order interactions. Chaos: An Interdisciplinary Journal of Nonlinear Science 34 (1), 013101.

Surges, R., Strzelczyk, A., Scott, C. A., Walker, M. C., Sander, J. W., 2011. Postictal generalized electroencephalographic suppression is associated with generalized seizures. Epilepsy & Behavior 21 (3), 271–274.

Tabor, M., 1989. Chaos and Integrability in Nonlinear Dynamics: An Introduction. Wiley-Interscience. John Wiley & Sons.

Tanaka, T., Aoyagi, T., 2011. Multistable attractors in a network of phase oscillators with three-body interactions. Physical Review Letters 106 (22), 224101.

Tao, J. X., Yung, I., Lee, A., Rose, S., Jacobsen, J., Ebersole, J. S., 2013. Tonic phase of a generalized convulsive seizure is an independent predictor of postictal generalized eeg suppression. Epilepsia 54 (11), e131–e134.

Truccolo, W., Ahmed, O. J., Harrison, M. T., Eskandar, E. N., Cosgrove, G. R., Madsen, J. R., Blum, A. S., Potter, N. S., Hochberg, L. R., Cash, S. S., 2014. Neuronal ensemble synchrony during human focal seizures. Journal of Neuroscience 34 (30), 9927–9944.

Tumash, L., Panteley, E., Zakharova, A., 2019. Synchronization patterns in stuart–landau networks: a reduced system approach. The European Physical Journal B 92, 100.

Uhlhaas, P. J., Singer, W., 2006. Neural synchrony in brain disorders: Relevance for cognitive dysfunctions and pathophysiology. Neuron 52 (1), 155–168.

Vasilyeva, E., Kozlov, A., Alfaro-Bittner, K., Musatov, D., Raigorodskii, A. M., Perc, M., Boccaletti, S., 2021. Multilayer representation of collaboration networks with higher-order interactions. Scientific Reports 11 (1), 5666.

Verma, U. K., Ambika, G., 2021. Tipping induced by multiplexing on two-layer networks. The European Physical Journal Special Topics.

Verma, U. K., Sharma, A., Kamal, N. K., Shrimali, M. D., 2018a. First order transition to oscillation death through an environment. Physics Letters A 382 (32), 2122–2126.
URL https://www.sciencedirect.com/science/article/pii/S0375960118305851

Verma, U. K., Sharma, A., Kamal, N. K., Shrimali, M. D., 2018b. First order transition to oscillation death through an environment. Physics Letters A 382 (32), 2122–2126.

Verma, U. K., Sharma, A., Kamal, N. K., Shrimali, M. D., 2019. Explosive death in complex network. Chaos: An Interdisciplinary Journal of Nonlinear Science 29 (6), 063127.
URL https://doi.org/10.1063/1.5054306

Wang, J., Zou, W., 2021. Collective behaviors of mean-field coupled stuart–landau limit-cycle oscillators under additional repulsive links. Chaos: An Interdisciplinary Journal of Nonlinear Science 31 (7), 073107.
URL https://doi.org/10.1063/5.0050698

Xu, J., Jin, B., Yan, J., Wang, J., Hu, J., Wang, Z., Chen, Z., Ding, M., Chen, S., Wang, S., 2016. Postictal generalized eeg suppression after generalized convulsive seizures: A double-edged sword. Clinical Neurophysiology 127 (4), 2078–2084.

Zhao, X.-Q., 2017. Dynamical Systems in Population Biology, 2nd Edition. CMS Books in Mathematics. Springer.

Zhu, J., Zhu, J., Ghosh, S., Wu, W., Yuan, J., 2018. Social influence maximization in hypergraph in social networks. IEEE Transactions on Network Science and Engineering 6 (4), 801–810.

Zlatić, V., Ghoshal, G., Caldarelli, G., 2009. Hypergraph topological quantities for tagged social networks. Physical Review E 80 (3), 036118.